Title

A Numerical Modeling Approach to Investigate Opportunity for Nature-based Shorelines in Urban Estuaries

Author

Taylor-Burns, Rae Monica

Publication Date

2023

Peer reviewed|Thesis/dissertation

UNIVERSITY OF CALIFORNIA
SANTA CRUZ

A NUMERICAL MODELING APPROACH TO INVESTIGATE OPPORTUNITY FOR NATURE-BASED SHORELINES IN URBAN ESTUARIES

A dissertation submitted in partial satisfaction
of the requirements for the degree of

DOCTOR OF PHILOSOPHY

in

OCEAN SCIENCES
with an emphasis in COASTAL SCIENCE AND POLICY

by

Rae Taylor-Burns

December 2023

The Dissertation of Rae Taylor-Burns is approved:

_____
Professor Chris A. Edwards, chair

_____
Patrick L. Barnard, Ph.D.

_____
Professor Michael W. Beck

_____
Professor Andrew M. Moore

_____
Peter F. Biehl
Vice Provost and Dean of Graduate Students

Table of Contents

Table of Contents iii
List of figures vi
List of tables xiii
Abstract xv
Acknowledgements xvi
Introduction 1
References 7
1. The influence of vegetation on wave transformation in sheltered estuaries 11
Abstract 12
1.1 Introduction 12
1.2 Methods 16
1.2.1 Study site 16
1.2.2 Model and data sources 18
1.2.3 Calibration and validation 21
1.2.4 Schematized model setup 25
1.3 Results 33
1.3.1 Wave transformation due to vegetation 33
1.3.2 Effects of marsh and hydrodynamic settings 35
1.3.3 Key drivers of wave transformation 39
1.3.4 Extreme Events 45
1.4. Discussion 47
References 51
2. The value of marsh restoration for flood risk reduction in an urban estuary 60
Abstract 61
2.1 Introduction 61
2.2 Methods 65
2.2.1 Model description 65
2.2.2 Calibration and validation 68
2.2.3 Hydrodynamic simulations 69
2.2.4 Flood damages and socioeconomic analysis 72
2.2.5 Discussion of uncertainties in the flood risk model. 74

2.3 Results 75
2.4 Discussion 78
References 82
3. Exploring limitations of marsh restoration for flood reduction 89
Abstract 90
3.1 Introduction 90
3.2 Methods 92
3.2.1 Study site 92
3.2.2 Management interventions 92
3.2.3 Numerical modeling 93
3.2.4 Simplified inlet-pond model 97
3.2.5 Hypothetical case to assess the effects of sea level rise on wetland restoration management 99
3.3 Results 99
3.3.1 Numerical results 99
3.3.2 Simplified model results 102
3.4. Conclusions 103
References 104
4. Horizonal levees extend the lifespan of a regional levee system 109
Abstract 110
4.1 Introduction 110
4.2 Methods 113
4.2.1 Study site 113
4.2.2 Numerical modeling 114
4.2.3 Transect development 116
4.2.4 Wave and sea level data 119
4.2.5 Horizontal levee design alternatives 122
4.3 Results 124
4.3.1 Effects of sea level rise on overtopping risk 124
4.3.2 Adaptation to sea level rise through horizontal levees 127
4.4 Discussion and conclusions 131
References 135
Conclusions 141

Supplementary material 148
Appendix 159
XBeach Non-hydrostatic 160
Delft 3D Flexible Mesh 163
SWAN 165

List of figures

Figure 1.1 Location (A and B; base-map layer from Google Earth) and view (C; photograph taken by R. Taylor-Burns) of the study site, and depiction of the transect deployed in 2016 by Lacy et al. (2017; D and E). MDF is the offshore site, SPD marks the beginning of the low marsh, DX1 marks the beginning of the first transition zone, DX2 marks the beginning of the second transition zone, and DXA – DX4 are all on the high marsh. 18

Figure 1.2 Results from model calibration (red) and validation (blue), showing wave height (row 1) and wave period (row 2). Columns A through E show model-data agreement at the six offshore observation locations at China Camp State Park, MFD, SPD, DX1, DX2, DXA, and DX3. Locations of these points can be seen in Figure 1.1. Skill scores correspond to relative bias, scatter, and mean absolute error. No calibration data are shown in column D because data were not collected at DX2 during the calibration period. 24

Figure 1.3 Depiction of the schematized transect. Bolded text identifies variables that were changed in the schematized model runs. 32

Figure 1.4 The effects of vegetation on spectral density of wave energy and on wave height. Green lines show model results from a transect with a vegetated marsh and brown lines show results from a transect with an unvegetated marsh. Row 1 row shows, from left to right, spectral density at the offshore boundary (1A), 1 km onto the mudflat (1B), at the edge of the marsh (+1.2 m NAVD88, 1C), 50 m into the marsh (1D), 200 m into the marsh (1E), and of the runup signal (1F), with the y-axis plotted in log scale. Black lines in row 1 indicate idealized JONSWAP spectra determined by wave statistics used at the offshore boundary, which diverge from model results at low frequencies due to wave-wave interactions. The middle three rows show, from top to bottom, total significant wave height (row 2), incoming wave height (row 3), and outgoing, or reflected, wave height (row 4). The bottom row (row 5) shows transect bathymetry in black, vegetation location in green, and mean water level in blue. Bathymetry and water level are identical for the vegetated and unvegetated model. Black labeled dots on the bottom four plots show locations of the spectra in the top row (runup location is variable and thus approximate). Models were forced with wave heights of 1.5 m and steepness of 0.04 (peak period of 4.9 s), and water level was 2.5 m NAVD88 (or 0.65 m of marsh inundation). Drag coefficient (C_d) was 10% of China Camp observations. ... 34

Figure 1.5 Box plots showing changes in wave transformation across the marsh. Wave transformation metrics are on the y axis of all box plots, including: wave height 100 m into the high marsh (Hs, row 1), wave induced setup 100 m into the high marsh (row 2), and R2% (row 3). Characteristics of hydrodynamic conditions are on the x axis of all box plots, including water level (column A), offshore wave steepness (column B), offshore wave height (column C), with each box representing results from all simulations in which the specified

hydrodynamic condition has the same setting. Red lines indicate medians, blue rectangles indicate the interquartile range, and blue dots indicate outliers. There are many positive outliers that are caused by coincidence of high water levels and low drag coefficient (C_d). Water level and wave height are the strongest controls on wave transformation. 36

Figure 1.6 Box plots showing changes in wave transformation across the marsh. Wave transformation metrics are on the y axis of all box plots, including: wave height 100 m into the high marsh (Hs, row 1), wave induced setup 100 m into the high marsh (row 2), R2% (row 3). Characteristics of vegetation are on the x axis of all box plots, including vegetation density (column A), vegetation frictional drag coefficient (C_d, column B), and minimum vegetation elevation (column C), with each box representing results from all simulations in which the specified vegetation condition has the same setting. Red lines indicate medians, blue rectangles indicate the interquartile range, and blue dots indicate outliers. There are many positive outliers that are caused by coincidence of high water levels and low C_d. Vegetation density and C_d are the strongest controls on wave transformation. 37

Figure 1.7 Box plots showing changes in wave transformation across the marsh. Wave transformation metrics are on the y axis of all box plots, including: wave height 100 m into the high marsh (Hs, row 1), wave induced setup 100 m into the high marsh (row 2), and R2% (row 3). Characteristics of marsh morphology are on the x axis of all box plots, including marsh platform elevation (column A), low mash slope (column B), mudflat slope (column C), and marsh platform width (column D), with each box representing results from all simulations in which the specified morphology condition has the same setting. In the shortest marsh setting, Hs and setup were measured at the last vegetated grid cell. Red lines indicate medians, blue rectangles indicate the interquartile range, and blue dots indicate outliers. There are many positive outliers that are caused by coincidence of high water levels and low drag coefficient (C_d). Marsh width is the strongest control on wave transformation. 38

Figure 1.8 The cumulative sum of the difference in medians of Hs, setup, and swash across the range of model settings used in 1.3.2. Variables which produced a cumulative sum greater than 5 cm, shown by the dashed line, were selected to be used in a subsequent analysis. 40

Figure 1.9 An overview of results from the second round of simulations (n = 55) in which wave height, wave steepness, water level, drag coefficient (C_d), and marsh width were all covaried across the ranges identified in Table 1-3, and in which simulations were completed with and without vegetation. In column A, an empirical cumulative density function of significant wave height 100 m into the high marsh (Hs, row 1), setup 100 m into the high marsh (row 2), and runup at the last wet grid cell (row 3) with vegetation present (green) and vegetation removed (brown) from the transect. In column B and C, reduction in wave height 100 m into the high marsh (Hs, row 1), setup 100 m into the high marsh (row 2), and runup at the last wet grid cell (row 3) between vegetated and unvegetated transects, with absolute reduction in B, and percent reduction in C. Dotted lines show the 25^{th}, 50^{th}, and 75^{th}

percentiles. Across the range of settings explored here, vegetation reduces significant wave height 100 m into the marsh by a median of 35 cm (1B); vegetation reduces setup by a median of less than 1 cm (2B); and vegetation reduces runup by a median of 40 cm (3B). ... 41

Figure 1.10 In row 1, empirical cumulative density functions showing significant wave height 100 m into the high marsh; and in row 2, empirical density functions showing wave height reduction due to vegetation. Plots are separated from left to right by wave steepness (column A), wave height [m] (column B), water level [m NAVD88] (column C), drag coefficient (C_d) of vegetation (column D), and marsh width [m] (column E), with each single line on each subplot showing an empirical cumulative density function of the mean Hs values from 5^4 simulations. Results show that the presence of vegetation plays a key role in reducing wave height across the range of simulation settings. 43

Figure 1.11 In row 1, empirical cumulative density functions showing setup 100 m into the high marsh; and in row 2, empirical density functions showing setup reduction due to vegetation. Plots are separated from left to right by wave steepness (column A), wave height [m] (column B), water level [m NAVD88] (column C), drag coefficient (C_d) of vegetation (column D), and marsh width [m] (column E), with each single line on each subplot showing an empirical cumulative density function of the mean setup values from 5^4 simulations. Results show that the presence of vegetation plays a key role in influencing setup, particularly in low water level and in large wave settings. 44

Figure 1.12 In row 1, empirical cumulative density functions showing runup at the last wet grid cell; and in row 2, empirical density functions showing runup reduction due to vegetation. Plots are separated from left to right by wave steepness (column A), wave height [m] (column B), water level [m NAVD88] (column C), drag coefficient (C_d) of vegetation (column D), and marsh width [m] (column E) with each single line on each subplot showing an empirical cumulative density function of the mean runup values from 5^4 simulations. Results show that the presence of vegetation plays a key role in 45

Figure 1.13 Runup across a vegetated marsh (blue) and runup reduction due to vegetation (red) on the y axis, and marsh width on the x axis. Black dots show simulated marsh widths. Conditions represent an extreme storm in San Francisco Bay (wave height of 1.5 m and water level 1.15 m above MHHW). 46

Figure 1.14 Bar graphs showing components of the dynamic water level (left) and the total water level (right), with and without vegetation. Components of the dynamic water level include setup (measured 100 m into the marsh or at the last vegetated grid cell) and swash (measured at the last wet grid cell), and components of the total water level include the still water level (SWL), setup, and swash. The total water level y axis starts at the MHHW level. Bars represent median values and error bars show the middle 50% of values for setup and swash. Vegetation reduces the dynamic water level by a median of 55 cm in conditions

representative of a present-day extreme storm (wave heights of 1.5 m and water level 1.15 m above MHHW), across a range of drag coefficient (C_d), marsh width, and wave steepness values. 47

Figure 2.1 Location of the study area and details of the simulated restorations. (A) and (B) Location of this study, shown by the red dot in (A) and the orange line in (B). The thin white boxes in (B) show the extent of the maps in (C), (E) and (F) and the thick white box in (B) shows the extent of the map in (D). (C) Vertical offset applied to the restoration sites to simulate sediment accretion/nourishment, bringing each site to +1 m relative to mean sea level. These values range from 0.05 to 1.1 m. (D) Levee breaches across historical marsh channels to facilitate tidal connectivity in salt ponds are shown in blue. (E) Current and (F) restored marsh habitat types, determined by elevation relative to tidal datum. The three shades of green, from dark to light, denote low, transition, and high marsh habitat. 64

Figure 2.2 Spatial distribution of (A) economic and (B) social flood reduction benefits of marsh restoration with sea level rise. Green colors signify positive present value and people protected while orange colors signify negative present value and increased risk. 76

Figure 2.3 Effects of marsh restoration and climate change in Colma Creek. (A) shows the study region. (B-D) show reduction in flood heights during a 100-year storm due to habitat restoration with 0, 0.5, and 1.0 m SLR. The green areas represent locations of marsh restoration, the pale blue areas show flood extent, and the bright blue areas represent regions where flood depth is decreased due to the marsh restoration. 78

Figure 3.1 Depiction of the study site (A) and of the management options simulated (B). 93

Figure 3.2 The numerical model mesh is shown in red. The yellow and purple circles show locations of model calibration and validation with sea level observations. The pink and green circles show locations of creek gauge data. The blue rectangles show locations of levee breaches in the Cargill Ponds. The text boxes in the mesh denote the grid resolution of the mesh in its lowest and highest resolution, which are the middle of the bay and in existing and potential San Mateo County marshes, respectively. 94

Figure 3.3 Idealized inlet-pond system representation (upper sketch) and head losses in an idealized inlet channel or breaching (lower sketch). Adapted from Bruun (1978). 97

Figure 3.4 Differences between water levels between three different management interventions and the existing salt ponds (top panels), and with three different levee breach widths (right panel); and differences in timing of peak water levels with existing salt pond (bottom panels). The blue lines and dots show results from 0.5 m SLR and an annual storm. The green lines and dots show results from 0.5 m SLR and a 20-year storm. The orange lines

and dots show results from 0.5 m SLR and a 100-year storm. The right panel corresponds to the black square shown in the marsh restoration water level subplot. The top row shows that marsh restoration (right column) increases water levels most, shown by the highest peaks in the right-most subplot in the top row. The bottom row shows that marsh restoration (right column) causes peak water levels to happen earliest, shown by the colored dots being furthest below the diagonal black line. The right panel shows that larger levee breaches cause water levels in the ponds to be higher, shown by the large dashed lines reaching higher values than the medium dashed lines or the dotted lines. 100

Figure 3.5 Flood extents and depths in the Cargill Ponds during the 0.5 m SLR and 100-year storm simulation, with the existing ponds on the top and the marsh restoration scenario on the bottom. Each column shows the modeled flood plain at a 50-minute time step, which is shown in the column title. In the marsh restoration scenario (bottom row), the ponds fill more quickly and the levee behind the ponds overtops earlier compared to the existing marsh scenario, resulting in increased flood risk. This can be seen by differences between the existing and restored flood plains at 20:00:00 and 20:50:00. At both of these model time steps, the restoration scenario results in increased flooding behind the red line which represents the levee separating the ponds from residential and industrial development. .. 101

Figure 3.6 Water level and associated flooded surface area within the tidal pond in column 1. Modeled water levels inside and outside the tidal pond are shown in columns 2 through 4, with varying sea levels in each column and varying levee breach widths in each color..... 102

Figure 3.7 Water level inside the pond under three sea level rise scenarios (panels) with three breach widths (colors) and two area laws (line types). 103

Figure 4.1 Depiction of a horizontal levee (A) and study location (B and C)..... 114

Figure 4.2 The relative wave height to surge ratio along throughout the study region (A) and areas with a relative wave height to surge ratio shown in orange, areas identified by Beagle et al. (2019) as suitable for horizontal levees shown in teal, and transects used in this study shown in white (B)..... 117

Figure 4.3 Gray dots show hindcast wave height (O'Neill et al., 2017) and water levels (Nederhoff et al., 2021) at or near the end of transect 37. These values were used as input for the joint probability analysis, which produced the return period curves which are shown in black. Text labels signify what the return period is for each of the six black lines. The gray lines underneath the thick black lines represent 1000 bootstrapped curves for each return period. The return period curves were used to determine the range and probability of boundary conditions in XB-NH. The boundary condition wave and water levels for XB-NH simulations are shown by the large colored dots. Color of the large dots represents interpolated return period for the water level and wave height combination. Yellow indicates short return period,

or high probability, and red indicates long return period, or low probability. Thus, high water levels paired with large wave are less probable (red) than low water levels and with smaller waves (yellow). 122

Figure 4.4 Location of transects (left column), bathymetry and elevation of the existing (middle column) and simulated horizontal levees with varying slopes (right column). Rows show groups of transects with similar bathymetry. 123

Figure 4.5 Joint probability return-period curves of co-occurring wave height and water levels on transect 37, with current sea level (yellow), 0.5 (orange) and 1 m of SLR (red). The black vertical line shows the levee crest height on transect 37. As sea levels rise, low probability events will become increasingly probable. An example of this increase in probability is shown by the gray star, which marks where with 0 m SLR 1:100 year event will cause the same wave and water level conditions as a 0.5 m SLR 1:2 year event. Thus, 0.5 m SLR makes 1:100 year storm conditions 50 times more probable. 125

Figure 4.6 Cumulative levee overtopping on three different transects (rows) and with three different sea level rise (SLR) scenarios (columns). Water level is on the x-axis of all subplots and wave height is on the y-axis of all subplots. Color represents the magnitude of cumulative overtopping greater than 500 L/m at the given water level and wave combination. This threshold is identified as the structural design overtopping limit of levees of a design typical in San Francisco Bay. In all three transects, overtopping that surpasses the structural design of the levee system becomes increasingly probable with sea level rise, shown by the expanding colored area going from left to right..... 126

Figure 4.7 Cumulative overtopping on transect 14, with six different adaptation options shown in columns (a - f) and three different sea level scenarios shown in rows (1-3). The colored areas in columns (a – f) show overtopping greater than 500 L/m..... 128

Figure 4.8 The probability of exceeding structural design thresholds of the levee on all 48 transects with five different adaptation options. The top row shows probability of exceeding q > 10 L/m/s; and the bottom row shows probability of exceeding Q > 500 L/m. Each column shows a different sea level rise scenario. The color of the dots signifies the adaptation option. Across the study region, the general trend shows that increasingly gradually sloped horizontal levees reduce the probability of exceeding the structural design thresholds. HL stands for horizontal levee in the legend. 129

Figure 4.9 Decrease in probability of exceeding two different levee structural design thresholds due to horizontal levee implementation. The color of each transect signifies the decrease in failure risk delivered by implementing a 1:100 sloping horizontal levee. The top row shows the decrease in risk of exceeding 10 L/m/s and the bottom row shows the decrease in risk of exceeding 500 L/m. The three different columns show three different sea

level scenarios. Green transects show places where horizontal levees are reducing the probability of levee failure by the greatest amount, reaching up to 30% in reduction of failure risk. The white star signifies two hotspots where horizontal levees are particularly effective. In both the top and the bottom row, horizontal levees decrease risk of overtopping. Horizontal levees play a stronger role as sea levels rise, shown by the increasing number of colored and dark colored transects, going from left to right. White stars in the top right plot denote hotspots of highest risk reduction from horizontal levees. 130

Figure 4.10 Bathymetry of transects in the two hotspots denoted in Figure 4.9, where horizontal levees provide the greatest risk reduction benefits. Hotspot 1 corresponds to the northwest star and hotspot 2 corresponds to the southeast star. In both hotspots the present levee drops off to relatively deep water, with little to no marsh habitat offshore from the existing levee. 131

Figure S1.1 In column A, examples of bursts with good model-data agreement, and in column B, examples of bursts with poor model-data agreement. Wave height is on the y axis and cross-shore distance is on the x axis. Red dots show observed wave height, and black dots show modeled wave height, both calculated spectrally from variance density time series at observation points. The black line shows estimated wave height along the whole transect, which is estimated by the variance in water level. In subplot 1B, modeled wave height at station SPD, which is at the edge of the low marsh, is higher than the observed wave height. In subplot 2B, modeled wave height at station DX2, which is at the edge of the first transition zone, is higher than observed wave height. Discrepancies in subplots 1B and 2B could be due to non-shore-normal wave direction in the observations, which the XBeach simulations do not include. In subplot 3B, modeled wave height at stations SPD, DX1, and DX are lower than observed wave heights. This could be due to wind-driven wave growth along the transect, which is reported in Foster-Martinez et al. (2018) and which the XBeach simulations do not include. 149

Figure S2.2 Observed (red) and modeled (blue) amplitude (cm, row 1) and phase (degrees, row 2) of the top five tidal constituents in the model; vector difference between observed and modeled tidal constituents (cm, row 3). 152

Figure S2.3 Calibration (rows 1 and 2) and validation (rows 3 and 4) time series, comparing model data (blue) and observations (red) at the Redwood City tide gauge (rows 1 and 3) and at a water logger deployed in Laumeister Marsh (rows 2 and 4). Skill scores include bias, root mean square error (RMSE) and mean absolute error (MAE). 153

List of tables

Table 1-1 Vegetation parameters used in the model calibration. Values for stem diameter, vegetation height, and stems/m^2 for the low and high marsh are taken from the field surveys done by Foster-Martinez et al. (2018). Stem diameter and vegetation height for the transition zones are linearly interpolated from the high and low marsh, based on proportional vegetation cover of the two main vegetation species. Stem density for the transition zones is determined by back-calculating from the $N \times B_v$ values listed in Table 1 of Foster-Martinez et al. (2018). Values of drag coefficient (C_d) are the mean of values calculated by Foster-Martinez et al. (2018) from the winter deployment, except for the low marsh Cd, which is from the summer deployment. 22

Table 1-2 A summary of marsh parameters observed in a 2013 regional survey done by Takekawa et al. (2013), followed by a summary of vegetation parameters found in existing literature. 26

Table 1-3 A summary of vegetation parameters used in the schematized experimental model runs, followed by a summary of the range of parameters that were varied in the schematized experimental runs. In the bottom half of the table, an asterisk denotes variables that were covaried in all simulations. 30

Table 2-1 (A) Property and (B) people protected by marsh restoration in San Mateo County under 3 different sea level rise (SLR) scenarios. Present value is calculated assuming a 50-yr project lifespan, with discount rates of 4, 7, and 10%. 75

Table 4-1 Limits for wave overtopping and structural design of breakwaters, seawalls, dikes, and dams from Van der Meer et al. (2018). Italicized text represents the design type and associated limits which are most relevant for this study, which is focused vegetated levee crests with relatively small significant wave heights. 124

Table S1-1 Summary of scatter index scores for modeled versus observed wave heights with different model settings. Scores are shown at each observation point for the calibration and validation time periods in the two columns on the left. Model settings are shown in the top row and include: Manning friction coefficient (varied from 0.016 to 0.020, per the range of values recommended in Chow 1959); maximum wave steepness before breaking (varied from 0.3 to 0.8, per the range of values recommended in the XBeach user manual); Cd values for the four vegetation zones (varied from mean values - 1 standard deviation to mean values + 1 standard deviation, or [0, 0.11, 0.31, 0.4] to [0.75, 0.77, 0.81, 1.46] from low marsh to high marsh); and bathymetry, including a 5 m LEAN corrected DEM which was developed to account for the height of vegetation above bed level (K. Buffington and Thorne 2018) but

which under-estimates bed level in the marsh, a 2 m DEM (Danielson et al. 2016) which is the highest resolution DEM available and which over-estimates bed level in the marsh, and the 2 m DEM corrected for discrepancies with a linear interpolation. The bottom row, which is bolded, shows the overall skill score, weighted equally across the six observation stations. Skill scores show that model results are relatively insensitive to changes in Manning friction coefficient and maximum wave steepness. Skill scores show that model sensitivity to bathymetry is similar to sensitivity to changes in Cd coefficients of one standard deviation. 150

Table S2-2 Indicators and rank of social vulnerability as determined by BCDC Adapting to Rising Tides “Vulnerable Communities” (BCDC et al., 2020). 154

Table S2-3 On top, annual expected damages (property loss and people flooded) with existing and restored habitat under 3 different SLR scenarios. On the bottom, total and percentage of protected people and property with existing and restored habitat under 3 different SLR scenarios. 154

Abstract

A numerical modeling approach to investigate opportunity for nature-based shorelines in urban estuaries

Rae Taylor-Burns

Urban estuaries are at risk of increased flooding due to storms and accelerating sea level rise (SLR) caused by anthropogenic climate change. This high and rising risk is forcing coastal communities to develop adaptation strategies. While gray infrastructure (walls, levees, berms) has historically been used to protect coastal communities from flooding, over recent decades nature-based solutions have emerged as a management approach to adapt to increasing flood risk. However, nature-based solutions have yet to be widely treated with the same rigor as traditional engineering solutions, both in hydrodynamic modeling and in policy related to urban planning and flood risk management. This dissertation uses coastal engineering and risk management tools, social and economic data, and stakeholder and practitioner perspectives to assess the utility and limitations of marsh habitat conservation and restoration as a flood defense strategy in the largest urban estuary in California, San Francisco Bay. This suite of research shows that marsh conservation and restoration can be cost-effective paths to reduce coastal flood risk in an era of global climate change and accelerating SLR, providing community safety and co-benefits including improved habitat, carbon sequestration, and recreation opportunities. Results support policy that facilitates conservation and restoration of existing and historical marsh habitat and incorporates habitat and green infrastructure into risk science and insurance.

Acknowledgements

Thank you to my three advisors:

- Thank you, Patrick, for taking a chance on me and allowing me to take ownership of my research questions. Your unwavering support and trust have been a gift over the past five years.

- Thank you, Chris, for being a constant source of ideas and positivity. You have helped me see a path through frustration so many times and I am lucky to have had the opportunity to learn from your approach to science and to life.

- Thank you, Mike, for welcoming me to your team and your world, and for showing me how science can support management and policy action. I am so grateful to have you as a mentor.

Thank you to the Coastal Impacts-Climate Processes Team at USGS, and my two labs on campus, the Physical Oceanography lab group, and the Coastal Resilience Lab. I am so fortunate to have been a part of three wonderful research groups, each filled with friends and teachers. Thank you to Andy Moore for thoughtful discussion and helpful ideas. Thank you to Curt Storlazzi for helping me formulate my ideas from the start. Thank you to Li Erikson, Andy O'Neill, Amy Foxgrover, and Jessie Lacy, and Juliette Finzi-Hart for your mentorship and patience; you are all role models to me.

Thank you to Babak, Kees, Camila, Borja, and David for technical support. I have learned so much about modeling and computing from all of you, and nothing in the following pages would have been possible without the time you have so generously shared with me.

Thank you to my wonderful parents, who are firm believers in the power of hard work and an excellent education and have always supported my dreams.

Thank you to Brian for being my partner in life and making every day brighter and more full of laughs and adventure.

This dissertation includes reprints of previously published and submitted work:

R. Taylor-Burns, C. Nederhoff, J. Lacy and P.L. Barnard. The influence of vegetated marshes on wave transformation in sheltered estuaries. Coastal Engineering 184 (2023).

R. Taylor-Burns, C. Lowrie, B. Tehranirad, J. Lowe, L. Erikson, P. Barnard, B. G. Reguero, M. W. Beck. The value of mash restoration for climate adaptation in an urban estuary. In review at Scientific Reports

R. Taylor-Burns and B.G. Reguero. “Exploring limitations of marsh restoration for flood reduction”. American Society of Civil Engineers: Infrastructure Innovation & Adaptation for a Sustainable and Resilient World, Arlington VA, 16-18 November 2023.

The co-authors P.L. Barnard, M.W. Beck and B.G. Reguero listed in these publications supervised the research which forms the basis for this dissertation. The co-authors C. Nederhoff, C. Lowrie and B. Tehranirad shared technical methodologies. The co-authors J. Lacy and J. Lowe provided field-based insight and data. L. Erikson provided technical direction and theoretical insight.

Introduction

Anthropogenic climate change is raising global sea levels and threatening coasts around the world with increased risk of flooding. Thermal expansion of seawater and melting of land-based ice is predicted to cause between 0.3 and 3 m of sea level rise (SLR) by 2100 (DeConto and Pollard 2016; Sweet et al. 2017; 2022; Le Bars et al. 2017; Masson-Delmotte et al. 2021). In addition to SLR, coastal flooding is amplified by tides, storm-driven surge, waves, and river discharge (Barnard et al. 2019). More than 600 million people live in the coastal zone and that number is expected to increase to more than 1 billion by 2050 (Merkens et al. 2016). These factors combine to create hazard, exposure, and risk for coastal communities around the world, forcing such communities to develop adaptation strategies to mitigate risk.

Historically, flood risk reduction has been primarily achieved with hard human-made structures such as seawalls, levees, and revetments. Seawalls are concrete walls built in front of developed areas and directly receive wave impact, reflecting wave energy back towards the sea and preventing erosion. Levees are earthen walls often built along the banks of rivers or bays, which protect developed areas from flooding. Revetments are similar to retaining walls and serve to stabilize a coast from erosion. These examples of traditional shoreline protection structures each have slightly different purposes but are widely deployed globally and generally serve to reduce flood risk during storms. However, these traditional shoreline protections all fail eventually without maintenance, and many of these approaches disturb, degrade, or destroy coastal habitat. Further, traditional shoreline protections often present tradeoffs such as disrupting sediment transport pathways, accelerating beach erosion, limiting beach-access, and preventing habitat transgression.

Coastal habitat such as coral reefs, mangrove forests and marshes can play a role in increasing resilience to storms and high water levels by buffering incoming waves and storm surge and stabilizing shorelines (Shepard et al. 2011; Ysebaert et al. 2011; Suzuki et al. 2012; Quataert et al. 2015; Narayan et al. 2016; Nowacki et al. 2017; Storlazzi et al. 2019). Research suggests that wetlands reduced damage from Hurricane Sandy by $625 million (Narayan et al. 2017), coral reefs annually protect over 18,000 people (Storlazzi et al. 2019) and $1.8 billion dollars of infrastructure in the USA (Reguero et al. 2021), and mangroves provide $65 billion in flood protection benefits globally each year (Menéndez et al. 2020). Findings like these have caused a recent shift in scientific and management focus to consider, evaluate, and implement nature-based shoreline protection (Powell et al. 2019). However, nature-based solutions to coastal flooding have only recently begun to be treated with the same rigor as traditional engineering solutions, both in hydrodynamic modeling and in policy related to urban planning and flood risk management.

Recent research suggests that in California, 600,000 people are at risk of flooding in a scenario with 2 meters of sea level rise combined with a 100 year storm (Barnard et al. 2019). The population bordering San Francisco Bay ("the Bay Area") accounts for two-thirds of future flooding impacts in California, and the cost of raising regional protection structures to prepare for 2 meters of SLR could reach $450 billion (Hirschfeld and Hill 2017). While the Bay relies heavily on gray infrastructures (primarily levees) for flood protection today, a wide variety of pathways for integrating nature-based shorelines have been identified regionally (Beagle et al. 2019). Coastal development has altered or removed about 90% of the Bay's historical tidal wetlands (Safran et al. 2013), resulting in dramatic habitat loss and

fragmentation and in the past several decades marsh restoration has emerged as a unifying management objective in the Bay (Callaway et al. 2007; Brew and Williams 2010; Callaway et al. 2011; Foxgrover et al. 2019). The coincidence of high and rising flood risk as well as opportunity for wetland conservation and restoration makes San Francisco Bay, CA, well suited to serve as a study site for an investigation of the potential for marsh restoration as a nature-based flood defense. This dissertation uses quantitative engineering approaches to assess how marsh plants and marsh restoration can be strategically used to reduce coastal flood risk in the densely urbanized estuary of San Francisco Bay.

In chapter one, observational data from San Francisco Bay, CA (USA), is used to calibrate and validate a model and establish that the model, XBeach non-hydrostatic, can hindcast wave heights and periods in vegetation fields. Then, through experimental schematized simulations which vary hydrodynamic conditions, vegetation characteristics, and marsh morphology dimensions, this study examines the role of vegetation in influencing wave transformation. The analysis shows how different characteristics of marshes control wave transformation and dynamic water levels, how these characteristics interact, and how the potential of marshes to reduce flooding may change with higher water levels and larger waves. In the range of model settings explored in this chapter, vegetation on a marsh reduces significant wave height by a median of 35 cm and reduces runup by a median of 40 cm. Meaningful reductions in wave height and runup can be achieved even in the narrowest marshes simulated (50 m). Flood managers can use the information presented here to strategically plan for extreme events. For example, under conditions similar to a 100-year storm in San Francisco Bay, 50 m of

marsh vegetation reduces runup by a median of 65 cm. Results demonstrate the importance of maintaining and restoring healthy marshes in urban estuaries.

Chapter two assesses the flood risk reduction benefits of marsh restoration, under current and future climate conditions, to characterize how and where they provide climate adaptation benefits now and into the future. The study is focused in San Mateo County, which has the highest future flood risk in the state and large areas with potential for wetland restoration. Results show that marsh restoration provides flood reduction benefits along shorelines unprotected by levees and along levee sections that are overtopped by high water levels. Countywide marsh restoration provides a present value in avoided damages of $21 million. This value increases to five-fold to $106 million with 0.5 m of sea level rise, and to $500 million with 1 m of sea level rise. Results show that marsh restoration can be a cost effective approach to climate adaptation in one of the most at-risk counties in the U.S. Considering future climate scenarios is becoming common practice with traditional infrastructure solutions (Hallegatte et al. 2013; Aerts et al. 2014; de Ruig et al. 2019), and similar approaches should be taken when assessing the potential of nature-based solutions. This work demonstrates that investments in nature and community resilience made today can result in increasing payoffs as climate change progresses and risk increases.

Chapter two shows that wetland restoration can be effective in reducing flood risk but that that marsh restoration in diked and drained former wetlands can amplify flood levels and overtop levee crests in some instances. Therefore, exploring how marsh restoration in diked and drained former wetlands like the San Francisco Bay salt ponds can be strategically

executed to maintain community safety is a necessary next step. In chapter three, I explore how restoration scenarios in one of the salt ponds of in San Francisco Bay could influence flooding in the future and provide guidance on the factors that should be considered when restoring diked and drained former wetlands. This work combines high fidelity numerical modeling with a simplified model built on the shallow water equations for tidal inlets to understand the controlling factors and the effects of sea level rise. The simplified model is applicable in other contexts. With a case study in San Francisco Bay, this work aims to inform wetland restoration in other geographies. These simulations demonstrate that the width of the tidal inlet and the bathymetry modifications of the restoration site are key drivers of water levels. Both factors can be controlled but are rarely considered when planning restorations. These results are timely for the Bay Area and beyond as regional and national priorities shift to investing in nature-based climate solutions (Olander et al. 2022).

Finally, chapter four applies the model developed in chapter one to a specific region, the bay shore of San Mateo County. This analysis is a first look at how nature-based climate adaptation measures can increase levee system safety with sea level rise in an area with high population density. Horizontal levees comprise a gently sloping vegetated area fronting a buried levee. The plants on the horizontal levee can provide wave attenuation benefits as well as habitat benefits. Here, a hydrodynamic model, XBeach non-hydrostatic (XB-NH), is used to assess the stability and sustainability of existing levees and determine how hybrid nature-based climate adaptation measures can reduce the risk of levee failure in San Francisco Bay. Various horizontal levee configurations are implemented in the numerical model under a variety of sea level and wave conditions and compare overtopping rates of the

existing levee and of the horizontal levee configuration to assess how horizontal levees perform in reducing flood risk, both with present day conditions and with SLR. Results show that the risk of levee failure can be reduced by up to 30% with horizontal levels. Further, the analysis provides insight to horizontal levee design considerations and a methodological approach to adapt levees to prepare for SLR in urban estuaries.

Altogether, this suite of work establishes that marsh habitat can play a strong role in increasing resilience to climate change in low-lying urban estuaries with high and rising flood risk. Marsh plants can meaningfully reduce wave heights, even across narrow fringing marsh areas, reducing risk of overtopping levees and extending the viability of the levee system into the future. Marsh restoration can provide net-positive economic benefits in some places, purely through reduction of flood damages. Results support policy that facilitates conservation and restoration of existing and historical marsh habitat and incorporates habitat and green infrastructure into risk science.

References

Aerts, Jeroen C.J.H., W. J.Wouter Botzen, Kerry Emanuel, Ning Lin, Hans De Moel, and Erwann O. Michel-Kerjan. 2014. "Climate Adaptation: Evaluating Flood Resilience Strategies for Coastal Megacities." *Science* 344 (6183): 473–75. https://doi.org/10.1126/science.1248222.

Barnard, Patrick L, Li H Erikson, Amy C Foxgrover, Juliette A Finzi Hart, Patrick Limber, Andrea C O Neill, Maarten Van Ormondt, et al. 2019. "Dynamic Flood Modeling Essential to Assess the Coastal Impacts of Climate Change." *Nature Scientific Reports* 9. https://doi.org/10.1038/s41598-019-40742-z.

Bars, Dewi Le, Sybren Drijfhout, and Hylke De Vries. 2017. "A High-End Sea Level Rise Probabilistic Projection Including Rapid Antarctic Ice Sheet Mass Loss." *Environmental Research Letters* 12 (4). https://doi.org/10.1088/1748-9326/aa6512.

Beagle, Julie, Jeremy Lowe, Katie McKnight, Sam Safran, Laura Tam, and Sarah Jo Szambelan.

2019. “San Francisco Bay Shoreline Adapation Atlas: Working with Nature to Plan for Sea Level Rise Using Operational Landscape Units.”

Brew, David S., and Philip B. Williams. 2010. “Predicting the Impact of Large-Scale Tidal Wetland Restoration on Morphodynamics and Habitat Evolution in South San Francisco Bay, California.” *Journal of Coastal Research* 265 (265): 912–24. https://doi.org/10.2112/08-1174.1.

Callaway, John C., V. Thomas Parker, Michael C. Vasey, Lisa M. Schile, and Ellen R. Herbert. 2011. “Tidal Wetland Restoration in San Francisco Bay: History and Current Issues.” *San Francisco Estuary and Watershed Science* 9 (3). https://doi.org/10.15447/sfews.2011v9iss3art2.

Callaway, John C., V. Thomas Parker, Michael C. Vasey, and Lisa M. Schile. 2007. “Emerging Issues for the Restoration of Tidal Marsh Ecosystems in the Context of Predicted Climate Change.” *Madroño* 54 (3): 234–48. https://doi.org/10.3120/0024-9637(2007)54[234:eiftro]2.0.co;2.

DeConto, Robert M., and David Pollard. 2016. “Contribution of Antarctica to Past and Future Sea-Level Rise.” *Nature* 531 (7596): 591–97. https://doi.org/10.1038/nature17145.

Foxgrover, Amy C., Mark Marvin-DiPasquale, Bruce E. Jaffe, and Theresa A. Fregoso. 2019. “Slough Evolution and Legacy Mercury Remobilization Induced by Wetland Restoration in South San Francisco Bay.” *Estuarine, Coastal and Shelf Science* 220 (August 2018): 1–12. https://doi.org/10.1016/j.ecss.2019.02.033.

Hallegatte, Stephane, Colin Green, Robert J. Nicholls, and Jan Corfee-Morlot. 2013. “Future Flood Losses in Major Coastal Cities.” *Nature Climate Change* 3 (9): 802–6. https://doi.org/10.1038/nclimate1979.

Hirschfeld, Daniella, and Kristina E. Hill. 2017. “Choosing a Future Shoreline for the San Francisco Bay: Strategic Coastal Adaptation Insights from Cost Estimation.” *Journal of Marine Science and Engineering* 5 (3): 42. https://doi.org/10.3390/jmse5030042.

Masson-Delmotte, V., P. Zhai, A. Pirani, S.L. Connors, C. Péan, S. Berger, N. Caud, et al. 2021. “IPCC, 2021: Summary for Policymakers. In: Climate Change 2021: The Physical Science Basis. Contribution of Working Group I to the Sixth Assessment Report of the Intergovernmental Panel on Climate Change.” *Cambridge University Press*.

Menéndez, Pelayo, Iñigo J. Losada, Saul Torres-Ortega, Siddharth Narayan, and Michael W. Beck. 2020. “The Global Flood Protection Benefits of Mangroves.” *Scientific Reports* 10 (1): 1–11. https://doi.org/10.1038/s41598-020-61136-6.

Merkens, Jan-ludolf, Lena Reimann, Jochen Hinkel, and Athanasios T Vafeidis. 2016. “Gridded Population Projections for the Coastal Zone under the Shared Socioeconomic Pathways.” *Global and Planetary Change* 145: 57–66. https://doi.org/10.1016/j.gloplacha.2016.08.009.

Narayan, Siddharth, Michael W. Beck, Borja G. Reguero, Iñigo J. Losada, Bregje Van Wesenbeeck, Nigel Pontee, James N. Sanchirico, Jane Carter Ingram, Glenn Marie

Lange, and Kelly A. Burks-Copes. 2016. “The Effectiveness, Costs and Coastal Protection Benefits of Natural and Nature-Based Defences.” *PLoS ONE* 11 (5): 1–17. https://doi.org/10.1371/journal.pone.0154735.

Narayan, Siddharth, Michael W. Beck, Paul Wilson, Christopher J. Thomas, Alexandra Guerrero, Christine C. Shepard, Borja G. Reguero, Guillermo Franco, Jane Carter Ingram, and Dania Trespalacios. 2017. “The Value of Coastal Wetlands for Flood Damage Reduction in the Northeastern USA.” *Scientific Reports* 7 (1): 1–12. https://doi.org/10.1038/s41598-017-09269-z.

Nowacki, Daniel J., Alexis Beudin, and Neil K. Ganju. 2017. “Spectral Wave Dissipation by Submerged Aquatic Vegetation in a Back-Barrier Estuary.” *Limnology and Oceanography* 62 (2): 736–53. https://doi.org/10.1002/lno.10456.

Olander, Lydia, Krystal Laymon, and Heather Tallis. 2022. “Opportunities to Accelerate Nature-Based Solutions : A Roadmap for Climate Progress , Thriving Nature , Equity, & Prosperity. A Report to the National Climate Taskforce.,” no. November: 1–44.

Powell, Emily J., Megan C. Tyrrell, Andrew Milliken, John M. Tirpak, and Michelle D. Staudinger. 2019. “A Review of Coastal Management Approaches to Support the Integration of Ecological and Human Community Planning for Climate Change.” *Journal of Coastal Conservation* 23 (1): 1–18. https://doi.org/10.1007/s11852-018-0632-y.

Quataert, Ellen, Curt Storlazzi, Arnold van Rooijen, Olivia Cheriton, and Ap Dongeren. 2015. “The Influence of Coral Reefs and Climate Change on Wave-Driven Flooding of Tropical Coastlines” 42: 6407–15. https://doi.org/10.1002/2015GL064861.Received.

Reguero, Borja G, Curt D Storlazzi, Ann E Gibbs, James B Shope, Aaron D Cole, Kristen A Cumming, and Michael W Beck. 2021. “The Value of US Coral Reefs for Flood Risk Reduction.” *Nature Sustainability* 4 (8): 688–98. https://doi.org/10.1038/s41893-021-00706-6.

Ruig, Lars T. de, Patrick L. Barnard, W. J.Wouter Botzen, Phyllis Grifman, Juliette Finzi Hart, Hans de Moel, Nick Sadrpour, and Jeroen C.J.H. Aerts. 2019. “An Economic Evaluation of Adaptation Pathways in Coastal Mega Cities: An Illustration for Los Angeles.” *Science of the Total Environment* 678: 647–59. https://doi.org/10.1016/j.scitotenv.2019.04.308.

Safran, Sam, April Robinson, Julie Beagle, Marcus Klatt, Kristen Cayce, and Robin Grossinger. 2013. “A Landscape Ecology Analysis of San Francisco Bay-Delta Marsh Then (1850) and Now.” Richmond, CA.

Shepard, Christine C., Caitlin M. Crain, and Michael W. Beck. 2011. “The Protective Role of Coastal Marshes: A Systematic Review and Meta-Analysis.” *PLoS ONE* 6 (11). https://doi.org/10.1371/journal.pone.0027374.

Storlazzi, Curt D, Borja G. Reguero, Aaron D. Cole, Erik Lowe, James B. Shope, Ann E. Gibbs, Barry A. Nickel, Robert T. McCall, Ap R. van Dongeren, and Michael W. Beck. 2019. “Rigorously Valuing the Role of U . S . Coral Reefs in Coastal Hazard Risk Reduction: U.S. Geological Survey Open File Report 2019-1027.” https://doi.org/10.3133/ofr20191027.

Suzuki, Tomohiro, Marcel Zijlema, Bastiaan Burger, Martijn C. Meijer, and Siddharth Narayan. 2012. “Wave Dissipation by Vegetation with Layer Schematization in SWAN.” *Coastal Engineering* 59 (1): 64–71. https://doi.org/10.1016/J.COASTALENG.2011.07.006.

Sweet, W. V., R. E. Kopp, C. P. Weaver, J. Obeysekera, R. M. Horton, E. R. Thieler, and Chris Zervas. 2017. “Global and Regional Sea Level Rise Scenarios for the United States,” no. NOS CO-OPS 083: 75. https://tidesandcurrents.noaa.gov/publications/techrpt83_Global_and_Regional_SLR_Scenarios_for_the_US_final.pdf.

Sweet, W.V., B.D. Hamlington, R.E. Kopp, C.P. Weaver, P.L. Barnard, D. Bekaert, W. Brooks, et al. 2022. “Global and Regional Sea Level Rise Scenarios for the United States: Updated Mean Projections and Extreme Water Level Probabilities along U.S. Coastlines.”

Ysebaert, Tom, Shi Lun Yang, Liquan Zhang, Qing He, Tjeerd J. Bouma, and Peter M.J. Herman. 2011. “Wave Attenuation by Two Contrasting Ecosystem Engineering Salt Marsh Macrophytes in the Intertidal Pioneer Zone.” *Wetlands* 31 (6): 1043–54. https://doi.org/10.1007/s13157-011-0240-1.

1. The influence of vegetation on wave transformation in sheltered estuaries

Abstract

Assessing the influence of marshes on mitigating flooding along estuarine shorelines under the pressures of sea level rise requires understanding wave transformation across the marsh. A numerical model was applied to investigate how vegetated marshes influence wave transformation. XBeach non-hydrostatic (XB-NH) was calibrated and validated with high frequency pressure data from the marsh at China Camp State Park in San Pablo Bay, California (USA). The model was used to examine how marsh and hydrodynamic characteristics change the potential for marshes to mitigate wave driven flooding. Model results demonstrate that hydrodynamics, vegetation, and marsh width influence wave transformation most, while marsh morphology parameters such as elevation and slope had least effect. Results suggest that in the range of settings explored here (incident wave heights ranging from 0.5 to 3 m and water levels ranging from current mean higher high water to 3 m above current mean higher high water), in comparison to wave propagation over an unvegetated mudflat, marsh vegetation reduces runup by a median of 40 cm and wave height by a median of 35 cm. Results illustrate how marshes can be strategically utilized to provide flood reduction benefits.

1.1 Introduction

Climate change is raising global sea levels and threatening coasts around the world with increased risk of flooding. Thermal expansion of seawater and melting of land-based ice is predicted to cause between 0.3 and 3 m of sea level rise (SLR) by 2100 (DeConto and Pollard 2016; Sweet et al. 2017; 2022; Le Bars et al. 2017; Masson-Delmotte et al. 2021), which will significantly increase coastal flood risk (Vitousek et al. 2017; Taherkhani et al. 2020). In

addition to SLR, coastal flooding is amplified by tides, storm-driven surge, waves, and river discharge (Barnard et al. 2019). Disproportionate population density in coastal areas further compounds this risk. More than 600 million people live in the coastal zone and that number is expected to increase to more than 1 billion by 2050 (Merkens et al. 2016). These factors combine to create hazard, exposure, and risk for coastal communities around the world. Coastal habitat such as coral reefs, mangrove forests and marshes can play a role in increasing resilience to storms and high water levels by buffering incoming waves and storm surge and stabilizing shorelines (Shepard et al. 2011; Ysebaert et al. 2011; Suzuki et al. 2012; Quataert et al. 2015; Narayan et al. 2016; Nowacki et al. 2017). Research suggests that wetlands reduced damage from Hurricane Sandy by $625 million (Narayan et al. 2017), coral reefs annually protect over 18,000 people (Storlazzi et al. 2019) and $1.8 billion dollars of infrastructure in the USA (Reguero et al. 2021), and mangroves provide $65 billion in flood protection benefits globally each year (Menéndez et al. 2020). Incorporating vegetation into levee systems on a global scale can reduce required levee height and result in cost savings on the order of $300 billion (van Zelst et al. 2021). Findings like these have caused a recent shift in scientific and management focus to nature-based shoreline protection (Powell et al. 2019).

Though coastal habitats have been shown to be effective in reducing flooding, projected sea level rise is anticipated to squeeze coastal habitat; for example, a morphological study of San Francisco Bay suggests that intertidal areas will drown with 21st century SLR (Elmilady et al. 2019), though this response depends on sediment supply, location, and morphology. A marsh with sufficient sediment supply may continue to accrete sediment on the marsh platform, raising its elevation gradually (Kirwan et al. 2010; Swanson et al. 2014). A marsh may also

respond to rising water levels with landward retreat of vegetation zones (Stralberg et al. 2011; Bigalbal et al. 2018), or lateral erosion and steepening of the marsh edge (Tommasini et al. 2019). Marshes that cannot keep up or migrate may lose vegetation density and transition to mudflat as the inundation periods begin to exceed the tolerance of marsh plants (Stralberg et al. 2011; Schile et al. 2014).

Wave energy on coasts dissipates through several processes. In the inner shelf and shoreface, dissipation occurs due to bottom friction (Putnam and Johson 1949), percolation (meaning transfer of energy into a permeable bottom; Putnam 1949; Shemdin et al. 1978), fluctuation in the bed level (Putnam and Johson 1949), and white capping (Hasselmann 1974); these processes can reduce wave energy significantly before waves ever begin to break. As waves enter the surf zone, turbulence due to depth-induced wave breaking is the primary driver of wave energy dissipation, though bottom friction also plays a role. There is great variation in energy loss due to breaking, depending on factors including surf zone morphology, infragravity energy, and breaker type (Wright and Short 1984). Finally, once waves reach the swash zone, energy loss occurs due to turbulence, bottom friction, and percolation (Stutz et al. 1998). Though swash, which is defined as the movement of water up the shore after the breaking of a wave, represents only a small fraction of the initial energy of waves, it can cause coastal morphology change and property damage.

Plants can reduce wave energy via work done by frictional drag. Vegetation induced wave attenuation has been studied extensively, in field (Foster-Martinez et al. 2018; Garzon et al. 2019) and lab experiments (Bouma et al. 2013; Maza et al. 2015), as well as with empirical (Mendez and Losada 2004) and physical models (Suzuki et al. 2012; Ma et al. 2013). The

amount of drag plants provide depends on hydrodynamic conditions (Mendez and Losada 2004; Callaghan et al. 2010; Foster-Martinez et al. 2018) and vegetation characteristics (Foster-Martinez et al. 2018). Dalrymple et al. (1984) developed an expression to describe energy dissipation of waves through a vegetated field, treating the vegetation elements as rigid cylinders, and subsequently that expression was modified for a random wave field by Mendez and Losada (2004), who also developed an analytical solution for shallow-water waves with a sloped water depth. The work of Mendez and Losada (2004) applies only to submerged plants, which are relatively short and stiff (such as marsh plants and some types of sea grass), and not to vegetation with low stiffness and high buoyancy (such as certain types of kelp), though it has been applied to vegetation with low stiffness.

The formulation developed by Mendez and Losada (2004) is the basis of wave attenuation in the XBeach model (van Rooijen et al. 2015). This formulation paired with the recent development of the XBeach non-hydrostatic mode, which, though computationally costly, is resolved for incident-band waves, (XB-NH; de Ridder et al. 2020) enables a first look at the impact of vegetation on incident-band (i.e., short period or high frequency) driven wave runup, which is the sum of wave setup and swash (Miche 1951; Longuet-Higgins and Stewart 1963; Guza and Thornton 1981; Stockdon et al. 2006). Runup requires high frequency (wave resolved) data to observe, and in the past has been observed using time series imagery (Stockdon et al. 2006), which is challenging to collect. Though runup is a direct indicator of maximum coastal flooding, and is thus a key consideration in coastal planning, the interactions of wave runup (measured vertically) and vegetation are not well understood and have only recently begun to be studied (van Wesenbeeck et al. 2022). Previous studies have

determined that wave height decay across vegetation fields depends on variables including water level, vegetation height, wave height, and frictional coefficient (Foster-Martinez et al. 2018; Garzon et al. 2019). However, other aspects of marsh morphology have not been considered, such as marsh platform elevation relative to tidal datum, mudflat and marsh edge slope, and marsh width. Furthermore, interactions between these variables have not been examined.

This study employs observational data from San Francisco Bay, California (USA), to calibrate and validate a model and establish that XB-NH can hindcast wave heights and periods in vegetation fields. Then, through experimental schematized simulations which vary hydrodynamic conditions, vegetation characteristics, and marsh morphology dimensions, this study examines the role of vegetation in reducing flooding potential. The analysis shows which characteristics of marshes control wave transformation and dynamic water levels, how these characteristics interact, and how the potential of marshes to reduce flooding may change with higher water levels.

1.2 Methods

1.2.1 Study site

In the winter of 2014-2015, and the summer of 2016, Foster-Martinez et al. (2018) performed vegetation surveys and deployed pressure sensors along a transect in China Camp State Park (38.0095°, -122.4837°), in San Pablo Bay, in the northwest corner of San Francisco Bay (Figure 1.1). They characterized the marsh with four different vegetation zones: a low marsh, characterized by *Spartina foliosa*; a high marsh, characterized by *Salicornia pacifica*;

and two transition zones, characterized by combinations of the two vegetation species. Vegetation surveys were conducted on January 23, 2015, and June 6, 2016, using one-meter quadrats to determine percent cover of each species and average and maximum canopy heights, which were determined by measuring the height of the tallest and a typical stem, and quarter-meter quadrats to determine stem count and stem diameter measurements. These values were measured for the high marsh and low marsh zones and interpolated linearly for the transition zones based on percent cover of high and low marsh vegetation. Pressure sensors were deployed on a 150 m transect, starting 35 m outside the marsh on the mudflat, and extending into the marsh, placed at the boundaries of the vegetation zones. These sensors collected data at either 6 or 8 Hz in bursts of measurements every 10 or 15 minutes. Bursts were 2048 measurements long, which is approximately 5 minutes at the given measurement frequencies. These data are publicly available (Lacy et al. 2017) and were utilized to calibrate and validate an XB-NH model. To convert total pressure to water depth, a constant water density was assumed, and atmospheric pressure was temporally interpolated from measurements taken at the NOAA RCMC1 weather station, which is 11.5 km from the site, and subtracted from total pressure. A spectral analysis was used to determine variance density from pressure time series, and variance density (from which wave statistics such as peak wave period Tp, significant wave height Hs or Hm_0 can be calculated) was used to force calibration and validation model runs.

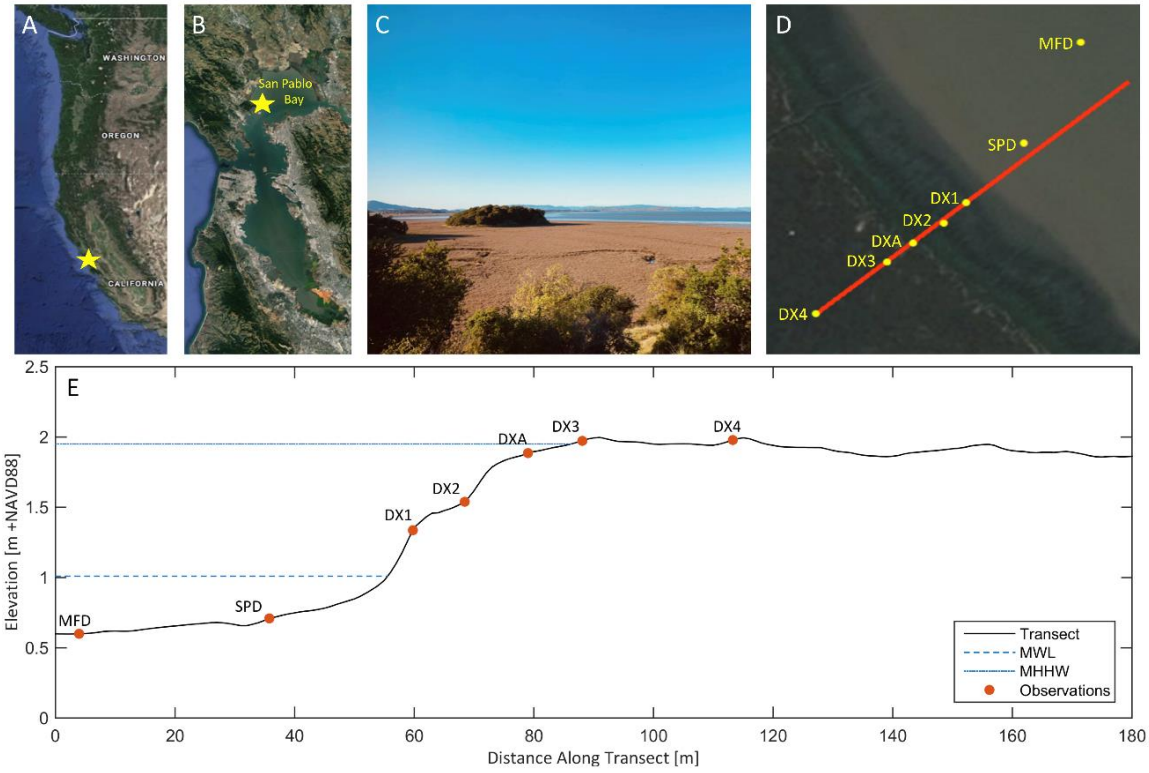

Figure 1.1 Location (A and B; base-map layer from Google Earth) and view (C; photograph taken by R. Taylor-Burns) of the study site, and depiction of the transect deployed in 2016 by Lacy et al. (2017; D and E). MDF is the offshore site, SPD marks the beginning of the low marsh, DX1 marks the beginning of the first transition zone, DX2 marks the beginning of the second transition zone, and DXA – DX4 are all on the high marsh.

1.2.2 Model and data sources

XBeach (Roelvink et al. 2009) is a process-based model which simulates nearshore processes including wave transformation, wave-induced setup, over-wash, and inundation; in addition to information on water levels and wave heights, model outputs can include parameters such as flow and orbital velocity, bed shear stress, and Stokes drift. XBeach was originally developed as a phase-averaged model that resolves amplitude variation on the wave group scale (surfbeat) but does not resolve individual waves as in a Boussinesq model. Recently, a non-hydrostatic mode (XB-NH) was developed for XBeach (de Ridder et al. 2020), which is

similar to a depth-averaged version of the SWASH model (Zijlema et al. 2011; Smit et al. 2013) and is able to fully resolve incident-band waves. Resolution of incident-band waves, though computationally costly, is necessary to determine swash on relatively steep slopes and is thus necessary to investigate runup (as determined by the last wet grid cell), and potential overtopping on levees. Runup and overtopping in the non-hydrostatic mode have been validated using several separate datasets from sandy beaches. Results show that incident-band driven runup height is predicted with good accuracy and a maximum deviation of 15% (Roelvink et al. 2018). A reduced two-layer non-hydrostatic formulation is included that allows for a more accurate description of the frequency dispersion in relatively deeper water. Relative depth (KD) determines whether waves are in deep water (waves do not interact with the bottom, $KD > \pi$) or shallow water (waves interact with the bottom, $KD < \pi/10$), and is based on water depth and wavelength. De Ridder et al. (2020) showed good performance up to a relative depth of 3. XB-NH allows for the inclusion of the effect of vegetation within the model via vegetation parameters including stem density, frictional drag coefficient, stem height, and stem diameter (van Rooijen et al. 2015; 2016).

In this study, XB-NH was applied in one-dimensional mode. This approach assumes that wave forcing is shore-normal and neglects lateral flow, assumptions which were also made in the analysis by Foster-Martinez et al. (2018). This approach also neglects tidal channels and creeks, which facilitate drainage of water on the marsh. Model boundary conditions were determined by obtaining wave statistics from every burst at the offshore observation station, MFD (Figure 1.1). Bathymetry was determined from a 2 m digital elevation model (DEM), which was collected aerially with Light Detection and Ranging (LiDAR, Danielson et al. 2016).

Discrepancies between elevations at the study sites in the DEM and elevations reported by Lacy et al. (2017) ranged from 0 to 20 cm, with largest discrepancies in the high marsh zone. These discrepancies are likely due to LiDAR overestimating elevation in dense vegetation. A vegetation-corrected DEM (only available at elevations above -1 m NAVD88) was also tested (Buffington and Thorne 2018), but it also had discrepancies and had lower spatial resolution (5 m) and thus was not used. To correct for vertical discrepancies between field observations and the 2 m DEM, a linear interpolation of the discrepancies was created and subtracted from the DEM.

Variable grid spacing was used, with a minimum of 30 grid points per wavelength and the total number of grid points ranging from 1500 to 19,000. Sensitivity analyses show that the model results converge at this resolution. A Manning's friction formulation was used for mudflat friction. The equilibrium bound long wave, which is energy that fluctuates at the same frequency as the wave group but 180 degrees out of phase, was not imposed in the calibration or validation as this saved significant computational time and did not impact model results. In contrast to open-coast conditions, offshore spectra in this sheltered environment do not show components of bound long waves in the variance density spectrum. We hypothesize that this is related to the relatively young age of the sea-state in combination with steep slope compared to wave period in San Pablo Bay. To determine wave statistics from water level time series, a Guza filter (Guza et al. 1984) was used to separate incoming and outgoing wave energy. A fast Fourier transform was used to determine wave spectra from water level time series. Significant wave height and peak period were determined from wave spectra. The last wet grid cell was utilized to determine a runup time

series and the 98th percentile of this time series was utilized to determine R2%, or the runup value which is exceeded by 2% of waves.

1.2.3 Calibration and validation

Bursts for which the significant wave height was greater than 5 cm at the offshore station (MFD), and for which ratio of wave group velocity to phase velocity (c_g/c_p, or N) was less than 0.85 at the offshore station, were selected for calibration and validation in order enable us to model meaningful decay of wind waves with deep water boundary conditions. Few bursts during the summer deployment met these conditions, so the model was developed using winter measurements, with the calibration dataset from January 15 –25, 2015 (n = 257), and the validation dataset from December 18 –28, 2014 (n = 88). For all bursts, the relative depth (KD) was less than 1.5, and the ratio of wave height to water depth was less than 1/3.

The vegetation module of XB-NH was utilized to account for wave-vegetation interactions within the marsh (van Rooijen et al. 2015). Stem height, diameter, and density for each of the four vegetation zones were taken from the vegetation surveys done by Foster-Martinez et al. (2018). That study calculated drag coefficients, C_d, for the four vegetation zones in winter and summer and found, progressing from the bay to the marsh, that the mean and standard deviation of C_d across the four vegetation zones and spanning the full range of water level conditions to be [9.85 ± 19.23, 0.44 ± 0.33, 0.56 ± 0.25, 0.93 ± 0.53] for winter and [0.34 ± 0.41, 0.56 ± 0.19, 0.41 ± 0.10] for summer (there was only one transition zone during the summer deployment). The C_d for the low marsh in winter is very high due to low vegetation frontal area at that time, caused by seasonal loss of leaves (see Figure 4 in Foster-Martinez et al. (2018) for a visual), but similar wave attenuation to the summer months. Foster-Martinez

et al. (2018) discusses possible mechanisms for similar attenuation despite seasonal changes in marsh plants. Additionally, uncertainty for C_d in the low marsh during winter is very high. Because that value is anomalously high, with high uncertainty, and inconsistent with other values reported in the literature, the summer C_d value for the low marsh was used, such that the values of C_d we used across the four vegetation zones were [0.34, 0.44, 0.56, 0.93], respectively. Vegetation parameters for calibration are shown in Table 1-1.

Table 1-1 Vegetation parameters used in the model calibration. Values for stem diameter, vegetation height, and stems/m^2 for the low and high marsh are taken from the field surveys done by Foster-Martinez et al. (2018). Stem diameter and vegetation height for the transition zones are linearly interpolated from the high and low marsh, based on proportional vegetation cover of the two main vegetation species. Stem density for the transition zones is determined by back-calculating from the $N \times B_v$ values listed in Table 1 of Foster-Martinez et al. (2018). Values of drag coefficient (C_d) are the mean of values calculated by Foster-Martinez et al. (2018) from the winter deployment, except for the low marsh Cd, which is from the summer deployment.

Marsh zone	Species	Stem diameter (m)	Vegetation height (m)	Stems/m^2	C_d
Low marsh	*Spartina foliosa*	0.0027	0.16	312	0.34
Transition zone 1	20% *S. foliosa,* 15% *S. pacifica*	0.0024	0.186	5583	0.43
Transition zone 2	5% *S.foliosa,* 55% *S. pacifica*	0.00205	0.215	23,562	0.56
High marsh	*Salicornia pacifica*	0.002	0.22	44,000	0.93

Model results were assessed by comparing modeled and measured wave heights and wave periods. Predictive skill was determined by calculating relative bias (RB), scatter index (SCI), and mean absolute error (MAE), using equations 1.1 – 1.3, where m is the measured value, c is the calculated value, and n is the number of observations. For model calibration, values of C_d were varied for each of the four vegetation zones, several DEMs were tested, and the Manning's coefficient of the mudflat and maximum breaking steepness of waves were varied as well.

$$Relative\ bias\ (RB) = \overline{(c-m)}\Big/_{|\overline{m}|} \quad \text{(Eq. 1.1)}$$

$$Scatter\ index\ (SCI) = \sqrt{\overline{(c-m)^2}}\Big/_{|\overline{m}|} \quad \text{(Eq. 1.2)}$$

$$Mean\ absolute\ error\ (MAE) = \sum|c_i - m_i|\Big/_{n} \quad \text{(Eq. 1.3)}$$

Previous research shows that C_d varies with Reynolds or Keulegan-Carpenter numbers (Mendez and Losada 2004; Pinsky et al. 2013; Foster-Martinez et al. 2018) and that as turbulence increases, C_d decreases. The field campaign carried out by Foster-Martinez et al. (2018) observed a limited range of Reynolds numbers (Re < 600), so we used a constant C_d across all calibration and validation bursts. The C_d was treated as a bulk drag coefficient, or an empirical coefficient appropriate for the whole vegetation field. It was determined by the mean value from the range of observed hydrodynamic conditions and was not time-varying, following the approach of Van Rooijen et al. (2016). Like Van Rooijen et al. (2016), model-data agreement in this study was found to have relatively low sensitivity to small changes in values of C_d. Calibration and validation skill scores are shown in Figure 1.2. See Figure S1.1 for a detailed look at several individual bursts.

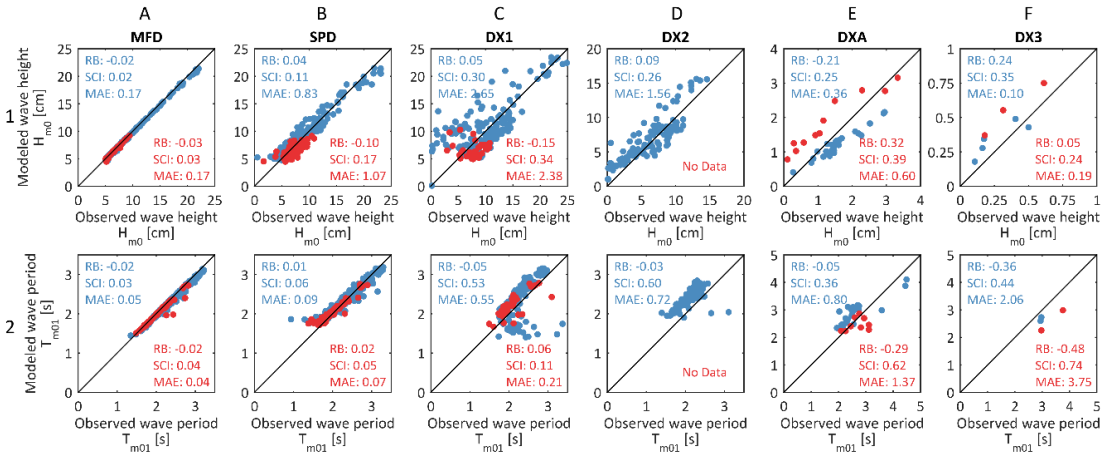

Figure 1.2 Results from model calibration (red) and validation (blue), showing wave height (row 1) and wave period (row 2). Columns A through E show model-data agreement at the six offshore observation locations at China Camp State Park, MFD, SPD, DX1, DX2, DXA, and DX3. Locations of these points can be seen in Figure 1.1. Skill scores correspond to relative bias, scatter, and mean absolute error. No calibration data are shown in column D because data were not collected at DX2 during the calibration period.

Calibration results showed that the model was relatively insensitive to Manning's friction coefficient of the mudflat and the maximum steepness of waves before breaking. Model sensitivity to bathymetry was similar to sensitivity to changes in vegetation drag coefficient ranging up to one standard deviation, or a factor of about two (Table S1-1). Given that maximum steepness and Manning's coefficient are not strong controls on the model and given the uncertainty in the 2 m DEM, the default value for maximum wave steepness was used (0.4), a standard Manning's friction was used for the mudflat (0.018 $s/m^{1/3}$, Chow 1959; Fernandes et al. 2000; Shen et al. 2006) and the vegetation drag coefficients calculated by Foster-Martinez et al. (2018) based on field observations were used.

In many bursts, both observed and modeled wave spectra have a peak at very low frequencies, resulting in both modeled and observed wave periods of up to 400 s. We hypothesize this is due to the length of bursts at which data were collected and the method

of spectral analysis. However, long period infragravity waves (Talke and Stacey 2003) or basin and sub-basin oscillation motions such as seiching (Kimmerer 2004) could also be at play. The focus of this analysis is on local wind waves and therefore these bursts have been excluded. The calibration process also revealed that the model does not simulate propagation of waves less than 1 mm, because XB-NH does not model capillary waves. Thus, bursts in which wave transformation over the transect resulted in peak wave periods greater than 20 s and significant wave heights less than 1 mm were excluded from the plots and skill scores shown in Figure 1.2, which is why there are many more data points at the offshore boundary than on the marsh platform.

The model hindcasts wave height and wave period, establishing that XB-NH effectively models wave transformation in vegetation fields. There is an over-prediction of wave period in the transition zones of the marsh (Figure 1.2, 2C, 2D), and an underprediction of wave period in the high marsh (2F). Wave heights during the calibration and validation phase at DX1 have negative and positive bias, respectively (Figure 1.2, 1F). However, the observed wave heights are small (<4 cm), and thus the biases could be due to changes in the bathymetry between the calibration and validation time periods, which were a month apart.

1.2.4 Schematized model setup

Having established that XBeach, a process-based model, is able to hindcast wave transformation in vegetation, we changed physical parameters in the model to explore the full range of possibilities that have been observed and modeled in our study region and similar study regions, including variations in vegetation, marsh morphology, and hydrodynamics, with a goal of creating idealized simulations that are applicable to other

locations in San Francisco Bay as well as other estuaries. The model settings from calibration and validation were used and physical parameters were varied, including C_d, following the approach taken by Quataert et al. (2015), Best et al. (2018), and Harris et al. (2018). Takekawa et al. (2013) performed an extensive regional survey of San Francisco Bay marshes, and observations from this survey (Table 1-2) were used to determine physical parameters of schematized model transects. Multiple vegetation surveys (Table 1-2) were used to determine typical values and ranges for stem height, diameter, density, and values of C_d.

Table 1-2 A summary of marsh parameters observed in a 2013 regional survey done by Takekawa et al. (2013), followed by a summary of vegetation parameters found in existing literature.

Marsh tidal data	**Survey observations (m NAVD88)**
Mean sea level (MSL)	0.99 - 1.21*
Mean high water (MHW)	1.70 - 1.92
Mean higher high water (MHHW)	1.85 - 2.09
Mean marsh elevation	1.4 - 2.1 m **
Marsh vegetation zones	**Survey observations (m relative to MSL)**
Typical mudflat elevation	< +0.2
Typical low marsh elevation	+0.2 - 0.45, mostly Spartina spp
Typical mid marsh elevation	+0.45 – 0.7
Typical high marsh elevation	> +0.7, mostly Salicornia pacifica

* 10 of the 12 surveyed marshes had mean sea levels between 0.99 and 1.07 m NAVD88

** 11 of the 12 surveyed marshes had mean marsh elevations between 1.6 and 2.1 m NAVD88

Species	Stem density (stems/m²)	Stem diameter (m)	Vegetation height (m)	Cd	Location	Citation
Salicornia pacifica	44000	0.002 - 0.0034	0.22 - 0.25	0.41 - 0.93	SF Bay	Foster-Martinez et al. 2018
Spartina foliosa	312-440	0.0027 - 0.0047	0.16 - 0.48	0.34	SF Bay	Foster-Martinez et al. 2018
Various marsh species	500 (model)	0.007 (model)	1.5 (model)	0.01 - 10 (mean=2.6)	various	Pinsky et al. 2013
Spartina alterniflora and *Spartina patens*	100-500	0.007	1.5		North Carolina	Gittman et al. 2014
Spartina foliosa	284		0.94		Tijuana	Ward et al. 2003

			Estuary	
Spartina foliosa	270		Tijuana Estuary	Desmond et al. 1999
Salicornia pacifica		0.15 - 0.35	SF Bay	Woo and Takekawa 2012
Salicornia europaea	1200 - 10000	0.05 - 0.2	Rhode Island	Ellison 1987

Schematized transects included, from bay to marsh, a sloped mudflat, a sloped marsh edge, a flat marsh top, and an unvegetated levee. The levee was included to ensure there is no flow out the back of the transect, with a slope of 1/10 and a height of +10 m NAVD88. The seaward boundary of each transect had a depth of -5 m NAVD88, thus resulting in ~500 – 2500 m of mudflat leading up to the vegetated marsh, depending on the mudflat slope. The transitions between the first three zones were smoothed with a spline interpolation. Mean sea level (MSL) was set at 1 m (NAVD88), and mean higher high water (MHHW) was set at 1.85 m (NAVD88) (Takekawa et al. 2013). The low marsh vegetation zone was set between +0.2 and +0.45 m MSL, the transition zone was set between elevations of +0.45 and +0.7 m MSL, and the high marsh was set above +0.7 m MSL (Takekawa et al. 2013). Regional surveys show that *S. pacifica* is dominant in the high marsh, and *S. foliosa* is dominant in the low marsh, and that these two species are dominant and nearly equally abundant in the transition zone (Takekawa et al. 2013). Foster-Martinez et al. (2018) also showed that drag coefficients are strongly dependent on the vegetation survey methods; thus, in the schematized models we used a range of vegetation density and frictional values centered on those measured (stem diameter, stem height and stem density, for which we picked values in the middle of the ranges reported) and calculated (C_d, which we rounded to one significant

figure, as shown in Table 1-3) by Foster-Martinez et al. (2018). These vegetation parameters are consistent with studies of similar vegetation from other regions.

A 30-year hindcast by O'Neill et al. (2017) suggested that the largest waves formed (99.9th percentile; i.e., exceeded 9 hours per year) in San Francisco Bay during the time period 1975 and 2004 reached significant wave heights of 1.38 to 1.93 m, depending on basin subregion. Similarly, field observations in the shallows of San Pablo Bay showed that significant wave height frequently surpasses 0.5 m in summer months, and can reach up to 0.8 m during winter storms (Lacy and MacVean 2016). These extreme wave heights occur in the main channels of the bay, where water depth is greatest, but can propagate toward marshes in the bay shallows; the same field observations show that wave height decays by 50% over 6.5 kilometers of mudflat. A 70-year water level hindcast by Nederhoff et al. (2021) suggested that storm-driven water levels in San Francisco Bay can exceed 1.2 m above predicted tides. Beyond high water levels driven by storm conditions, sea level rise is predicted to cause relative elevation of marshes to decrease by between 0.4 and 1.3 m in San Francisco Bay by the end of the century under a moderate emissions scenario (Swanson et al. 2014). Thus, by the end of the century, San Francisco Bay marshes could be exposed to up to 2.5 m of additional water level during storms. Higher water levels in estuaries will increase depth and fetch, enabling larger waves to form (Lacy and MacVean 2016; Karimpour et al. 2017). For example, previous research suggested that one meter of sea level rise in San Francisco Bay will result in up to 0.4 m greater wave heights during a 100 year storm (O'Neill et al. 2017), though this depends on bay sedimentation rates (Ranasinghe et al. 2013). To account for daily and storm wave conditions in San Francisco Bay, as well as estuaries with greater fetch,

we simulated wave heights ranging from typical present day conditions (Lacy and MacVean 2016) to 1.5 – 2 × present day modeled extreme San Francisco Bay wave height (O'Neill et al. 2017). Thus, in some simulations, waves are already breaking by the time they reach the marsh, resulting in greater dissipation over the mudflat as compared to dissipation over vegetation. Experimental models were forced with a JONSWAP spectrum (Hasselmann et al. 1973). To account for storm water levels as well as higher water levels due to rising sea levels, water levels from present day MHHW (1.85 m NAVD88) to 3.15 m above present day MHHW (5 m NAVD88) were used as boundary conditions. Existing marshes tend to have marsh platform with elevations within 20 cm of MHHW, thus this study simulates marshes with 0.05 to 3.2 m of inundation. See Table 1-3 for more information on experimental simulation boundary conditions.

Previous studies with explicit vegetation representation show that C_d can vary widely between sites and under different hydrodynamic conditions (Pinsky et al. 2013; Foster-Martinez et al. 2018). Pinsky et al. (2013) found that drag coefficients ranged from 0.5 to 30 for similar hydrodynamic conditions, illustrating that C_d is a highly variable and uncertain parameter. Numerous studies quantify relationships between C_d and Re in marsh vegetation, but these relationships vary widely and do not extend beyond $Re > 10^3$. Because established relationships between Re and C_d do not extend beyond $Re > 10^3$, in higher Re simulations C_d values are an approximation. To account for this uncertainty in C_d, as well as variations in vegetation density and stem diameter, which also have direct effects on energy attenuation formulation developed by Mendez and Losada (2004), in this study we used a three order of

magnitude range of drag coefficients, centered on the average of the four-week study period in China Camp, which spanned a variety of tidal and wave conditions.

Table 1-3 and Figure 1.3 illustrate the schematized model settings that were used. In the first round of simulations, for each variation in schematized model settings shown in Table 1-3 (base case values are bolded in column 2 of Table 1-3), a range of water levels and frictional coefficients were used (shown by asterisks in column 1 of Table 1-3) to create a suite of multi-dimensional model runs and investigate how each parameter impacts the ability of marshes to transform waves and reduce potential flooding. Each model was run with vegetation present and with vegetation completely removed, to separate the influence of vegetation and the influence of bathymetry. In the unvegetated models, the Manning's friction coefficient determined from calibration and used on the mudflat was applied across the entire transect. This process consisted of 1650 XB-NH simulations. Results can be seen in Section 1.3.2 and were utilized to identify parameters most important in controlling wave transformation.

Table 1-3 A summary of vegetation parameters used in the schematized experimental model runs, followed by a summary of the range of parameters that were varied in the schematized experimental runs. In the bottom half of the table, an asterisk denotes variables that were covaried in all simulations.

Marsh Zone	Stems/m^2	Stem height [cm]	Stem diameter [mm]	C_d
Low	400	15	3	0.3
Transition	20,200	20	2.5	0.6
High	40,000	25	2	0.9

Parameter	Range	Source
*Water level**	[1.85, 2.5, 3, 4, 5] m NAVD88	Nederhoff et al. 2021
Wave height	[0.5, **1**, 1.5, 2, 3] m	ONeill et al. 2017

Wave steepness	[0.025, 0.035, **0.04**, 0.045, 0.055]	Zhao and Li 2019
Vegetation density	[0, 0.5, **1**, 1.5, 2] × values listed above	Foster-Martinez et al. 2018
*C_d, Frictional drag coefficient of vegetation**	[0.1, 0.5, 1, 2, 10] × values listed above	Foster-Martinez et al. 2018, Pinsky et al. 2013
Minimum elevation of vegetation	[0, +10, **+20**, +30 +40] cm relative to MSL	Takekawa et al. 2013
Mudflat slope	[1:100, 1:200, **1:300**, 1:400 1:500]	Danielson et al. 2016
Low marsh slope	[1:10, 1:20, **1:30**, 1:40, 1:50]	Danielson et al. 2016
Marsh platform elevation	[-25, -15, **-5**, +5, +15] cm relative to MHHW	Takekawa et al. 2013
Marsh platform width	[50, 100, 250, 500, 750, **1000**] m	Danielson et al. 2016

Based on results from the first round of simulations, a second round of simulations was subsequently run. In the second round of simulations, the key parameters identified in the first round of simulations (italicized in column 1 of Figure 1.3) were all covaried, creating a complete set of every combination of the key drivers of wave transformation in the ranges identified in Table 1-3 and Figure 1.3, both with vegetation present and with vegetation removed from the transect. This process consisted of 3750 XB-NH simulations and results can be seen in Section 1.3.3.

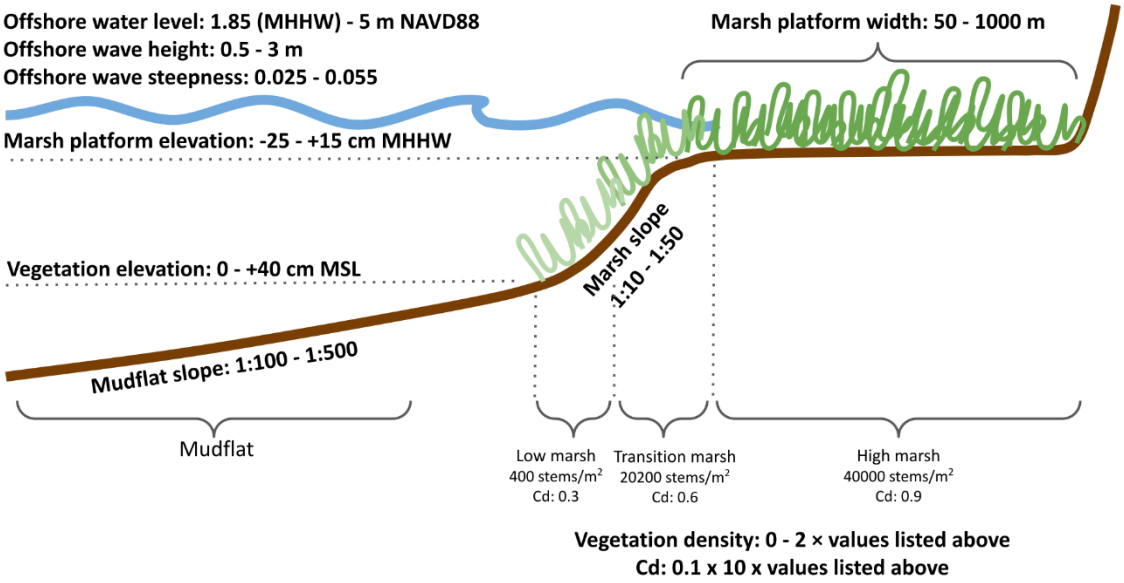

Figure 1.3 Depiction of the schematized transect. Bolded text identifies variables that were changed in the schematized model runs.

All runs were at least 1000 waves long (based on peak period) plus 60 minutes of spin-up (400 – 1500 waves, depending on period) to reach stationarity of the wave setup, which were not used for analysis. Model results were post-processed to obtain significant wave height 100 m into the high marsh (Hs), average wave-induced setup 100 m into the high marsh (setup), and the 98th percentile runup value (R2%). Hs was calculated spectrally using functions available on Open Earth Tools, which is a repository for free and open-source code for a variety of topics related to delta and coastal areas (https://publicwiki.deltares.nl/display/OET/OpenEarth); setup was calculated as the mean water level 100 m into the marsh relative to the offshore water level (i.e., at the offshore edge of the transect, which is between 500 and 2500 m offshore from the marsh edge, depending on mudflat slope); runup was also calculated relative to the offshore water level. Thus, runup is determined by the total water level at the last wet grid cell (TWL) minus the

still water level at the offshore boundary (SWL) and includes both swash and setup. In the shortest marsh settings (50 m of vegetation), Hs and setup were measured at the last vegetated grid cell.

1.3 Results

1.3.1 Wave transformation due to vegetation

To examine and isolate the impact of vegetation on wave transformation, spectral analyses of the incoming water level and subsequent computed wave energy and height from the schematized experimental model runs were completed; an example of this is shown in Figure 1.4. Results show that a large proportion of wave decay due to vegetation happens across a short horizontal distance, with the majority of wave energy dissipation due to vegetation occurring in as little as 50 meters into the marsh vegetation (1D), which is approximately 30 m into the high marsh. This decay in wave height (row 2) and wave energy (1D and 1E) is due to reflection of wave energy by vegetation, which is shown by the peak in the outgoing wave height at that point on the transect (row 3), and to frictional drag. Additionally, wave spectral energy analysis reveals that vegetation reduces relatively higher frequency energy first, and as waves travel up the transect through the marsh vegetation, spectral energy shifts toward lower frequencies (1D, 1E and 1F).

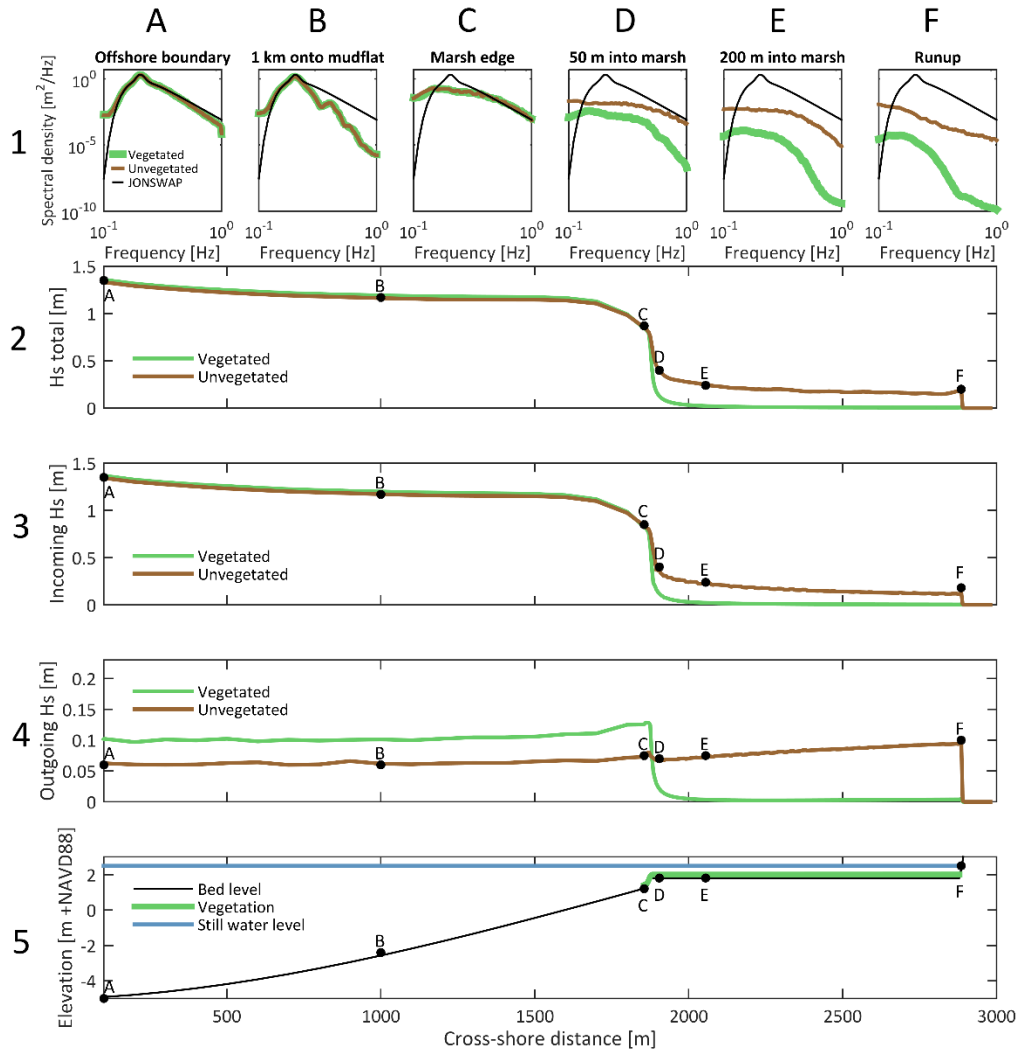

Figure 1.4 The effects of vegetation on spectral density of wave energy and on wave height. Green lines show model results from a transect with a vegetated marsh and brown lines show results from a transect with an unvegetated marsh. Row 1 row shows, from left to right, spectral density at the offshore boundary (1A), 1 km onto the mudflat (1B), at the edge of the marsh (+1.2 m NAVD88, 1C), 50 m into the marsh (1D), 200 m into the marsh (1E), and of the runup signal (1F), with the y-axis plotted in log scale. Black lines in row 1 indicate idealized JONSWAP spectra determined by wave statistics used at the offshore boundary, which diverge from model results at low frequencies due to wave-wave interactions. The middle three rows show, from top to bottom, total significant wave height (row 2), incoming wave height (row 3), and outgoing, or reflected, wave height (row 4). The bottom row (row 5) shows transect bathymetry in black, vegetation location in green, and mean water level in blue. Bathymetry and water level are identical for the vegetated and unvegetated model. Black labeled dots on the bottom four plots show locations of the spectra in the top row (runup location is variable and thus approximate). Models were forced with wave heights of 1.5 m and steepness of 0.04 (peak period

of 4.9 s), and water level was 2.5 m NAVD88 (or 0.65 m of marsh inundation). Drag coefficient (C_d) was 10% of China Camp observations.

1.3.2 Effects of marsh and hydrodynamic settings

The capacity of a marsh to reduce potential flooding increases with increasing vegetation density, C_d, and wave steepness and decreases with increasing minimum elevation of vegetation, water level, and wave height (Figure 1.5 - Figure 1.7). Generally, there are many positive outliers, which signify that when high water levels and low friction coefficients coincide, the potential of marshes to reduce waves and flooding decreases. Marsh width, vegetation friction, water level, and wave height conditions are the strongest controls on wave transformation.

1.3.2.1 Hydrodynamic conditions

Increasing water level (Figure 1.5, column A) results in an increase in Hs and runup. At higher water levels, bathymetric effects are reduced, mudflat friction decreases per the Manning friction formulation, and the relative height of vegetation decreases, thus reducing frictional drag by marsh plants. Increasing the steepness of offshore waves (column B) decreases the wave period, thus decreasing the wave power. This causes a decrease in Hs, setup and runup. In the range of conditions studied here, wave height has a stronger effect on wave transformation metrics than wave steepness. Increasing wave height (column C) causes an increase in Hs, setup and runup as expected based on prior work (Guza and Thornton 1981; 1982; Stockdon et al. 2006).

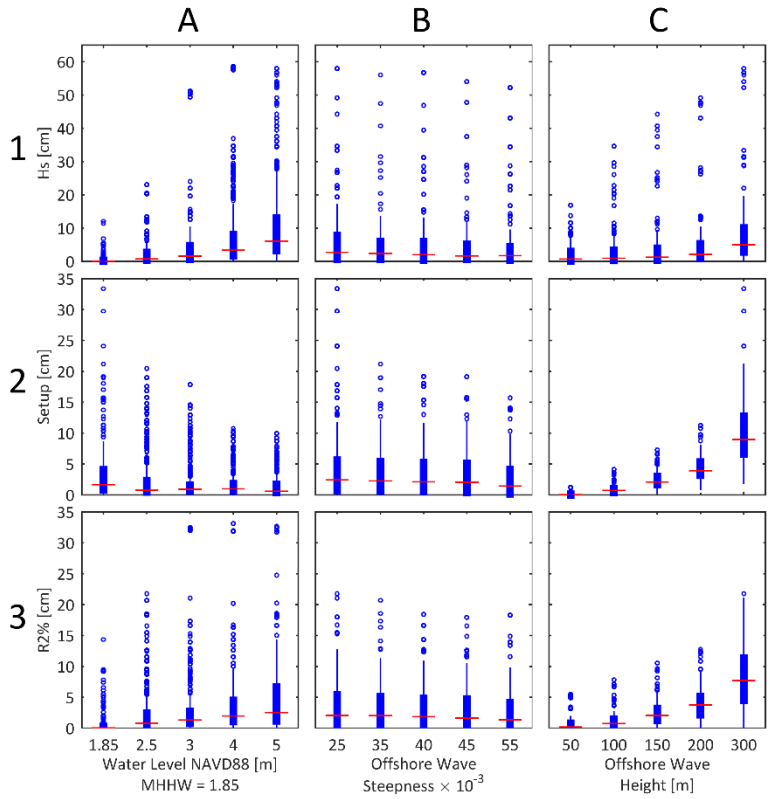

Figure 1.5 Box plots showing changes in wave transformation across the marsh. Wave transformation metrics are on the y axis of all box plots, including: wave height 100 m into the high marsh (Hs, row 1), wave induced setup 100 m into the high marsh (row 2), and R2% (row 3). Characteristics of hydrodynamic conditions are on the x axis of all box plots, including water level (column A), offshore wave steepness (column B), offshore wave height (column C), with each box representing results from all simulations in which the specified hydrodynamic condition has the same setting. Red lines indicate medians, blue rectangles indicate the interquartile range, and blue dots indicate outliers. There are many positive outliers that are caused by coincidence of high water levels and low drag coefficient (C_d). Water level and wave height are the strongest controls on wave transformation.

1.3.2.2 Vegetation characteristics

Increasing vegetation density (Figure 1.6, column A) and increasing C_d (column B) cause similar impacts on wave transformation and flood reduction, resulting in decreased Hs, setup, and runup by increasing the short-wave dissipation due to vegetation. Increasing the minimum elevation of vegetation (column C) causes a greater proportion of the transect to be unvegetated, resulting in waves traveling over more mudflat and a narrower vegetation

field. Thus, increasing the vegetation elevation decreases dissipation due to vegetation. This causes an increase in Hs, setup, and runup. The highest setting of vegetation elevation eliminates the high marsh zone completely, meaning that only low and transition marsh zones are present. This setting results in the greatest change of the wave reduction metrics suggesting that minimum elevation of vegetation has little impact on wave transformation until the high marsh zone is completely lost.

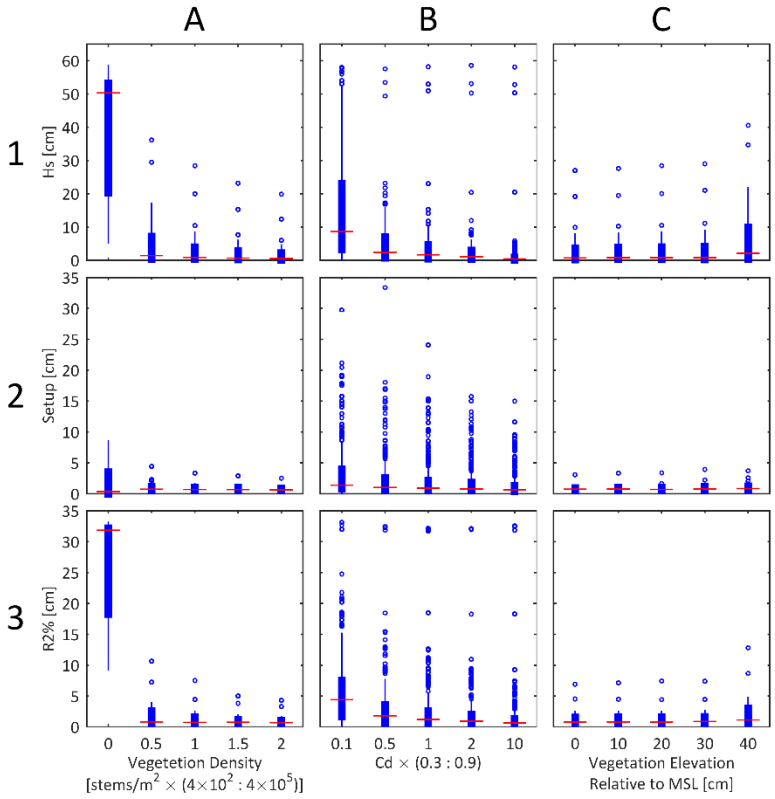

Figure 1.6 Box plots showing changes in wave transformation across the marsh. Wave transformation metrics are on the y axis of all box plots, including: wave height 100 m into the high marsh (Hs, row 1), wave induced setup 100 m into the high marsh (row 2), R2% (row 3). Characteristics of vegetation are on the x axis of all box plots, including vegetation density (column A), vegetation frictional drag coefficient (C_d, column B), and minimum vegetation elevation (column C), with each box representing results from all simulations in which the specified vegetation condition has the same setting. Red lines indicate medians, blue rectangles indicate the interquartile range, and blue dots indicate outliers. There are many positive outliers that are caused by coincidence of high water levels and low C_d. Vegetation density and C_d are the strongest controls on wave transformation.

1.3.2.3 Marsh morphology

The marsh morphology settings include marsh platform elevation, low marsh slope, mudflat slope, and marsh platform width. These settings had the weakest influence on wave transformation with marsh platform width providing the greatest variation, particularly in runup. Increasing the marsh platform width (Figure 1.7, column D) decreases runup because waves must travel across more vegetation before hitting the levee and causing runup. Thus, waves are dissipated more as they travel across the marsh platform in wider marshes, causing less runup at the levee.

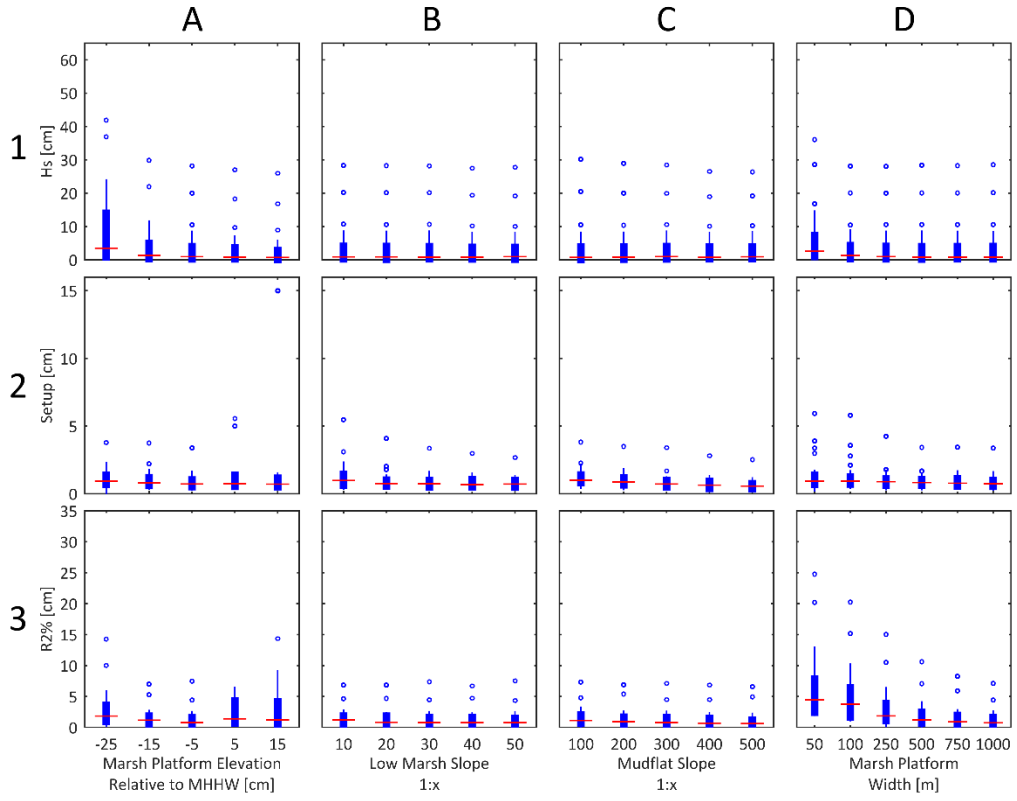

Figure 1.7 Box plots showing changes in wave transformation across the marsh. Wave transformation metrics are on the y axis of all box plots, including: wave height 100 m into the high marsh (Hs, row 1),

wave induced setup 100 m into the high marsh (row 2), and R2% (row 3). Characteristics of marsh morphology are on the x axis of all box plots, including marsh platform elevation (column A), low mash slope (column B), mudflat slope (column C), and marsh platform width (column D), with each box representing results from all simulations in which the specified morphology condition has the same setting. In the shortest marsh setting, Hs and setup were measured at the last vegetated grid cell. Red lines indicate medians, blue rectangles indicate the interquartile range, and blue dots indicate outliers. There are many positive outliers that are caused by coincidence of high water levels and low drag coefficient (C_d). Marsh width is the strongest control on wave transformation.

1.3.3 Key drivers of wave transformation

The cumulative sum of the difference in medians of Hs, setup, and runup across the range of model settings was calculated (Figure 1.8). For example, the top bar shows the difference in median Hs (blue), setup (orange), and runup (red) between the highest and lowest offshore Hs simulated. Variables which produced a cumulative sum of greater than 5 cm were identified as the most important factors that influence the impact of marshes on wave transformation. These include Hs, C_d, water level, and marsh width.

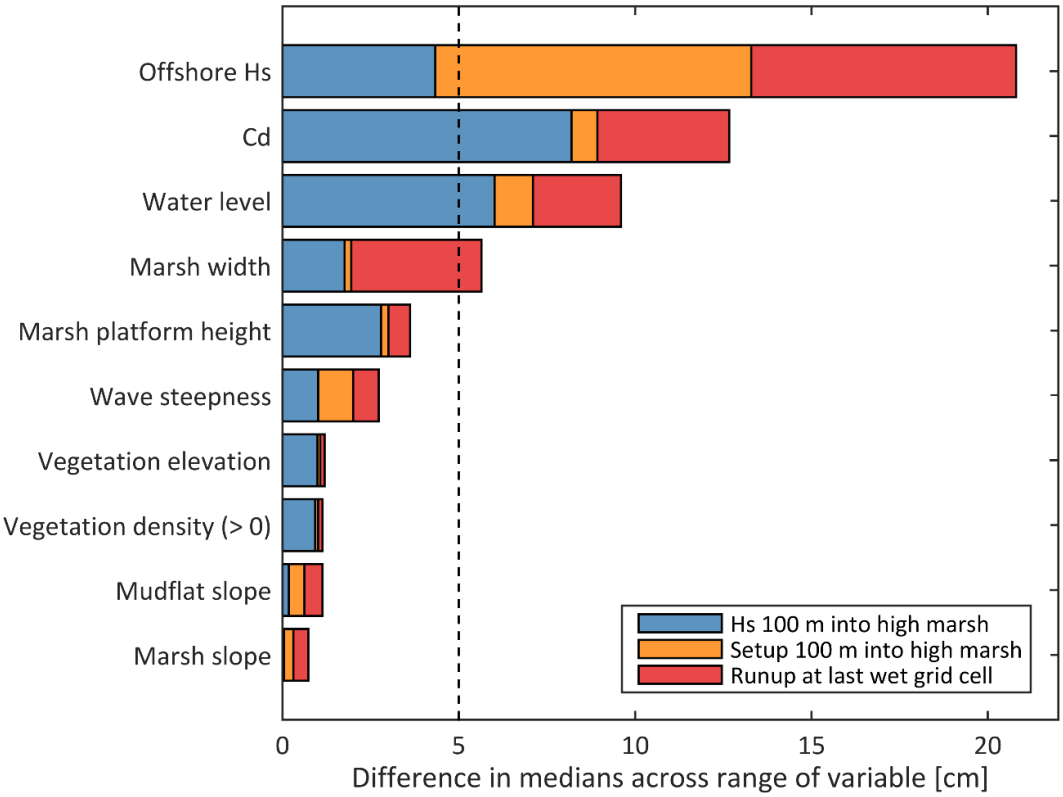

Figure 1.8 The cumulative sum of the difference in medians of Hs, setup, and swash across the range of model settings used in 1.3.2. Variables which produced a cumulative sum greater than 5 cm, shown by the dashed line, were selected to be used in a subsequent analysis.

We ran a subsequent set of simulations using the same settings described in Table 1-3 in which five different factors were covaried (wave height, water level, C_d, marsh width, and wave steepness) to identify combinations of settings that resulted in extreme results, and to further explore the key drivers of wave transformation in marsh ecosystems. Wave steepness was included to provide a more complex look at wave and vegetation dynamics and to allow for multiple settings for each run. All runs were done with and without vegetation present. An overview of results from the second round of simulations is shown in Figure 1.9.

Across the range of conditions explored here, which represent 5^5 simulations with settings described by italicized entries in Table 1-3, vegetation reduces significant wave height 100 m

into the marsh by a median of 35 cm (Figure 1.9, 1B) and 94% (1C). The middle 95% of significant wave height reduction due to vegetation (cm) falls in the range [1, 157]. Vegetation reduces setup by a median of less than 1 cm (2B). The middle 95% of setup reduction due to vegetation (cm) is falls in the range [-5, 17]. Vegetation reduces runup by a median of 40 cm (3B) and 90% (3C). The middle 95% of runup reduction due to vegetation (cm) falls in the range [4, 133].

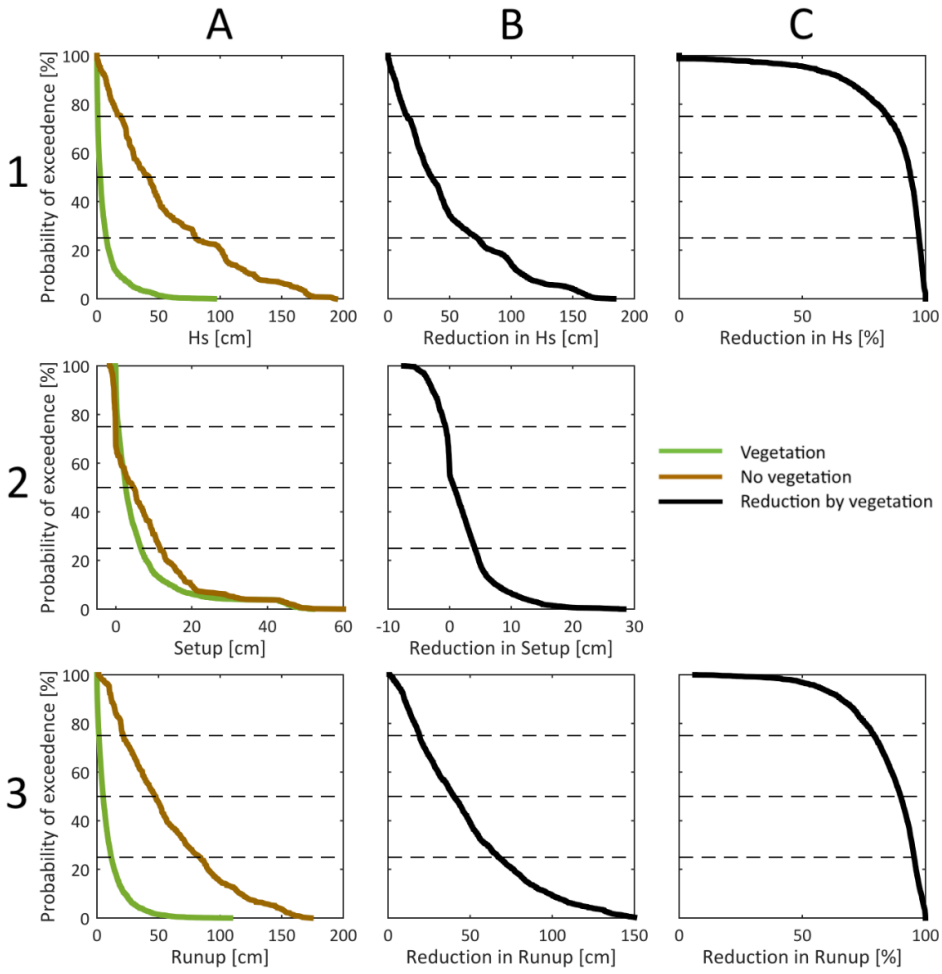

Figure 1.9 An overview of results from the second round of simulations (n = 55) in which wave height, wave steepness, water level, drag coefficient (C_d), and marsh width were all covaried across the ranges

identified in Table 1-3, and in which simulations were completed with and without vegetation. In column A, an empirical cumulative density function of significant wave height 100 m into the high marsh (Hs, row 1), setup 100 m into the high marsh (row 2), and runup at the last wet grid cell (row 3) with vegetation present (green) and vegetation removed (brown) from the transect. In column B and C, reduction in wave height 100 m into the high marsh (Hs, row 1), setup 100 m into the high marsh (row 2), and runup at the last wet grid cell (row 3) between vegetated and unvegetated transects, with absolute reduction in B, and percent reduction in C. Dotted lines show the 25th, 50th, and 75th percentiles. Across the range of settings explored here, vegetation reduces significant wave height 100 m into the marsh by a median of 35 cm (1B); vegetation reduces setup by a median of less than 1 cm (2B); and vegetation reduces runup by a median of 40 cm (3B).

1.3.3.1 Wave height

The presence of vegetation plays a key role in reducing significant wave height in the marsh (Hs), shown by the empirical cumulative density plots in Figure 1.10. When $C_d = 0$ (representing no vegetation), Hs increases for all model settings (1D). The widest spread in Hs reduction due to vegetation occurs with changes in wave height and water level (2B and 2C), meaning that vegetation is reducing Hs effectively across the range of water level and wave settings. Greatest values for Hs and Hs reduction by vegetation occur in simulations with largest waves (1B, 2B) and highest water levels (1C, 2C). Hs is highest with low C_d values (1D), and Hs reduction by vegetation is highest with high C_d values (2D). Wave steepness has limited effect wave height; marsh width also has limited effect because Hs is measured 100 m into the marsh, or at the last vegetated grid cell. Results show that vegetation reduces Hs by a median of 30 cm, and up to 118 cm even with the lowest friction coefficients (2D).

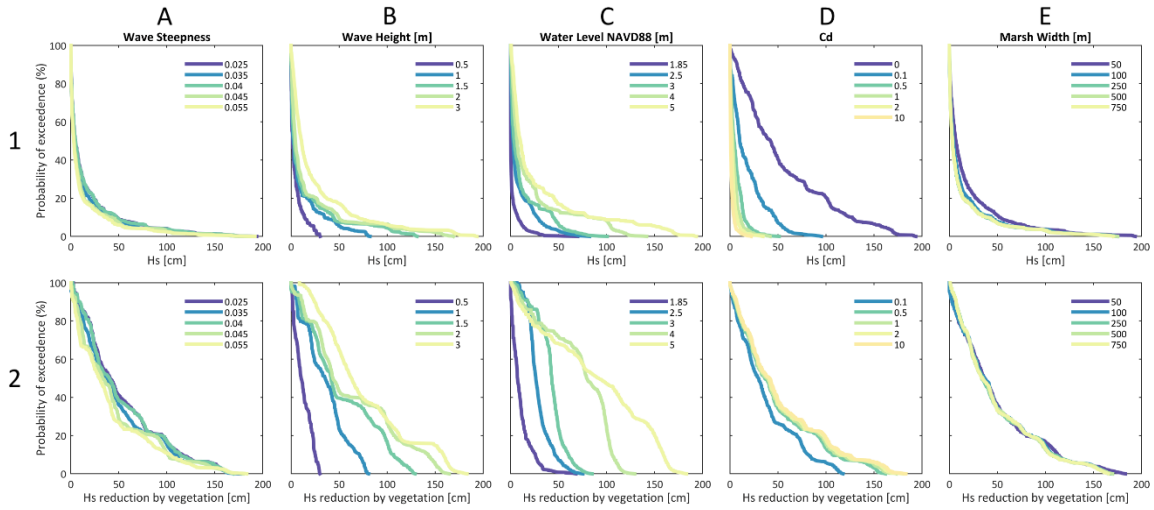

Figure 1.10 In row 1, empirical cumulative density functions showing significant wave height 100 m into the high marsh; and in row 2, empirical density functions showing wave height reduction due to vegetation. Plots are separated from left to right by wave steepness (column A), wave height [m] (column B), water level [m NAVD88] (column C), drag coefficient (C_d) of vegetation (column D), and marsh width [m] (column E), with each single line on each subplot showing an empirical cumulative density function of the mean Hs values from 5^4 simulations. Results show that the presence of vegetation plays a key role in reducing wave height across the range of simulation settings.

1.3.3.2 Setup

Vegetation influences setup through several mechanisms including radiation stress gradients (Buckley et al. 2016), wave-induced force due to emergent vegetation (Dean and Bender 2006), and wave-induced force due to skewed waves (Dean and Bender 2006), which each decrease setup; vegetation can also increase setup due to an increase in the mean drag force (Løvås and Tørum 2001; Luhar et al. 2010). As a result, the influence of vegetation on setup is nuanced, as shown by the empirical cumulative density plots in Figure 1.11. Extreme values for setup and setup reduction by vegetation occur in simulations wth largest waves (1B, 2B) and lowest water levels (1C, 2C). Narrow marshes (1E), no vegetation (1D), and the least steep waves (1A) result in highest values of setup. Setup reduction due to vegetation is greatest across wider marshes (2E) with higher C_d (2D); wave steepness has limited effect.

The widest spread in setup reduction due to vegetation occurs with changes in water level. At lower water level settings, vegetation can reduce setup by more than 25 cm, while at higher water level settings, vegetation can increase setup by more than 5 cm (2C), likely due to large mean drag forces acting to increase setup in these settings (Løvås and Tørum 2001; Luhar et al. 2010). Wave height also plays an important role, with vegetation resulting in the most significant increases and decreases in setup under the largest wave settings (2B).

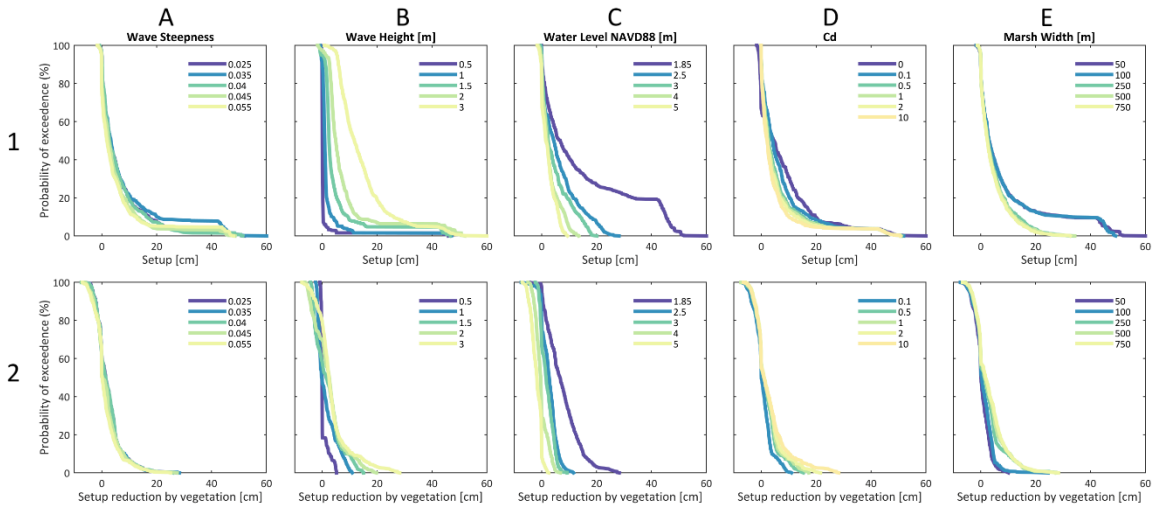

Figure 1.11 In row 1, empirical cumulative density functions showing setup 100 m into the high marsh; and in row 2, empirical density functions showing setup reduction due to vegetation. Plots are separated from left to right by wave steepness (column A), wave height [m] (column B), water level [m NAVD88] (column C), drag coefficient (C_d) of vegetation (column D), and marsh width [m] (column E), with each single line on each subplot showing an empirical cumulative density function of the mean setup values from 5^4 simulations. Results show that the presence of vegetation plays a key role in influencing setup, particularly in low water level and in large wave settings.

1.3.3.3 Runup

Results show that the presence of vegetation plays a key role in reducing runup (setup + swash) across the range of simulation settings, shown by the empirical cumulative density plots in Figure 1.12. Extreme values for runup and runup reduction by vegetation occur in simulations with largest waves (1B, 2B) and highest water levels (1C, 2C). Runup is highest

with low C_d (1D) and runup reduction is highest with high C_d (2D). Runup is greatest across narrow mashes (1E), but vegetation reduces runup effectively even in the narrowest marshes (2E). Wave steepness has limited effect on runup and runup reduction due to vegetation. Results show that vegetation reduces runup by a median of 45 cm in the narrowest marshes (dark purple line in 2E) and by a median of 30 cm with the lowest friction coefficients (blue line in 2D). In both settings, vegetation can reduce runup by more than 130 cm.

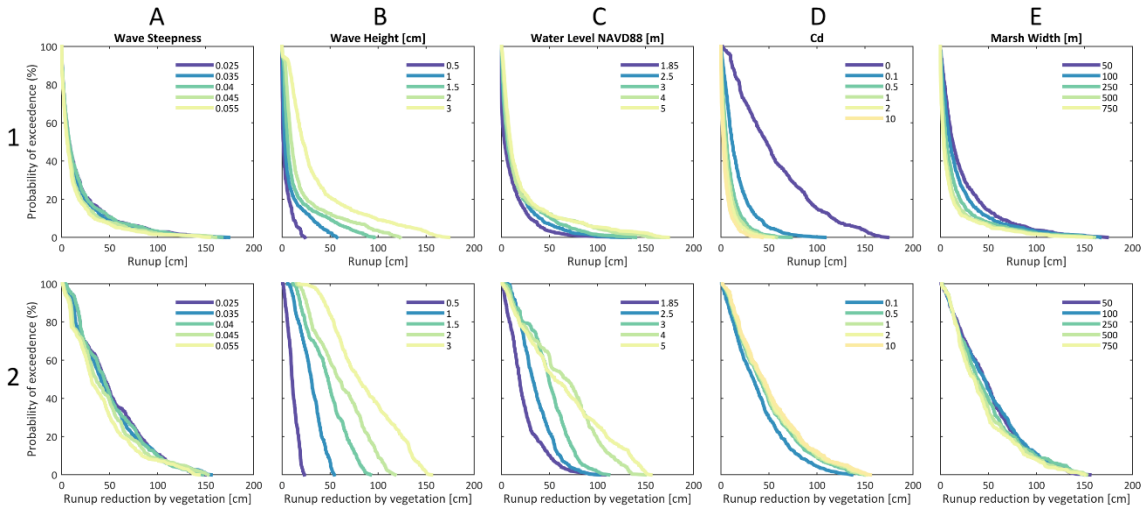

Figure 1.12 In row 1, empirical cumulative density functions showing runup at the last wet grid cell; and in row 2, empirical density functions showing runup reduction due to vegetation. Plots are separated from left to right by wave steepness (column A), wave height [m] (column B), water level [m NAVD88] (column C), drag coefficient (C_d) of vegetation (column D), and marsh width [m] (column E) with each single line on each subplot showing an empirical cumulative density function of the mean runup values from 5^4 simulations. Results show that the presence of vegetation plays a key role in

1.3.4 Extreme Events

In many locations in San Francisco Bay, marsh width is constrained between open water and levees. To understand the interplay between vegetation, marsh width, and extreme storm conditions, we explored the effects of marsh vegetation and marsh width in conditions representative of a present-day strong storm with wave heights of 1.5 m (O'Neill et al. 2017)

and water level 1.15 m above MHHW (Nederhoff et al. 2021), or 3 m NAVD88, with wave steepness and C_d varied across the ranges shown in Table 1-3.

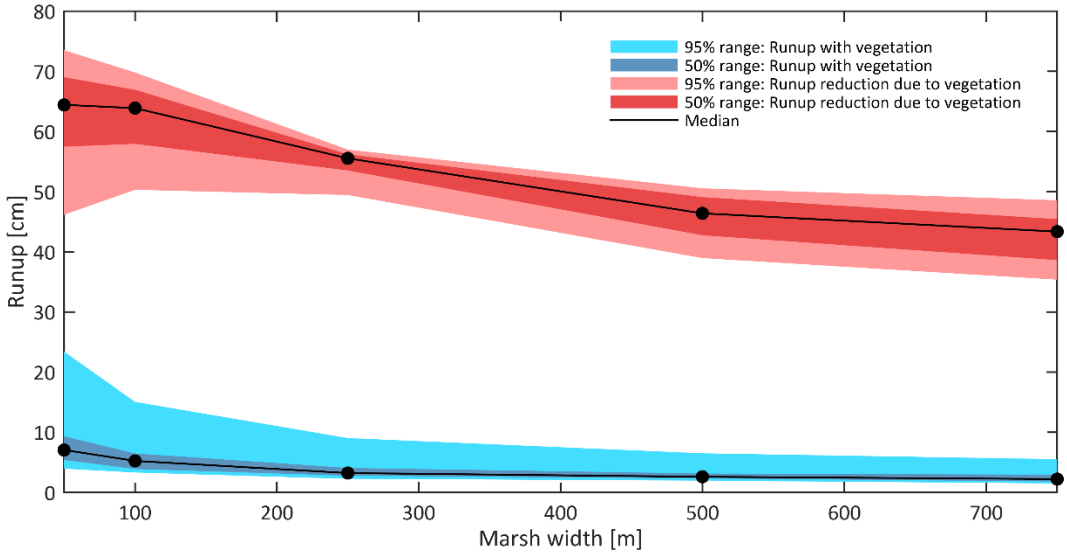

Figure 1.13 Runup across a vegetated marsh (blue) and runup reduction due to vegetation (red) on the y axis, and marsh width on the x axis. Black dots show simulated marsh widths. Conditions represent an extreme storm in San Francisco Bay (wave height of 1.5 m and water level 1.15 m above MHHW).

Results show that even in the narrowest marshes simulated (50 m), runup (setup + swash) is unlikely to exceed 25 cm, and that vegetation can reduce runup by a median of 65 cm across a 50 m marsh in storm conditions (Figure 1.13). As marsh width increases, runup quickly decreases. Beyond 250 meters of marsh width, additional width has limited impact on runup. Vegetation reduces runup most in narrower marsh settings because runup in unvegetated transects is greatest in narrower settings.

In the same hydrodynamic conditions representative of an extreme storm, across the range of marsh widths, C_d values, and wave steepness settings explored in this work, the main role vegetation plays in reducing nearshore water levels is through reducing swash. Vegetation

reduces water levels at the base of the levee by a median of 55 cm primarily through reduction in swash (Figure 1.14).

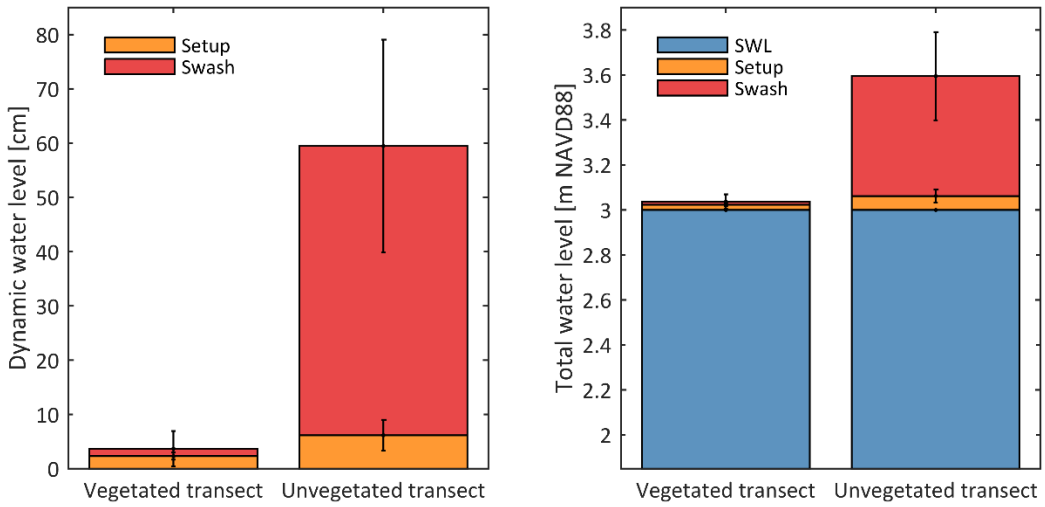

Figure 1.14 Bar graphs showing components of the dynamic water level (left) and the total water level (right), with and without vegetation. Components of the dynamic water level include setup (measured 100 m into the marsh or at the last vegetated grid cell) and swash (measured at the last wet grid cell), and components of the total water level include the still water level (SWL), setup, and swash. The total water level y axis starts at the MHHW level. Bars represent median values and error bars show the middle 50% of values for setup and swash. Vegetation reduces the dynamic water level by a median of 55 cm in conditions representative of a present-day extreme storm (wave heights of 1.5 m and water level 1.15 m above MHHW), across a range of drag coefficient (C_d), marsh width, and wave steepness values.

1.4. Discussion

Vegetation on marshes can be effective in reducing potential wave induced flooding. In the range of model settings explored here, vegetation on a marsh reduces significant wave height by a median of 35 cm, causes minor changes in wave-induced setup (<5 cm), and reduces runup by a median of 40 cm (Figure 1.9). Meaningful reductions in wave height and runup can be achieved even in the narrowest marshes simulated (50 m, Figure 1.13).

Flood managers can use the information presented here to strategically plan for extreme events. For example, under conditions similar to a 100-year storm in San Francisco Bay, with offshore water level of 1.15 m above MHHW and wave heights of 1.5 m, 50 m of marsh vegetation reduces runup by a median of 65 cm and runup after a 50 m wide marsh will likely be less than 25 cm, reduced from as high as 1 m (Figure 1.13). Under these same conditions, the dynamic water level at the base of the levee without vegetation is a median of 55 cm higher than it is with vegetation (Figure 1.14), increasing likelihood of levee overtopping. High velocities introduced by wave overtopping of levees can introduce turbulence, scouring, and erosion of levees, as modeled by Xiao et al. (2009) and observed during Hurricane Katrina in New Orleans, Louisiana, USA.

The validation presented here shows that the XB-NH model is capable of accurately simulating wave transformation of incident-band waves due to vegetation, allowing a first look at the effects of vegetation on incident-band driven runup. This has been achieved by utilizing a constant bulk drag coefficient (C_d) similar to other authors (van Rooijen et al. 2016) in which vegetation is schematized as a rigid-cylinder concept. Over the past several decades, several authors (Mendez and Losada 2004; Pinsky et al. 2013; Jadhav et al. 2013; Möller et al. 2014; Foster-Martinez et al. 2018) have developed formulas to describe the relationship between C_d and Reynolds number (Re). The trend in these relationships is clear and shows that C_d decreases as conditions become more turbulent, with high Re. However, the specific relation varies widely between vegetation types and even between different studies of the same vegetation species. Pinsky et al. (2013) uniformly re-analyzed existing wave attenuation in marshes from 14 prior studies to determine a generalized relationship between C_d and Re.

However, C_d is inherently difficult to measure, and is typically calculated using other vegetation measurements including stem height, stem density, and stem diameter, which each pose challenges in measurement due to seasonal, site, and species variability. These challenges have spurred recent developments in quantifying wave attenuation in marshes by their standing biomass rather than the parameters listed above (Maza et al. 2022), though this approach is not yet incorporated into numerical models like XBeach. Here, we utilized a constant C_d, determined from field measurements taken by Foster-Martinez et al. (2018) and varied it across three orders of magnitude. While we did not vary C_d as a function of Reynolds number in this study, 77% of hydrodynamic and C_d combinations fell within one standard deviation of the relationship derived by Pinsky et al. (2013), which is specific to marsh habitat; 13% fell below and 10% fell above one standard deviation. This is largely due to the high degree of uncertainty in relationships between C_d and Re, particularly beyond $Re > 10^3$, which is the upper limit of established relationships between Re and C_d. The uncertainty of our experimental simulations increases outside the calibrated range, but similarly to van Rooijen et al. (2016), our results show a relatively low sensitivity to a three order-of-magnitude variation in C_d in comparison to changes in hydrodynamics, as shown by the spread of empirical density curves in column D of Figure 1.10 - Figure 1.12. Further, based on the Pinsky et al. (2013) equation, a three order of magnitude variation in C_d is approximately the range expected for the range of Reynolds numbers simulated here. This is encouraging for applications in which vegetation measurements are limited and the vegetation bulk drag coefficient is unknown. The inverse relationship between C_d and Re results in outliers shown throughout Figure 1.5 - Figure 1.7, which occur with coincidence of high water-levels and low C_d. These simulations give insight to how wave transformation capacity of vegetated marshes

may change in high water level settings due to changes in wave Reynolds number, driven by an increase in orbital velocity. To further explore how marsh plants can reduce wave driven flooding, we recommend prioritizing additional observational studies measuring wave attenuation in marshes, particularly during extreme hydrodynamic conditions, such as strong storms and high tides.

As sea levels rise, marshes may either vertically accrete, retreat landward, erode, or drown; the response of a marsh depends on sediment supply, location, and morphology. This study has parameterized these responses: a marsh accreting vertically gains marsh platform elevation (Figure 1.7, column A); a marsh retreating increases the elevation where vegetation begins (Figure 1.6, column C); a marsh laterally eroding steepens the low marsh slope (Figure 1.7, column B); a marsh that drowns and transitions to mudflat loses vegetation density (Figure 1.6, column A). Results from this study show that flood risk increases most drastically for marshes that lose vegetation density and transition to mudflat (Figure 1.6, column A). In a setting similar to China Camp, transition to mudflat could mean increases of 50 cm in wave height at the marsh interior and increases of 30 cm in vertical wave runup (Figure 1.6, A1, and A3, respectively), emphasizing the importance of maintaining marsh vegetation coverage in urban estuaries. In marshes that are providing important flood reduction services, managers could consider sediment nourishment to facilitate vegetation persistence with rising water level (Ganju 2019).

This work highlights the importance of continuing research on sediment dynamics in marshes and marsh response to higher water levels. Radioisotope dated cores show San Francisco Bay marshes have been keeping up with sea level rise over the last 150 years, with typical vertical

accretion rates of 0.2 – 0.5 cm/year (Callaway et al. 2012). However, studies accounting for future sea level rise rates and current marsh accretion rates show that accretion rates are presently less than 4% of what will be necessary to keep up with accelerating sea level rise by the end of the 21st century (Knowles 2010; Barnard et al. 2013). The relative elevations of marshes in San Francisco Bay are predicted to decrease by 0.4 to 1.3 m by 2100 (Swanson et al. 2014), causing marshes that do not have migration space to transition to mudflats (Elmilady et al. 2019).

Beyond San Francisco Bay, the majority of the world's megacities are coastal, and average global flood losses are expected to rise tenfold between 2005 and 2050, even with adaptation investments to maintain constant flood probability (Hallegatte et al. 2013). Many of these coastal megacities are at least partially protected by marshes, meaning that flood risk will be further amplified beyond SLR if marsh sedimentation rates are outpaced by SLR. Without rigorous sediment nourishment, there may be a tipping point after which relative elevations of marshes have decreased such that marsh habitat is not an effective flood defense. At that point, flood managers interested in nature-based shorelines could instead focus efforts on approaches such as vegetated levees to reduce swash, which still provide wave and flood reduction benefits of vegetation fields but are less sensitive to relative sea level.

References

Barnard, Patrick L., David H. Schoellhamer, Bruce E. Jaffe, and Lester J. McKee. 2013. "Sediment Transport in the San Francisco Bay Coastal System: An Overview." *Marine Geology* 345: 3–17. https://doi.org/10.1016/j.margeo.2013.04.005.

Barnard, Patrick L., Li H. Erikson, Amy C. Foxgrover, Juliette A. Finzi Hart, Patrick Limber, Andrea C. O Neill, Maarten Van Ormondt, et al. 2019. "Dynamic Flood Modeling Essential to Assess the Coastal Impacts of Climate Change." *Nature Scientific Reports* 9.

https://doi.org/10.1038/s41598-019-40742-z.

Best, S. N., M. Van der Wegen, J. Dijkstra, P. W. J. M. Willemsen, B. W. Borsje, and Dano J. A. Roelvink. 2018. "Do Salt Marshes Survive Sea Level Rise? Modelling Wave Action, Morphodynamics and Vegetation Dynamics." *Environmental Modelling and Software* 109 (August): 152–66. https://doi.org/10.1016/j.envsoft.2018.08.004.

Bigalbal, Alayna, Ali M. Rezaie, Juan L. Garzon, and Celso M. Ferreira. 2018. "Potential Impacts of Sea Level Rise and Coarse Scale Marsh Migration on Storm Surge Hydrodynamics and Waves on Coastal Protected Areas in the Chesapeake Bay." *Marine Science and Engineering* 6. https://doi.org/10.3390/jmse6030086.

Bouma, T. J., S. Temmerman, L. A. van Duren, E. Martini, W. Vandenbruwaene, D. P. Callaghan, T. Balke, et al. 2013. "Organism Traits Determine the Strength of Scale-Dependent Bio-Geomorphic Feedbacks: A Flume Study on Three Intertidal Plant Species." *Geomorphology* 180–181: 57–65. https://doi.org/10.1016/j.geomorph.2012.09.005.

Buckley, Mark L., Ryan J. Lowe, Jeff E. Hansen, and Ap R. Van Dongeren. 2016. "Wave Setup over a Fringing Reef with Large Bottom Roughness." *Journal of Physical Oceanography* 46 (8): 2317–33. https://doi.org/10.1175/JPO-D-15-0148.1.

Buffington, KJ, and KM Thorne. 2018. "LEAN-Corrected San Francisco Bay Digital Elevation Model." U.S. Geological Survey.

Callaghan, D. P., T. J. Bouma, P. Klaassen, D. van der Wal, M. J. F. Stive, and P. M. J. Herman. 2010. "Hydrodynamic Forcing on Salt-Marsh Development: Distinguishing the Relative Importance of Waves and Tidal Flows." *Estuarine, Coastal and Shelf Science* 89 (1): 73–88. https://doi.org/10.1016/j.ecss.2010.05.013.

Callaway, John C., Evyan L. Borgnis, R. Eugene Turner, and Charles S. Milan. 2012. "Carbon Sequestration and Sediment Accretion in San Francisco Bay Tidal Wetlands." *Estuaries and Coasts* 35 (5): 1163–81. https://doi.org/10.1007/s12237-012-9508-9.

Chow, Ven Te. 1959. *Open-Channel Hydraulics*. McGraw-Hill Book Company, Inc.

Dalrymple, Robert A., James T. Kirby, and Paul A. Hwang. 1984. "Wave Diffraction Due To Areas of Energy Dissipation." *Journal of Waterway, Port, Coastal and Ocean Engineering* 110 (1): 67–79.

Danielson, Jeffrey J., Sandra K. Poppenga, John C. Brock, Gayla A. Evans, Dean J. Tyler, Dean B. Gesch, Cindy A. Thatcher, and John A. Baras. 2016. "Topobathymetric Elevation Model Development Using a New Methodology : Coastal National Elevation Database." *Journal of Coastal Research*, no. 76. https://doi.org/10.2112/SI76-008.

de Ridder, Menno P., Pieter B. Smit, Ap van Dongeren, Robert McCall, Kees Nederhoff, and Ad J.H.M. Reniers. 2020. "Efficient Two-Layer Non-Hydrostatic Wave Model with Accurate Dispersive Behaviour." *Coastal Engineering* 164 (October 2020): 103808. https://doi.org/10.1016/j.coastaleng.2020.103808.

Dean, Robert G., and Christopher J. Bender. 2006. “Static Wave Setup with Emphasis on Damping Effects by Vegetation and Bottom Friction.” *Coastal Engineering* 53 (2–3): 149–56. https://doi.org/10.1016/j.coastaleng.2005.10.005.

DeConto, Robert M., and David Pollard. 2016. “Contribution of Antarctica to Past and Future Sea-Level Rise.” *Nature* 531 (7596): 591–97. https://doi.org/10.1038/nature17145.

Desmond, J., G. Williams, M. James, J. Johnson, J. Callaway, and J. Zedler. 1999. “Tijuana River National Estuarine Research Reserve: Annual Report on Ecosystem Monitoring.” *Pacific Estuarine Research Laboratory, San Diego, California*.

Ellison, A. M. 1987. “Effects of Competition, Disturbance, and Herbivory on Salicornia Europaea.” *Ecology*. https://doi.org/10.2307/1938463.

Elmilady, H., M. van der Wegen, D. Roelvink, and B. E. Jaffe. 2019. “Intertidal Area Disappears Under Sea Level Rise: 250 Years of Morphodynamic Modeling in San Pablo Bay, California.” *Journal of Geophysical Research: Earth Surface* 124 (1): 38–59. https://doi.org/10.1029/2018JF004857.

Fernandes, Elisa Helena, Keith Richard Dyer, and Luis Felipe Hax Niencheski. 2000. “Calibration and Validation of the TELEMAC-2D Model to the Patos Lagoon (Brazil).” *Journal of Coastal Research*, 470–88.

Foster-Martinez, M. R., J. R. Lacy, M. C. Ferner, and E. A. Variano. 2018. “Wave Attenuation across a Tidal Marsh in San Francisco Bay.” *Coastal Engineering* 136 (February): 26–40. https://doi.org/10.1016/j.coastaleng.2018.02.001.

Ganju, Neil K. 2019. “Marshes Are the New Beaches: Integrating Sediment Transport into Restoration Planning.” *Estuaries and Coasts* 42 (4): 917–26. https://doi.org/10.1007/s12237-019-00531-3.

Garzon, Juan L., M. Maza, C. M. Ferreira, J. L. Lara, and I. J. Losada. 2019. “Wave Attenuation by Spartina Saltmarshes in the Chesapeake Bay Under Storm Surge Conditions.” *Journal of Geophysical Research: Oceans* 124 (7): 5220–43. https://doi.org/10.1029/2018JC014865.

Gittman, Rachel K., Alyssa M. Popowich, John F. Bruno, and Charles H. Peterson. 2014. “Marshes with and without Sills Protect Estuarine Shorelines from Erosion Better than Bulkheads during a Category 1 Hurricane.” *Ocean and Coastal Management* 102 (PA): 94–102. https://doi.org/10.1016/j.ocecoaman.2014.09.016.

Guza, R. T., and E. B. Thornton. 1981. “Wave Set-up on a Natural Beach.” *Journal of Geophysical Research* 86 (C5): 4133–37. https://doi.org/10.1029/JC086iC05p04133.

———. 1982. “Swash Oscillations on a Natural Beach.” *Journal of Geophysical Research* 87 (C1): 483–91. https://doi.org/10.1029/JC087iC01p00483.

Guza, R. T., E. B. Thornton, and R. A. Holman. 1984. “Swash on Steep and Shallow Beaches.” *Proceedings of the Nineteenth Int. Conference on Coastal Engineering*, 708–23. https://doi.org/10.9753/icce.v19.48.

Hallegatte, Stephane, Colin Green, Robert J. Nicholls, and Jan Corfee-Morlot. 2013. "Future Flood Losses in Major Coastal Cities." *Nature Climate Change* 3 (9): 802–6. https://doi.org/10.1038/nclimate1979.

Harris, Daniel L., Alessio Rovere, Elisa Casella, Hannah Power, Remy Canavesio, Antoine Collin, Andrew Pomeroy, Jody M. Webster, and Valeriano Parravicini. 2018. "Coral Reef Structural Complexity Provides Important Coastal Protection from Waves under Rising Sea Levels." *Science Advances* 4 (2): 1–8. https://doi.org/10.1126/sciadv.aao4350.

Hasselmann, K. 1974. "On the Spectral Dissipation of Ocean Waves Due to White Capping." *Boundary-Layer Meteorology* 6: 107–27.

Hasselmann, K., T. P. Barnett, E. Bouws, H. Carlson, D. E. Cartwright, K. Enke, J. A. Ewing, et al. 1973. "Measurements of Wind-Wave Growth and Swell Decay during the Joint North Sea Wave Project (JONSWAP)."

Jadhav, Ranjit S., Qin Chen, and Jane M. Smith. 2013. "Spectral Distribution of Wave Energy Dissipation by Salt Marsh Vegetation." *Coastal Engineering* 77: 99–107. https://doi.org/10.1016/j.coastaleng.2013.02.013.

Karimpour, Arash, Qin Chen, and Robert R. Twilley. 2017. "Wind Wave Behavior in Fetch and Depth Limited Estuaries." *Scientific Reports* 7 (December 2016): 1–8. https://doi.org/10.1038/srep40654.

Kimmerer, Wim J. 2004. "Open Water Processes of the San Francisco Estuary: From Physical Forcing to Biological Responses." *San Francisco Estuary and Watershed Science* 2 (1). https://doi.org/10.15447/sfews.2004v2iss1art1.

Kirwan, Matthew L., Glenn R. Guntenspergen, Andrea D'Alpaos, James T. Morris, Simon M. Mudd, and Stijn Temmerman. 2010. "Limits on the Adaptability of Coastal Marshes to Rising Sea Level." *Geophysical Research Letters* 37 (23): 1–5. https://doi.org/10.1029/2010GL045489.

Knowles, Noah. 2010. "Potential Inundation Due to Rising Sea Levels in the San Francisco Bay Region." *San Francisco Estuary and Watershed Science* 8 (1). https://doi.org/10.15447/sfews.2010v8iss1art1.

Lacy, J.R., R.M. Allen, M.R. Foster-Martinez, J.C. Ferreira, and A. C. O'Neill. Hydrodynamic and sediment transport data from San Pablo Bay and China Camp marsh (northern San Francisco Bay). 2017. "Hydrodynamic and Sediment Transport Data from San Pablo Bay and China Camp Marsh (Northern San Francisco Bay), 2013-2016." https://doi.org/10.5066/F7HM56MX.

Lacy, Jessica R., and Lissa J. MacVean. 2016. "Wave Attenuation in the Shallows of San Francisco Bay." *Coastal Engineering* 114: 159–68. https://doi.org/10.1016/j.coastaleng.2016.03.008.

Le Bars, Dewi, Sybren Drijfhout, and Hylke De Vries. 2017. "A High-End Sea Level Rise Probabilistic Projection Including Rapid Antarctic Ice Sheet Mass Loss." *Environmental Research Letters* 12 (4). https://doi.org/10.1088/1748-9326/aa6512.

Longuet-Higgins, M. S., and R. W. Stewart. 1963. “A Note on Wave Set-Up.” *Journal of Marine Research* 11 (2): 324. https://doi.org/10.1016/0011-7471(64)90258-x.

Løvås, Stig Magnar, and Alf Tørum. 2001. “Effect of the Kelp Laminaria Hyperborea upon Sand Dune Erosion and Water Particle Velocities.” *Coastal Engineering* 44 (1): 37–63. https://doi.org/10.1016/S0378-3839(01)00021-7.

Luhar, Mitul, Sylvain Coutu, Eduardo Infantes, Samantha Fox, and Heidi Nepf. 2010. “Wave-Induced Velocities inside a Model Seagrass Bed.” *Journal of Geophysical Research: Oceans* 115 (12): 1–15. https://doi.org/10.1029/2010JC006345.

Ma, Gangfeng, James T. Kirby, Shih Feng Su, Jens Figlus, and Fengyan Shi. 2013. “Numerical Study of Turbulence and Wave Damping Induced by Vegetation Canopies.” *Coastal Engineering* 80: 68–78. https://doi.org/10.1016/j.coastaleng.2013.05.007.

Masson-Delmotte, V., P. Zhai, A. Pirani, S. L. Connors, C. Péan, S. Berger, N. Caud, et al. 2021. “IPCC, 2021: Summary for Policymakers. In: Climate Change 2021: The Physical Science Basis. Contribution of Working Group I to the Sixth Assessment Report of the Intergovernmental Panel on Climate Change.” *Cambridge University Press*.

Maza, M., J. L. Lara, I. J. Losada, B. Ondiviela, J. Trinogga, and T. J. Bouma. 2015. “Large-Scale 3-D Experiments of Wave and Current Interaction with Real Vegetation. Part 2: Experimental Analysis.” *Coastal Engineering* 106: 73–86. https://doi.org/10.1016/j.coastaleng.2015.09.010.

Maza, Maria, Javier L. Lara, and Iñigo J. Losada. 2022. “A Paradigm Shift in the Quantification of Wave Energy Attenuation Due to Saltmarshes Based on Their Standing Biomass.” *Scientific Reports*, 1–13. https://doi.org/10.1038/s41598-022-18143-6.

Mendez, Fernando J., and Inigo J. Losada. 2004. “An Empirical Model to Estimate the Propagation of Random Breaking and Nonbreaking Waves over Vegetation Fields.” *Coastal Engineering* 51 (2): 103–18. https://doi.org/10.1016/j.coastaleng.2003.11.003.

Menéndez, Pelayo, Iñigo J. Losada, Saul Torres-Ortega, Siddharth Narayan, and Michael W. Beck. 2020. “The Global Flood Protection Benefits of Mangroves.” *Scientific Reports* 10 (1): 1–11. https://doi.org/10.1038/s41598-020-61136-6.

Merkens, Jan-ludolf, Lena Reimann, Jochen Hinkel, and Athanasios T. Vafeidis. 2016. “Gridded Population Projections for the Coastal Zone under the Shared Socioeconomic Pathways.” *Global and Planetary Change* 145: 57–66. https://doi.org/10.1016/j.gloplacha.2016.08.009.

Miche, M. 1951. “Le Pouvoir Réfléchissant Des Ouvrages Maritimes Exposés à l’action de La Houle.” *Annales de Ponts et Chaussées* 121: 285–319.

Möller, Iris, Matthias Kudella, Franziska Rupprecht, Tom Spencer, Paul Maike, Bregje K. van Wesenbeeck, Guido Wolters, et al. 2014. “Wave Attenuation over Coastal Salt Marshes under Storm Surge Conditions.” *Nature Geosciences* 7: 727–31.

Narayan, Siddharth, Michael W. Beck, Borja G. Reguero, Iñigo J. Losada, Bregje Van

Wesenbeeck, Nigel Pontee, James N. Sanchirico, Jane Carter Ingram, Glenn Marie Lange, and Kelly A. Burks-Copes. 2016. “The Effectiveness, Costs and Coastal Protection Benefits of Natural and Nature-Based Defences.” *PLoS ONE* 11 (5): 1–17. https://doi.org/10.1371/journal.pone.0154735.

Narayan, Siddharth, Michael W. Beck, Paul Wilson, Christopher J. Thomas, Alexandra Guerrero, Christine C. Shepard, Borja G. Reguero, Guillermo Franco, Jane Carter Ingram, and Dania Trespalacios. 2017. “The Value of Coastal Wetlands for Flood Damage Reduction in the Northeastern USA.” *Scientific Reports* 7 (1): 1–12. https://doi.org/10.1038/s41598-017-09269-z.

Nederhoff, Kees, Saleh Rohin, Babak Tehranirad, Liv Herdman, Li Erikson, Patrick L. Barnard, and Mick van der Wegen. 2021. “Drivers of Extreme Water Levels in a Large, Urban, High-Energy Coastal Estuary – A Case Study of the San Francisco Bay.” *Coastal Engineering*.

Nowacki, Daniel J., Alexis Beudin, and Neil K. Ganju. 2017. “Spectral Wave Dissipation by Submerged Aquatic Vegetation in a Back-Barrier Estuary.” *Limnology and Oceanography* 62 (2): 736–53. https://doi.org/10.1002/lno.10456.

O’Neill, A. C., L. H. Erikson, and P. L. Barnard. 2017. “Downscaling Wind and Wavefields for 21st Century Coastal Flood Hazard Projections in a Region of Complex Terrain.” *Earth and Space Science* 4 (5): 314–34. https://doi.org/10.1002/2016EA000193.

Pinsky, Malin L., Greg Guannel, and Katie K. Arkema. 2013. “Quantifying Wave Attenuation to Inform Coastal Habitat Conservation.” *Ecosphere* 4 (8). https://doi.org/10.1890/ES13-00080.1.

Powell, Emily J., Megan C. Tyrrell, Andrew Milliken, John M. Tirpak, and Michelle D. Staudinger. 2019. “A Review of Coastal Management Approaches to Support the Integration of Ecological and Human Community Planning for Climate Change.” *Journal of Coastal Conservation* 23 (1): 1–18. https://doi.org/10.1007/s11852-018-0632-y.

Putnam, J A. 1949. “Loss of Wave Energy Due to Percolation in a Permeable Sea Bottom.” *Transactions, American Geophysical Union* 30 (3).

Putnam, J A, and J W Johson. 1949. “The Dissipation of Wave Energy by Bottom Friction” 30 (1).

Quataert, Ellen, Curt Storlazzi, Arnold van Rooijen, Olivia Cheriton, and Ap van Dongeren. 2015. “The Influence of Coral Reefs and Climate Change on Wave-Driven Flooding of Tropical Coastlines” 42: 6407–15. https://doi.org/10.1002/2015GL064861.Received.

Ranasinghe, Roshanka, Trang Minh Duong, Stefan Uhlenbrook, Dano Roelvink, and Marcel Stive. 2013. “Climate-Change Impact Assessment for Inlet-Interrupted Coastlines.” *Nature Climate Change* 3 (1): 83–87. https://doi.org/10.1038/nclimate1664.

Reguero, Borja G., Curt D. Storlazzi, Ann E. Gibbs, James B. Shope, Aaron D. Cole, Kristen A. Cumming, and Michael W. Beck. 2021. “The Value of US Coral Reefs for Flood Risk Reduction.” *Nature Sustainability* 4 (8): 688–98. https://doi.org/10.1038/s41893-021-

00706-6.

Roelvink, Dano, Robert McCall, Seyedabdolhossein Mehvar, Kees Nederhoff, and Ali Dastgheib. 2018. “Improving Predictions of Swash Dynamics in XBeach: The Role of Groupiness and Incident-Band Runup.” *Coastal Engineering* 134 (July 2017): 103–23. https://doi.org/10.1016/j.coastaleng.2017.07.004.

Roelvink, Dano, Ad Reniers, Ap van Dongeren, Jaap van Thiel de Vries, Robert McCall, and Jamie Lescinski. 2009. “Modelling Storm Impacts on Beaches, Dunes and Barrier Islands.” *Coastal Engineering* 56 (11–12): 1133–52. https://doi.org/10.1016/j.coastaleng.2009.08.006.

Schile, Lisa M., John C. Callaway, James T. Morris, Diana Stralberg, V. Thomas Parker, and Maggi Kelly. 2014. “Modeling Tidal Marsh Distribution with Sea-Level Rise: Evaluating the Role of Vegetation, Sediment, and Upland Habitat in Marsh Resiliency.” *PLoS ONE* 9 (2). https://doi.org/10.1371/journal.pone.0088760.

Shemdin, O., K. Hasselmann, S. V. Hsiao, and K. Herterich. 1978. “Nonlinear and Linear Bottom Interaction Effects in Shallow Water.” In *Turbulent Fluxes Through the Sea Surfae, Wave Dunami and Prediction*, 347–72. New York: Plenum Press. https://doi.org/10.1007/978-1-4612-9806-9_23.

Shen, Jian, Harry Wang, Mac Sisson, and Wenping Gong. 2006. “Storm Tide Simulation in the Chesapeake Bay Using an Unstructured Grid Model.” *Estuarine, Coastal and Shelf Science* 68 (1): 1–16. https://doi.org/10.1016/j.ecss.2005.12.018.

Shepard, Christine C., Caitlin M. Crain, and Michael W. Beck. 2011. “The Protective Role of Coastal Marshes: A Systematic Review and Meta-Analysis.” *PLoS ONE* 6 (11). https://doi.org/10.1371/journal.pone.0027374.

Smit, Pieter, Marcel Zijlema, and Guus Stelling. 2013. “Depth-Induced Wave Breaking in a Non-Hydrostatic, near-Shore Wave Model.” *Coastal Engineering* 76: 1–16. https://doi.org/10.1016/j.coastaleng.2013.01.008.

Stockdon, Hilary F., Rob A. Holman, Peter A. Howd, and Asbury H. Sallenger. 2006. “Empirical Parameterization of Setup, Swash, and Runup.” *Coastal Engineering* 53 (7): 573–88. https://doi.org/10.1016/j.coastaleng.2005.12.005.

Storlazzi, Curt D., Borja G. Reguero, Aaron D. Cole, Erik Lowe, James B. Shope, Ann E. Gibbs, Barry A. Nickel, Robert T. McCall, Ap R. van Dongeren, and Michael W. Beck. 2019. “Rigorously Valuing the Role of U . S . Coral Reefs in Coastal Hazard Risk Reduction: U.S. Geological Survey Open File Report 2019-1027.” https://doi.org/10.3133/ofr20191027.

Stralberg, Diana, Matthew Brennan, John C. Callaway, Julian K. Wood, Lisa M. Schile, Dennis Jongsomjit, Maggi Kelly, V. Thomas Parker, and Stephen Crooks. 2011. “Evaluating Tidal Marsh Sustainability in the Face of Sea-Level Rise: A Hybrid Modeling Approach Applied to San Francisco Bay.” *PLoS ONE* 6 (11). https://doi.org/10.1371/journal.pone.0027388.

Stutz, Matthew L., A. W. Sam Smith, and Orrin H. Pilkey. 1998. “Differing Mechanisms of Wave Energy Dissipation in the Wave Shoaling Zone, Surf Zone and Swash Zone; Why a

Uniform Rate of Wave Energy Dissipation Is Impossible; Proceedings of the International Coastal Symposium (ICS98)." *International Coastal Symposium (ICS98), Palm Beach, FL, United States, May 19-23, 1998* Special is (26): 214–18.

Suzuki, Tomohiro, Marcel Zijlema, Bastiaan Burger, Martijn C. Meijer, and Siddharth Narayan. 2012. "Wave Dissipation by Vegetation with Layer Schematization in SWAN." *Coastal Engineering* 59 (1): 64–71. https://doi.org/10.1016/J.COASTALENG.2011.07.006.

Swanson, Kathleen M., Judith Z. Drexler, David H. Schoellhamer, Karen M. Thorne, Mike L. Casazza, Cory T. Overton, John C. Callaway, and John Y. Takekawa. 2014. "Wetland Accretion Rate Model of Ecosystem Resilience (WARMER) and Its Application to Habitat Sustainability for Endangered Species in the San Francisco Estuary." *Estuaries and Coasts* 37 (2): 476–92. https://doi.org/10.1007/s12237-013-9694-0.

Sweet, W. V., R. E. Kopp, C. P. Weaver, J. Obeysekera, R. M. Horton, E. R. Thieler, and Chris Zervas. 2017. "Global and Regional Sea Level Rise Scenarios for the United States," no. NOS CO-OPS 083: 75. https://tidesandcurrents.noaa.gov/publications/techrpt83_Global_and_Regional_SLR_Scenarios_for_the_US_final.pdf.

Sweet, W. V., B. D. Hamlington, R. E. Kopp, C. P. Weaver, P. L. Barnard, D. Bekaert, W. Brooks, et al. 2022. "Global and Regional Sea Level Rise Scenarios for the United States: Updated Mean Projections and Extreme Water Level Probabilities along U.S. Coastlines."

Taherkhani, Mohsen, Sean Vitousek, Patrick L. Barnard, Neil Frazer, Tiffany R. Anderson, and Charles H. Fletcher. 2020. "Sea-Level Rise Exponentially Increases Coastal Flood Frequency." *Scientific Reports* 10 (1): 1–18. https://doi.org/10.1038/s41598-020-62188-4.

Takekawa, J. Y., K. M. Thorne, K. J. Buffington, K. A. Spragens, K. M. Swanson, J. Z. Drexler, D. H. Schoellhamer, C. T. Overton, and M. L. Casazza. 2013. "Final Report for Sea-Level Rise Response Modeling for San Francisco Bay Estuary Tidal Marshes." *U.S. Geological Survey Open File Report 2012-1081*, 161.

Talke, S. A., and M. T. Stacey. 2003. "The Influence of Oceanic Swell on Flows over an Estuarine Intertidal Mudflat in San Francisco Bay." *Estuarine, Coastal and Shelf Science* 58 (3): 541–54. https://doi.org/10.1016/S0272-7714(03)00132-X.

Tommasini, Laura, Luca Carniello, Massimiliano Ghinassi, Marcella Roner, and Andrea D'Alpaos. 2019. "Changes in the Wind-Wave Field and Related Salt-Marsh Lateral Erosion: Inferences from the Evolution of the Venice Lagoon in the Last Four Centuries." *Earth Surface Processes and Landforms* 44 (8): 1633–46. https://doi.org/10.1002/esp.4599.

van Rooijen, A. A., R. T. McCall, J. S. M. van Thiel de Vries, A. R. van Dongeren, A. J. H. M Reniers, and J. A. Roelvink. 2016. "Modeling the Effect of Wave Vegetation Interaction on Wave Setup." *Journal of Geophysical Research: Oceans* 121. https://doi.org/10.1002/2015JC011486.Received.

van Rooijen, A. A., J .S. M. van Thiel de Vries, R. T. McCall, A. R. van Dongeren, J. A. Roelvink, and A. J. H. M. Reniers. 2015. “Modeling of Wave Attenuation by Vegetation with XBeach.” *E-Proceedings of the 36th IAHR World Congress*, 7.

van Wesenbeeck, Bregje K., Guido Wolters, José A.A. Antolínez, Sudarshini A. Kalloe, Bas Hofland, Wiebe P. de Boer, Ceylan Çete, and Tjeerd J. Bouma. 2022. “Wave Attenuation through Forests under Extreme Conditions.” *Scientific Reports* 12 (1): 1–8. https://doi.org/10.1038/s41598-022-05753-3.

Vitousek, Sean, Patrick L. Barnard, Charles H. Fletcher, Neil Frazer, Li H. Erikson, and Curt D. Storlazzi. 2017. “Doubling of Coastal Flooding Frequency within Decades Due to Sea-Level Rise.” *Nature Scientific Reports* 7: 1–9. https://doi.org/10.1038/s41598-017-01362-7.

Ward, Kristen M., John C. Callaway, and Joy B. Zedler. 2003. “Episodic Colonization of an Intertidal Mudflat by Native Cordgrass (Spartina Foliosa) at Tijuana Estuary.” *Estuaries* 26 (1): 116–30. https://doi.org/10.1007/BF02691699.

Woo, I., and J. Y. Takekawa. 2012. “Will Inundation and Salinity Levels Associated with Projected Sea Level Rise Reduce the Survival, Growth, and Reproductive Capacity of Sarcocornia Pacifica (Pickleweed)?” *Aquatic Botany* 102: 8–14. https://doi.org/10.1016/j.aquabot.2012.03.014.

Wright, L. D., and A. D. Short. 1984. “Morphodynamic Variability of Surf Zones and Beaches: A Synthesis.” *Marine Geology* 56 (1–4): 93–118. https://doi.org/10.1016/0025-3227(84)90008-2.

Xiao, Hong, Wenrui Huang, and Jianhua Tao. 2009. “Numerical Modeling of Wave Overtopping a Levee during Hurricane Katrina.” *Computers and Fluids* 38 (5): 991–96. https://doi.org/10.1016/j.compfluid.2008.01.025.

Ysebaert, Tom, Shi Lun Yang, Liquan Zhang, Qing He, Tjeerd J. Bouma, and Peter M.J. Herman. 2011. “Wave Attenuation by Two Contrasting Ecosystem Engineering Salt Marsh Macrophytes in the Intertidal Pioneer Zone.” *Wetlands* 31 (6): 1043–54. https://doi.org/10.1007/s13157-011-0240-1.

Zelst, Vincent T.M. van, Jasper T. Dijkstra, Bregje K. van Wesenbeeck, Dirk Eilander, Edward P. Morris, Hessel C. Winsemius, Philip J. Ward, and Mindert B. de Vries. 2021. “Cutting the Costs of Coastal Protection by Integrating Vegetation in Flood Defences.” *Nature Communications* 12 (1): 1–11. https://doi.org/10.1038/s41467-021-26887-4.

Zhao, Dongliang, and Moxin Li. 2019. “Dependence of Wind Stress across an Air – Sea Interface on Wave States.” *Journal of Oceanography* 75 (3): 207–23. https://doi.org/10.1007/s10872-018-0494-9.

Zijlema, Marcel, Guus Stelling, and Pieter Smit. 2011. “SWASH : An Operational Public Domain Code for Simulating Wave Fi Elds and Rapidly Varied Fl Ows in Coastal Waters.” *Coastal Engineering* 58 (10): 992–1012. https://doi.org/10.1016/j.coastaleng.2011.05.015.

2. The value of marsh restoration for flood risk reduction in an urban estuary

Abstract

Incorporating nature-based solutions (NBS) into coastal climate adaptation is of broad and growing interest, but NBS are rarely assessed with the same rigor as traditional engineering solutions or with respect to future climate change. This gap poses challenges for the use of NBS for climate adaptation. We value the flood protection benefits of stakeholder-identified marsh restoration under current and future climate change within San Francisco Bay, a densely urbanized estuary, focusing on San Mateo County, the California county most vulnerable to future flooding. Marsh restoration provides a present value of $21 million which increases to over $100 million with 0.5 m of sea level rise (SLR), and to about $500 million with 1 m of SLR. We identify hotspots where marsh restoration delivers the highest benefits for adaptation, which reach $9 million/hectare. Today's investments in nature and community resilience can result in increasing payoffs as climate change progresses and risk increases.

2.1 Introduction

Climate change is raising sea levels and increasing the threat of coastal flooding. By 2100, sea level is expected to rise 0.6 to 2.2 m along the contiguous United States, primarily due to the melting of ice sheets and glaciers, and thermal expansion of seawater (Sweet et al. 2022), which will significantly increase coastal flooding (Vitousek et al., 2017; Taherkhani et al., 2020). Flooding due to sea-level rise (SLR) is amplified by storms, which drive higher coastal water levels via surge, waves, and increased river discharge (Barnard et al. 2019). Increasing coastal population density further compounds the consequences of flooding. More than 600 million people live in the coastal zone, a number which is expected to increase to more than

1 billion by 2050 (Merkens et al. 2016). These factors combine to create high and rising flood risk on coasts around the world.

Recent research suggests that in California, 675,000 people and $250 billion in property are at risk of flooding in a scenario with 2 m of sea level rise combined with a 100-year storm (*Hazard Reporting and Analytics (HERA)*, 2017; Barnard et al., 2019). The population bordering San Francisco Bay ("the Bay Area") accounts for two-thirds of future flooding impacts in California, and the cost of raising Bay area coastal protection structures to prepare for 2 m of SLR could reach $450 billion (Hirschfeld and Hill 2017). Across California and the West Coast of the United States West Coast, the communities bordering low-lying urban estuarine environments including Puget Sound, San Francisco Bay, and smaller Southern California lagoons and estuaries are all highly vulnerable to flooding, resulting in the majority of socio-economic exposure of the U.S. West Coast (Barnard et al. 2019).

Within California, San Mateo County has the most projected flood exposure due to climate change, with more than 140,000 people and $50 billion of property exposed to flooding through this century ("Hazard Reporting and Analytics (HERA)" 2017). Communities are already beginning to experience these impacts. San Mateo County's bay shoreline (Figure 2.1B and Figure 2.1B) is highly altered and contains critical public infrastructure, including the San Francisco International Airport (SFO, Figure 2.1B), touchdowns of two regional bridges, an interstate highway, the heart of the Silicon Valley technology industry, and over 750,000 residents. Levees are an essential component of flood control throughout the region (San Francisco Estuary Institute (SFEI) 2016). Much of the urban coast is built on historical wetlands that have been drained, diked, and filled; wetlands have also been diked to create

ponds for industrial salt production (Goals Project, 2015). The result of this filling, diking, and development of former tidal marshes is that San Mateo County is one of only six counties in the country with over 100,000 residents at risk of flooding with 0.9 m of SLR (Hauer et al. 2016).

Communities in San Francisco Bay rely heavily on gray infrastructure (primarily levees and seawater pumping) for flood protection today, but a wide variety of pathways for integrating nature-based shorelines have been identified regionally (Beagle et al., 2019; BCDC, 2020; *Bay Adapt: Regional Strategy for a Rising Bay*, 2021). There is strong interest in the use of wetlands in reducing flooding – in 2016, Bay Area voters passed Measure AA, which uses a $12 per year parcel tax to restore wetlands to prepare for climate change (Gutierrez 2016) in addition to providing other co-benefits including supporting fish and wildlife and carbon sequestration (Callaway et al., 2012; Pinsky et al., 2013; Narayan et al., 2017; Foster-Martinez et al., 2018). However, coastal development has altered or removed up to 90% of the Bay's historical tidal wetlands (Safran et al. 2013), resulting in dramatic habitat loss and fragmentation. In San Mateo County, large marshes in the northern part of the county were buried and developed to create planned communities; in the southern part of the county, marsh habitat was diked and drained to create ponds for salt production. In the past several decades, marsh restoration has emerged as a unifying management objective in the Bay, particularly restoration of legacy salt ponds (Callaway et al., 2007, Brew & Williams, 2010; 2011; Foxgrover et al., 2019). San Mateo County's tidal marshes are among the highest ranked for conservation priority across the Bay (Veloz et al. 2013). Marshes receive sediment supply from suspended sediment deposition during periods of flooding, a process that

facilitates vertical accretion (Lacy et al. 2020). A large portion of San Mateo County's bay coast is historical marsh that has been diked to prevent tidal flooding (San Francisco Estuary Institute (SFEI) 1999); many historical diked marshes have subsided in elevation and are no longer high enough to support a full range of marsh vegetation. Marsh restoration in the region usually includes strategic breaching of levees across historical channels (Figure 2.1D) to allow inundation and sedimentation to occur in diked historical marsh (Figure 2.1C), facilitating revegetation by native marsh plants (Figure 2.1E and Figure 2.1F).

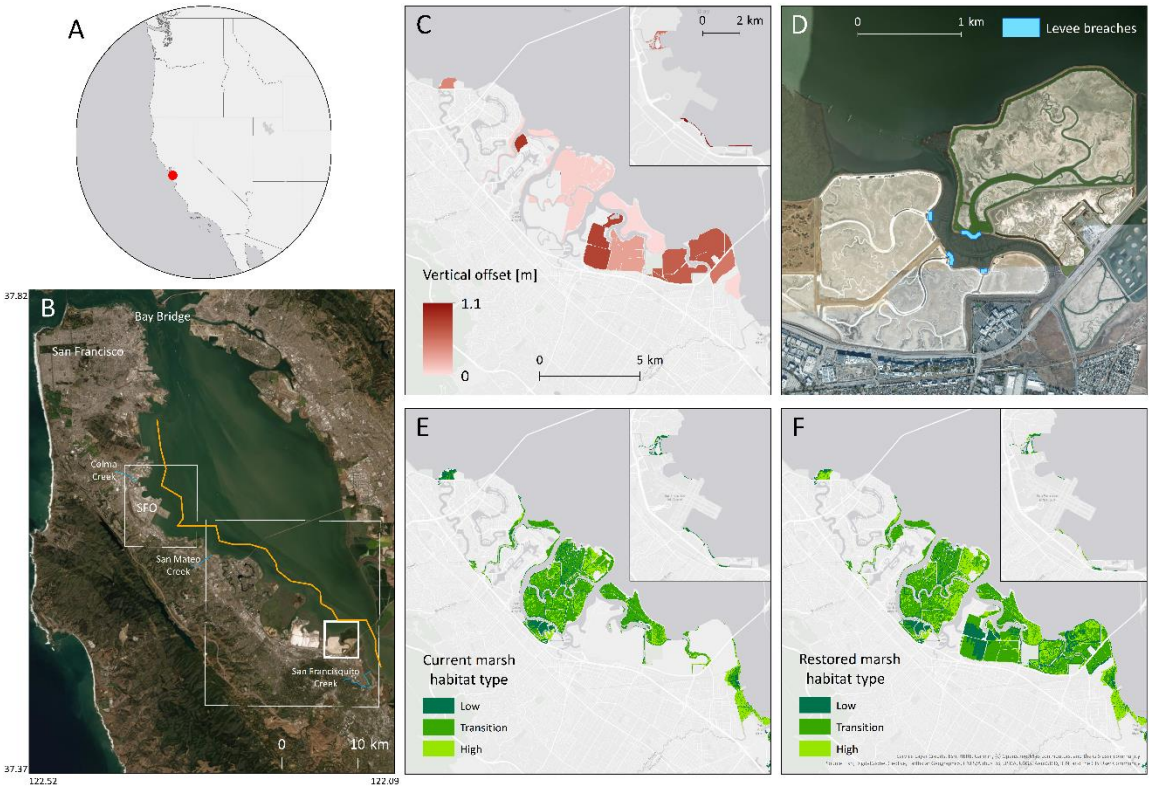

Figure 2.1 Location of the study area and details of the simulated restorations. (A) and (B) Location of this study, shown by the red dot in (A) and the orange line in (B). The thin white boxes in (B) show the extent of the maps in (C), (E) and (F) and the thick white box in (B) shows the extent of the map in (D). (C) Vertical offset applied to the restoration sites to simulate sediment accretion/nourishment, bringing each site to +1 m relative to mean sea level. These values range from 0.05 to 1.1 m. (D) Levee breaches across historical marsh channels to facilitate tidal connectivity in salt ponds are shown in

blue. (E) Current and (F) restored marsh habitat types, determined by elevation relative to tidal datum. The three shades of green, from dark to light, denote low, transition, and high marsh habitat.

With the highest future flood risk in the state and large areas of wetlands with potential for restoration, San Mateo County's shoreline is a key study site for investigating the potential of marsh restoration as a nature-based flood defense. Few studies have quantified the flood risk reduction benefits provided by habitat (Reguero et al. 2018). Even fewer assess benefits of habitat restoration (Gourevitch et al., 2020; Storlazzi et al., 2021; Beck et al., 2022; Martínez-García et al., 2022) and none have rigorously quantified the value of restored habitat under climate change. Impacts of climate change present pressing challenges to coastal communities and assessments of the benefits of both natural and artificial infrastructure will need to account for these challenges. Here, we address this gap by assessing the flood risk reduction benefits of marsh restoration projects in San Francisco Bay, under current and future climate conditions, to characterize how and where they provide climate adaptation benefits now and into the future.

2.2 Methods

2.2.1 Model description

The Delft3D Flexible Mesh modeling suite (Delft3D Flexible Mesh 2020.04, Deltares, 2022) and Simulating WAves Nearshore (SWAN, Booij et al., 1999) were two-way coupled to assess the flood impacts of marsh restoration. Delft3D FM solves the shallow-water equations on staggered unstructured grids in one-, two-, and three-dimensional schematizations with a finite volume method. Here, we ran the model in a two-dimensional-horizontal schematization, which simulates depth-averaged flow. SWAN, a third-generation, phase-

averaged numerical wave model, simulates the propagation of waves from deep to shallow waters by solving the energy balance and action balance equations. The use of the energy spectrum through these equations allows models such as SWAN to significantly reduce computational time, but as a result, they do not resolve individual waves. Wave-current interactions are simulated in the coupled model, and result in changes in current refraction, bottom friction, wave setup, turbulence, and bed shear stress. Thus, this model includes tides, steric changes in water level, creek discharge, wave setup, and relative SLR. This model does not account for swash, which requires a wave-resolving model.

The domain for this model was adapted from Tehranirad et al. (2020), and the approach was based on the Coastal Storm Modeling System (Barnard et al. 2014; 2019). The open boundary was perpendicular to the main bay channel, approximately 5 km south of the Bay Bridge. The grid resolution was increased over existing and potential marsh habitat to ~10 m, to capture complex bathymetry and tidal channels of the marshes (Figure S2.1). Bathymetry was derived from a Lidar Elevation Adjustment with NDVI (LEAN)-corrected 5-m horizontal resolution digital elevation model, used above -1 m NAVD88 (Buffington & Thorne, 2018). The LEAN-correction facilitates the Lidar collected elevation data to capture the mudflat rather than the top of marsh plants. 10-m resolution model was used below -1 m NAVD88 (Fregoso et al., 2017). The tidal constituents at the open model boundary for this model are derived from the FES Global Tide Model ("FES Global Tide Model" 2014). Constituents were calibrated to maximize model-data agreement.

Land cover type was determined the National Land Cover Database (Homer et al. 2020), which details satellite-derived land cover nationally. Open water Manning's friction values

were set to 0.02, following Tehranirad et al. (2020) and supported by sensitivity testing. Vegetation was represented implicitly with Manning's friction coefficients of 0.03, 0.035, and 0.04 for low, transition, and high marsh zones, respectively. These values follow those suggested by Bunya et al. (2010) and DHI (2013).

Tidal vegetation location in the Bay Area Aquatic Resources Inventory (BAARI, San Francisco Estuary Institute & Aquatic Science Center (SFEI ASC) 2015) was used to determine marsh habitat locations. Because marsh plants are sensitive to flooding periods (Takekawa et al. 2013), the extents of the three different marsh vegetation zones were determined based on elevation relative to tidal data (mean sea level, or MSL, and mean higher high water, or MHHW). This was done using z* as a metric, following the methods established by Beagle et al. (2019): $z* = \frac{land\ surface\ elevation - MSL}{MHHW - MSL}$. Areas with a z* value between 1.02 and 1.38 were assumed to support high marsh; locations with a z* value between 0.75 and 1.02 were assumed to support transition marsh; locations with a z* value between -0.14 and 0.75 were assumed to support low mash(Beagle et al. 2019). MHHW and MSL were determined from values reported in Appendix 5 of Beagle et al. (2019) and assumed to be constant across the domain. This assumption neglects the regional < 20 cm variation in MHHW. MSL was assumed to be 1.00 m NAVD88 and MHHW was assumed to be 2.12 m NAVD88. Flood control infrastructure was included as a sub-grid feature with location determined from the San Francisco Estuary Institute's Bay Shore Inventory (San Francisco Estuary Institute (SFEI) 2016), and height determined from the most highly resolved DEM available (Danielson et al. 2016). The two gauged creeks in the study region are San Francisquito Creek and San Mateo Creek (Figure S2.1), and both were included in the model, allowing for the simulation of

flooding driven by high offshore water-levels as well as upland flooding driven by high creek flows.

2.2.2 Calibration and validation

To calibrate the model, non-tidal residuals (NTR) at the model boundary were derived from a 70-year model hindcast developed by Tehranirad et al. (2020) and Nederhoff et al. (2021). This hindcast, which spans from 1950 to 2020, was forced with tides and ERA5 30-km resolution winds (Hersbach et al. 2020), which provide a longer temporal record than other hindcasts of finer resolution, facilitating a more robust calibration. A low pass filter was used to remove the tidal signal from the 70-yr time series, and to generate the NTR signal, which was used to force Delft3D. For calibration and validation, waves were simulated with the built-in fetch-limited wave formulation, which is more computationally efficient than SWAN, and forced with Rapid Refresh wind hindcasts (Benjamin et al. 2016). This data is resolved to 13 km, which is lower than many other hindcast winds, but it is the only available data for the study region during the calibration period. Flow rates for San Mateo and San Francisquito creeks were derived from USGS gauges (*National Water Information System Data Available on the World Wide Web (USGS Water Data for the Nation)*, 2016).

Modeled water-levels were compared to measurements collected by the NOAA Redwood City Tide Gauge (NOAA, 2021) and by a water logger deployed in Laumeister Marsh during storms in 2010 and 2011 (Thorne et al. 2013). The months of January 2010 and March 2011, which included significant storms and extreme high water-levels, were used for calibration and validation, respectively. The amplitude and phase offset of individual tidal constituents were compared between the modeled and observed data. The differences were used to

adjust to the FES constituents on the boundary to improve model data agreement (Figure S2.2 and S2.3). Root mean square error (RMSE) for the calibration period was 9 and 12 cm at Redwood City and Laumeister Marsh, respectively, and 10 and 20 cm at Redwood City and Laumeister Marsh, respectively, for the validation period. The full tidal amplitude at both sites is about 2.5 m and 1.5 m, respectively.

Model-observation agreement was initially very poor in Laumeister Marsh because the marsh channel in which observations were taken was unresolved in the 5-m resolution DEM and the 10-m resolution model grid. Thus, to facilitate model-observation comparison in Laumeister Marsh, channel depth was increased manually. Simulations with varying marsh platform height and marsh channel depth were done during the calibration period to assess the model sensitivity to marsh bathymetry. This analysis revealed that model data agreement in Laumeister Marsh is most strongly sensitive to channel depth, and less sensitive to platform elevation. Results from the sensitivity analysis are shown in Table S2-1. After manually adjusting channel depth, a systematic bias was still present in the Laumeister Marsh model-data agreement. This bias is likely due to uncertainty in marsh channel depth in Laumeister Marsh.

2.2.3 Hydrodynamic simulations

To understand how marsh habitat restoration influences flood depth and extent, simulations with existing marshes and potential restoration projects were compared under various sea level and storm conditions, including: 0, 0.5, and 1.0 m of SLR, within the range of most updated intermediate estimates for California by 2100 (Sweet et al. 2022), along with annual, 20-year and 100-year storm conditions. For each of these SLR scenarios, several marsh

habitat distributions were simulated, including existing marsh, as defined by San Francisco Estuary Institute & Aquatic Science Center (SFEI ASC, 2015), and an extensive regional restoration. The simulated marsh restorations were identified in close collaboration with local flood managers over a series of workshops, with the goal of developing plausible scenarios of marsh restoration to assess effects on flood risk in the study region.

Storm water levels and wind and pressure time series were derived from Barnard et al. (2014) and Barnard et al. (2019). These were originally developed for the Coastal Storm Modeling System (CoSMoS). A 21st century total water level proxy time-series was created from global climate model sea surface temperatures, winds, sea level pressures, and water levels from this time series were ranked. Mean, annual, 20-yr, and 100-yr events occurring on future dates were extracted from the ranked water levels. Local models were forced with downscaled 21st century wind and pressure for the future dates. These storms were run in combination with plausible 21st century increases in sea level, thus capturing non-linear interactions between waves and water levels. These downscaled 21st century storms were used as boundary conditions in the present work.

Data from the tide gauge closest to the open boundary, located in Alameda (NOAA, 2021), were appended before and after the 50-hour storm water level time series at the open boundary, to facilitate isolating NTR from changes in water level due to tides. A low-pass filter was used to derive the NTR. This caused the storm water levels to become non-progressive in the second day of the simulation, so water levels from the first day of the simulation were used to determine maximum flood depth.

Creek flows for San Francisquito Creek were derived from Erikson et al. (2018), which determined flow rates for 8 California creeks and rivers coincident with annual, 20-yr, and 100-yr 21st century storms based on a 21st century time series of flow for the Sacramento/San Joaquin Delta (Knowles et al., 2015). San Mateo Creek was not included in that analysis, so flow rates for San Mateo Creek were determined by the same percentile of flow from the stream gauge as flow rates from San Francisquito Creek, which is 20 km away. This approach neglects localized watershed differences in normalized flow rates.

The study region is home to low-lying marshes, which, though presently classified as marsh habitat, are too low in elevation to support a full range of marsh vegetation. In such locations, the restoration projects assume sediment nourishment and re-vegetation that would bring the sites to a mean elevation of 2 m NAVD88, or +1 m relative to regional MSL, which is representative of healthy marshes in San Francisco Bay (Takekawa et al. 2013). The uniform elevation increase was applied to sites that were identified by stakeholders as potential restoration sites (Figure 2.1C). Vegetation zones were shifted according to the new z***** score (Figure 2.1E and Figure 2.1F). For the 0.5 and 1.0 m SLR scenarios, vegetation zones were modified to represent the corresponding upward and landward shift of marsh vegetation zones caused by an increase in mean sea level. The simulated restorations also included breaching several levees surrounding salt ponds. We used satellite and historical photography, as well as conversations with stakeholders, to determine locations for the breaches, which are made across historical channels (Figure 2.1D).

The restoration sites and projects were implemented using the most recently available data on marsh distribution and levee location. However, certain sections of the region's levee

system have been breached since the SFEI Bayshore Inventory was published in 2016 and a section of Bair Island has been restored to marsh habitat from open water in recent years. To ensure hydrodynamics in the model reflect the current state of the study region, we manually edited the datasets for marsh distribution and levee elevation based on stakeholder input.

2.2.4 Flood damages and socioeconomic analysis

To calculate flood damages on buildings, we used the Federal Emergency Management Association's (FEMA's) Flood Assessment Structure Tool (FAST, Hazus, 2021). FAST connects FEMA's Hazus depth-damage curves with flood maps and built infrastructure inventories to quantify flood damages. Depth-damage curves quantify damage to a structure as flood depths increase, using curves that vary by structure type. The exposure data was obtained from the National Structure Inventory (NSI, "National Structure Inventory", 2019), which includes information on structure replacement cost, content cost, material type, basement type, and number of floors. NSI includes about 200,000 structures in San Mateo County. NSI and the flood depth maps produced from the hydrodynamic model were used as inputs to FAST, which determines the appropriate depth-damage curve for each structure and the resulting economic damage. Damages across all structures in the domain were aggregated to quantify economic impacts of flooding. Flood damages were calculated with and without the restoration projects.

The damages associated with each return period flood zone were used to determine the annual expected damage, which represents the frequency-weighted sum of damages for the full range of flood events and is a measure of flood risk per year (e.g., Reguero et al., 2021):`

$Annual\ expected\ damage\ (AED) = \frac{1}{2}\sum_{i=1}^{n}\left(\frac{1}{T_i} - \frac{1}{T_{i+1}}\right)(D_i + D_{i+1})$, where *i* represents the number of return periods, T_i represents the return period, and D_i represents the damage associated with a storm with a return period of T_i, following the formula for trapezoidal integration. The difference in damage between the baseline flooding and the flooding with habitat scenarios determines the avoided damages provided by the restoration projects. The annual expected benefit (AEB) of the restoration projects can be calculated as the differences with the baseline situation (without restoration):

$Annual\ expected\ benefit\ (AEB) = AED_{existing} - AED_{restored}$. To discount future benefits of adaptation investments (Reguero et al. 2018), the present value of the projects was determined by summing annual expected benefit over the lifetime of the project, represented by *n*, and discounting the benefits of each future year by *i:*

$Present\ Value\ (PV) = \sum \frac{AEB_n}{(1+i)^n}$. We assumed the project lifespan to be 50 years and included several discount rates (Reguero et al. 2018). 7% is the standard value used by the US Army Corps of Engineers.

The number of people affected by impacts of marsh restoration on flooding in San Mateo County was determined following a similar approach. Population across each census block-group (BCDC et al., 2020) was assumed to be evenly distributed between residential buildings, and population impacted was determined by whether a residential structure was flooded. Thus, for determining the social impacts of marsh restoration, the annual expected damage equation was used, where D_i = residences flooded per census block group × population of CBG ÷ total residences in CBG. Absolute and percent in social and economic risk with habitat restoration and without can be found in Table S2-3.

The San Francisco Bay Conservation and Development Commission's Adapting to Rising Tides project has ranked social vulnerability of census block groups based on demographics (BCDC et al., 2020). Social vulnerability of census block-group was determined through 12 indicators (Table S2-2). In this work, we considered most vulnerable census block groups to be those marked as "high social vulnerability" and "highest social vulnerability".

2.2.5 Discussion of uncertainties in the flood risk model.

Uncertainty is introduced into this model at numerous points. The main uncertainty sources of analyses like this involve the hydrodynamic modelling, bathymetry, elevation, damage models and socioeconomic changes (Reguero et al. 2021). This model includes local defense structures, but results are sensitive to the height of the levees in the model. Thus, the hydrodynamic analysis can be considered conservative in the difference between existing and marsh restoration scenarios, but the absolute flood results may be non-conservative in certain areas, such as behind levees where the crest height is not fully resolved. There may be unresolved hydraulic connectivity in some places, which could result in an underestimate of flood extents. Studies specifically focused on characterizing the uncertainty in coastal flood damage models at local scales have determined that the greatest sources of uncertainty are the elevation model and the depth-damage functions (Menendez et al. 2019; Parodi et al. 2020). This analysis relies on bathymetric and topographic data at the highest resolution available for San Francisco Bay. The damage curves for each building type correspond to the official curves included with FEMA-HAZUS, which were developed with local empirical data on building damage vulnerability for the United States. Other additional uncertainty factors affecting the flood results include the forcing conditions (waves, sea levels and storms

duration) and differences in the spatial distribution of building stock and exposure value. To test the sensitivity of results from this work to uncertainty we added and subtracted 25 cm to the resulting flood depths, which is representative of a linear combination of model error (up to 19 cm) and DEM error in San Francisco Bay (6 cm, Buffington et al. 2016), and propagated the resulting uncertainty through the economic analysis, following the methods of Barnard et al. (2019). Results for this can be found in Table S2-4.

2.3 Results

Overall, marsh restoration decreases flood risk, providing a net positive annual expected benefit (AEB) and present value in avoided damage. These benefits increase with SLR; benefits increase by a factor of 5 with 0.5 m SLR and by a factor of more than 20 with 1.0 m SLR (Table 2-1). Population protected by restoration is also shown in Table 2-1. At present sea level, a large portion (43%) of the people who would be protected from flooding due to restoration live in socially vulnerable census block groups. As sea levels rise, the percent of population that is protected by restoration and that is socially vulnerable decreases.

Table 2-1 (A) Property and (B) people protected by marsh restoration in San Mateo County under 3 different sea level rise (SLR) scenarios. Present value is calculated assuming a 50-yr project lifespan, with discount rates of 4, 7, and 10%.

	A				B	
SLR [m]	Annual expected benefit [$ millions]	Present value [$ millions] Discount rate 4%	7%	10%	Number of people who benefit from flood reduction	% of benefits in census block group ranked high or highest social vulnerability
0	1.5	33.2	21.3	15.3	7	43%
0.5	7.6	164.4	105.6	75.9	322	18%
1	36.2	777.2	499.3	358.7	254	9%

Although the present value of marsh restoration is positive, the benefits vary spatially (Figure 2.2). Flood depth reduction benefits are not always directly attributable to a certain restoration site due to complex hydrodynamics, such as channels, creeks, and sloughs. However, the restoration south of SFO, a simple fringing marsh restoration, provides directly attributable benefits. The restoration, which is 14.7 ha in area, produces a present value of $12.7m in flood reduction benefits (at a 7% discount rate), i.e., $0.9m/ha, a value that can be used by planners and managers as a "break-even point" for the cost of restoration. The value of restoration at this site increases substantially with 0.5 m of SLR to $9.2m/ha.

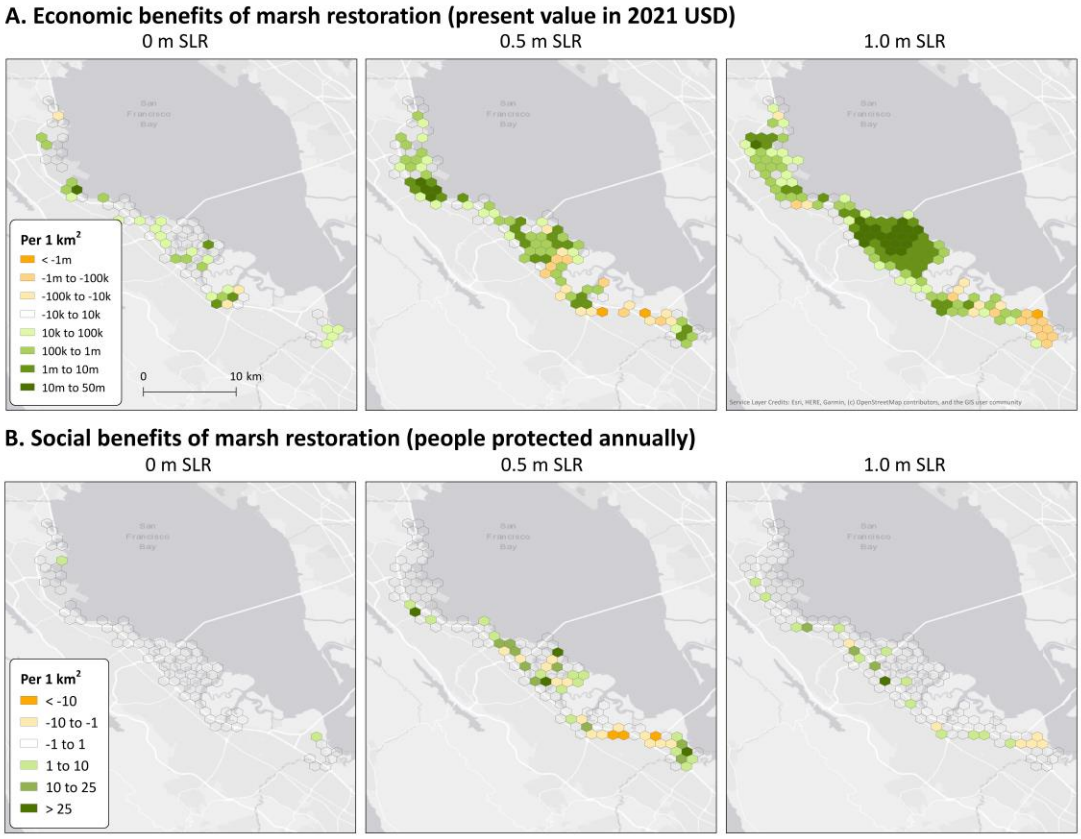

Figure 2.2 Spatial distribution of (A) economic and (B) social flood reduction benefits of marsh restoration with sea level rise. Green colors signify positive present value and people protected while orange colors signify negative present value and increased risk.

Levee height relative to storm water levels is a key determinant of whether a restoration will provide risk reduction benefits. In many locations in the study region and in San Francisco Bay more broadly, marshes front levees. Areas protected by levees will only flood when levees overtop - thus, restoring a marsh on the seaward side of a levee can only reduce flood risk if the levee is at risk of overtopping. This outcome is illustrated by the 100-year flood plain with different sea level scenarios at the mouth of Colma Creek, in the northern end of the study region (Figure 2.3). With 0 m SLR, the restoration provides limited flood depth reduction benefits because the levees lining the creek do not overtop and so there is limited flooding (Figure 2.3B). However, as SLR progresses, water levels from storms will exceed levee height, causing flooding in the lee of the restoration. Therefore, the restoration provides increasing benefits over time (Figure 2.3C and Figure 2.3D). The marsh at Colma Creek, if restored at present sea level, will provide increasing benefits as levees are increasingly overtopped, even as vegetation in the restored marsh restoration migrates upslope where there is space to do so.

Figure 2.3 Effects of marsh restoration and climate change in Colma Creek. (A) shows the study region. (B-D) show reduction in flood heights during a 100-year storm due to habitat restoration with 0, 0.5, and 1.0 m SLR. The green areas represent locations of marsh restoration, the pale blue areas show flood extent, and the bright blue areas represent regions where flood depth is decreased due to the marsh restoration.

2.4 Discussion

We quantified the flood risk reduction benefits provided by marsh restoration under several climate change scenarios in San Mateo County. Overall, marsh restoration provides meaningful flood reduction benefits. The highest value restoration site in our study is a narrow fringing marsh restoration south of San Francisco International Airport (SFO), which provides a present value of $0.9m/ha of restored marsh with 0 m SLR and $9.2m/ha with 0.5

m SLR (Figure 2.2). Countywide, flood reduction benefits increase by a factor of 5 and 23 with 0.5 m and 1.0 m of SLR, respectively. These values are encouraging for managers who may be concerned about the lifespan of marsh restorations in an era of accelerating SLR. Our results indicate that annual benefits will increase into the future as SLR progresses, highlighting high potential benefits for investments in adaptation now.

Results from this analysis can help to prioritize where investments should be made in marsh restoration for flood reduction. In this study system, simple and smaller restorations provide more flood reduction benefit, as measured by amount of avoided damage. Restoration of fringing marshes could be considered as an alternative or a supplement to gray infrastructure solutions as communities adapt to impacts of climate change. Results indicate that restoration of diked and drained historical marshes, such as the salt ponds in this study region, may not provide straightforward flood reduction benefits. Determining how such sites can be restored to produce ecological benefit and flood risk reduction benefit warrants further study. If managers and communities are interested in habitat restoration in the salt ponds, raising levee heights behind the ponds could be considered as part of a green-gray infrastructure solution to restore habitat while keeping adjacent communities safe. These results, along with other work (Foxgrover et al. 2019), highlight the enduring cost of diking and draining marsh habitat, particularly in an era of accelerating SLR.

We simulated a total of 2,937 ha of marsh restoration. Excluding restoration of large offshore islands and current and former salt ponds, which provide the least clear benefits, the total area of restoration is 367 ha. Based on reviews of restoration costs in developed countries, restoring this area of marsh would cost on the order of $70 million (in 2021 USD, Bayraktarov

et al., 2015), which is an order of magnitude lower than present value of restoration with 1.0 m SLR. In contrast, previous work indicates that the cost of raising coastal protection structures along the bay coast of San Mateo County (calculated by determining the % of Bay shoreline in San Mateo County, which is ~12%) to prepare for the highest SLR scenario we explored, 1.0 m, would be $7-18 billion (in 2021 USD, Hirschfeld & Hill, 2017). The restoration scenarios we explored here do not fully protect the county from flooding, but they do meaningfully decrease flood risk. These scenarios could also decrease the height and, thus, cost of shoring up existing hard infrastructure (van Zelst et al. 2021), and cost less than 1% of preparing gray infrastructure for 1.0 m of SLR. Although marsh restoration is unlikely to be a silver bullet solution for communities interested in increasing resilience to SLR and storm-driven flooding, this work demonstrates it can be a part of the solution while simultaneously providing community and ecosystem co-benefits.

Future research should focus on wave-resolved interactions between vegetation, levees, and waves. In this study region, a densely urbanized estuarine coastline with the some of the highest future flood risk in the nation, marshes tend to be on the seaward side of levees. In such settings, we demonstrate that marsh restoration can influence flood depths when levees overtop; however, when levees do not overtop the influence of restoration is limited to reducing damage to the levee system itself. While our work includes phase-averaged (spectral) wave dynamics, SWAN does not model individual waves or wave-wave interactions that are necessary to quantify swash, a key driver of levee overtopping, as well as levee damage. Previous work indicates that marshes can meaningfully reduce dynamic water levels at levees (van Zelst et al. 2021), which, paired with these results, demonstrate that a wave-

resolved investigation of the interactions between levees and marsh vegetation may give insight to how marsh restoration could influence levee overtopping and hydraulic failure.

Our value of benefits is conservative because it does not include additional co-benefits. A valuation of ecosystem services of marsh restoration in northern San Francisco Bay reports that fluvial and storm surge driven flood reduction accounts for 86% of ecosystem service benefits; recreation and water quality improvements account for the remaining 14% of benefits (Calder et al. 2019). If these percentages hold true in San Mateo County, the total benefits of restoration with 0 m SLR would increase from $21 million to $25 million.

Our modeling is conservative because we have not accounted for future changes in marsh height or shape. As sea levels rise, marshes may either vertically accrete, retreat landward, erode, prograde, or drown, depending on sediment supply, location, and morphology. In this study, we assumed that marsh vegetation will retreat upslope and that sites will be squeezed with SLR and transition to mudflat but will otherwise remain the same into the future. This assumption neglects the possibilities of sediment and organic matter accretion on the marsh platform and allowing the marsh elevation to keep up with SLR and maintain vegetation coverage, which could be incorporated using a Marsh Equilibrium Model (MEM, Alizad et al., 2016), though confirmation of this possibility would require detailed marsh biomass measurements and precise marsh elevation measurements, presenting challenges in a regional two-dimensional domain. This assumption also neglects the possibility that the marsh platform will laterally erode or prograde as water levels rise. Surveys indicate that over recent decades, marshes in the northern part of San Francisco Bay, which is more wave exposed than our study region, have exhibited both spatial and temporal variability in edge

change on a local scale (SFEI and Baye 2020). Management interventions to stabilize a marsh edge, such as restoration of oyster reefs, have been shown to be effective in decreasing marsh-edge erosion (Meyer et al. 1997). Some form of marsh-edge stabilization will likely be necessary in the simulations presented here, particularly those including future SLR.

Our results show that marsh restoration can be a cost effective approach to climate adaptation in one of the most at-risk counties in the U.S. Considering future climate scenarios is becoming common practice with traditional infrastructure solutions (Hallegatte et al. 2013; Aerts et al. 2014; de Ruig et al. 2019), and similar approaches should be taken when assessing the potential of nature-based solutions. This work demonstrates that investments in nature and community resilience made today can result in increasing payoffs as climate change progresses and risk increases.

References

Aerts, Jeroen C.J.H., W. J.Wouter Botzen, Kerry Emanuel, Ning Lin, Hans De Moel, and Erwann O. Michel-Kerjan. 2014. "Climate Adaptation: Evaluating Flood Resilience Strategies for Coastal Megacities." *Science* 344 (6183): 473–75. https://doi.org/10.1126/science.1248222.

Alizad, Karim, Scott C Hagen, James T Morris, Stephen C Medeiros, Matthew V Bilskie, and John F Weishampel. 2016. "Earth ' s Future Special Section : Coastal Wetland Response to Sea-Level Rise in a Fluvial Estuarine System Earth ' s Future." https://doi.org/10.1002/eft2.151.

Barnard, Patrick L., Maarten van Ormondt, Li H. Erikson, Jodi Eshleman, Cheryl Hapke, Peter Ruggiero, Peter N. Adams, and Amy C. Foxgrover. 2014. "Development of the Coastal Storm Modeling System (CoSMoS) for Predicting the Impact of Storms on High-Energy, Active-Margin Coasts." *Natural Hazards* 74 (2): 1095–1125. https://doi.org/10.1007/s11069-014-1236-y.

Barnard, Patrick L, Li H Erikson, Amy C Foxgrover, Juliette A Finzi Hart, Patrick Limber, Andrea C O Neill, Maarten Van Ormondt, et al. 2019. "Dynamic Flood Modeling Essential to Assess the Coastal Impacts of Climate Change." *Nature Scientific Reports* 9. https://doi.org/10.1038/s41598-019-40742-z.

"Bay Adapt: Regional Strategy for a Rising Bay." 2021. https://www.bayadapt.org/wp-

content/uploads/2022/01/BayAdapt_JointPlaform_Final_Oct2021.pdf.

Bayraktarov, Elisa, Megan Irene Saunders, Sabah Abdullah, Morena Mills, Jutta Beher, Hugh P. Possingham, Peter J. Mumby, and Catherine E. Lovelock. 2015. "The Cost and Feasibility of Marine Coastal Restoration." *Ecological Applications* 26 (4): 1055–74. https://doi.org/10.1890/15-1077.1.

BCDC, Caltrans, MTC, ABAG, and BARC. 2020. "Adapting to Rising Tides Bay Area, Regional Sea Level Rise Vulnerability and Adaptation Study," no. March: 205. http://www.adaptingtorisingtides.org/project/art-bay-area/.

Beagle, Julie, Jeremy Lowe, Katie McKnight, Sam Safran, Laura Tam, and Sarah Jo Szambelan. 2019. "San Francisco Bay Shoreline Adapation Atlas: Working with Nature to Plan for Sea Level Rise Using Operational Landscape Units."

Beck, Michael W., Nadine Heck, Siddharth Narayan, Pelayo Menéndez, Borja G. Reguero, Stephan Bitterwolf, Saul Torres-Ortega, et al. 2022. "Return on Investment for Mangrove and Reef Flood Protection." *Ecosystem Services* 56: 101440. https://doi.org/10.1016/j.ecoser.2022.101440.

Benjamin, S.G., S.S. Weygandt, J.M. Brown, M. Hu, C.R. Alexander, T.G. Smirnova, J.B. Olson, E.P. James, D.C.; Dowell, and G.A. Grell. 2016. "A North American Hourly Assimilation and Model Forecast Cycle: The Rapid Refresh." *Weather* 144: 1669–94.

Booij, N., R. C. Ris, and L. H. Holthuijsen. 1999. "A Third-Generation Wave Model for Coastal Regions 1. Model Description and Validation." *Journal of Geophysical Research: Oceans* 104 (C4): 7649–66. https://doi.org/10.1029/98JC02622.

Brew, David S., and Philip B. Williams. 2010. "Predicting the Impact of Large-Scale Tidal Wetland Restoration on Morphodynamics and Habitat Evolution in South San Francisco Bay, California." *Journal of Coastal Research* 265 (265): 912–24. https://doi.org/10.2112/08-1174.1.

Buffington, Kevin J., Bruce D. Dugger, Karen M. Thorne, and John Y. Takekawa. 2016. "Statistical Correction of Lidar-Derived Digital Elevation Models with Multispectral Airborne Imagery in Tidal Marshes." *Remote Sensing of Environment* 186 (December): 616–25. https://doi.org/10.1016/j.rse.2016.09.020.

Bunya, S., J. C. Dietrich, J. J. Westerink, B. A. Ebersole, J. M. Smith, J. H. Atkinson, R. Jensen, et al. 2010. "A High-Resolution Coupled Riverine Flow, Tide, Wind, Wind Wave, and Storm Surge Model for Southern Louisiana and Mississippi. Part I: Model Development and Validation." *Monthly Weather Review* 138 (2): 345–77. https://doi.org/10.1175/2009MWR2906.1.

Calder, Ryan S.D., Congjie Shi, Sara A. Mason, Lydia P. Olander, and Mark E. Borsuk. 2019. "Forecasting Ecosystem Services to Guide Coastal Wetland Rehabilitation Decisions." *Ecosystem Services* 39 (September): 101007. https://doi.org/10.1016/j.ecoser.2019.101007.

Callaway, John C., Evyan L. Borgnis, R. Eugene Turner, and Charles S. Milan. 2012. "Carbon

Sequestration and Sediment Accretion in San Francisco Bay Tidal Wetlands." *Estuaries and Coasts* 35 (5): 1163–81. https://doi.org/10.1007/s12237-012-9508-9.

Callaway, John C., V. Thomas Parker, Michael C. Vasey, Lisa M. Schile, and Ellen R. Herbert. 2011. "Tidal Wetland Restoration in San Francisco Bay: History and Current Issues." *San Francisco Estuary and Watershed Science* 9 (3). https://doi.org/10.15447/sfews.2011v9iss3art2.

Callaway, John C., V. Thomas Parker, Michael C. Vasey, and Lisa M. Schile. 2007. "Emerging Issues for the Restoration of Tidal Marsh Ecosystems in the Context of Predicted Climate Change." *Madroño* 54 (3): 234–48. https://doi.org/10.3120/0024-9637(2007)54[234:eiftro]2.0.co;2.

Danielson, Jeffrey J, Sandra K Poppenga, John C Brock, Gayla A Evans, Dean J Tyler, Dean B Gesch, Cindy A Thatcher, and John A Baras. 2016. "Topobathymetric Elevation Model Development Using a New Methodology : Coastal National Elevation Database Topobathymetric Elevation Model Development Using a N Ew Methodology : Coastal N Ational Elevation Database." *Journal of Coastal Research*, no. 76. https://doi.org/10.2112/SI76-008.

"Delft3D Flexible Mesh." 2022. Deltares. https://www.deltares.nl/en/software/delft3d-flexible-mesh-suite/.

DHI. 2013. "Regional Coastal Hazard Modeling Study for South San Francisco Bay."

Erikson, Li H., Andrea C. O'Neill, and Patrick L. Barnard. 2018. "Estimating Fluvial Discharges Coincident with 21st Century Coastal Storms Modeled with CoSMoS." *Journal of Coastal Research* 85: 791–95. https://doi.org/10.2112/si85-159.1.

"FES Global Tide Model." 2014. Noveltis, Legos and CLS. https://www.aviso.altinetry.fr/.

Foster-Martinez, M. R., J. R. Lacy, M. C. Ferner, and E. A. Variano. 2018. "Wave Attenuation across a Tidal Marsh in San Francisco Bay." *Coastal Engineering* 136 (February): 26–40. https://doi.org/10.1016/j.coastaleng.2018.02.001.

Foxgrover, Amy C., Mark Marvin-DiPasquale, Bruce E. Jaffe, and Theresa A. Fregoso. 2019. "Slough Evolution and Legacy Mercury Remobilization Induced by Wetland Restoration in South San Francisco Bay." *Estuarine, Coastal and Shelf Science* 220 (August 2018): 1–12. https://doi.org/10.1016/j.ecss.2019.02.033.

Gourevitch, Jesse D., Nitin K. Singh, Josh Minot, Kristin B. Raub, Donna M. Rizzo, Beverley C. Wemple, and Taylor H. Ricketts. 2020. "Spatial Targeting of Floodplain Restoration to Equitably Mitigate Flood Risk." *Global Environmental Change* 61 (December 2019): 102050. https://doi.org/10.1016/j.gloenvcha.2020.102050.

Gutierrez, Melody. 2016. "SF Bay Protection: Measure AA Passes." *San Franciso Chronicle*, June 8, 2016. https://www.sfgate.com/politics/article/SF-Bay-protection-Measure-AA-passes-7970365.php.

Hallegatte, Stephane, Colin Green, Robert J. Nicholls, and Jan Corfee-Morlot. 2013. "Future

Flood Losses in Major Coastal Cities." *Nature Climate Change* 3 (9): 802–6. https://doi.org/10.1038/nclimate1979.

Hauer, Mathew E., Jason M. Evans, and Deepak R. Mishra. 2016. "Millions Projected to Be at Risk from Sea-Level Rise in the Continental United States." *Nature Climate Change* 6 (7): 691–95. https://doi.org/10.1038/nclimate2961.

"Hazard Reporting and Analytics (HERA)." 2017. https://www.usgs.gov/apps/hera/.

Hazus. 2021. "Hazus Flood Assessment Structure Tool." Federal Emergency Management Agency. https://github.com/nhrap-hazus/FAST.

Hersbach, Hans, Bill Bell, Paul Berrisford, Shoji Hirahara, András Horányi, Joaquín Muñoz-Sabater, Julien Nicolas, et al. 2020. "The ERA5 Global Reanalysis." *Quarterly Journal of the Royal Meteorological Society* 146 (730): 1999–2049. https://doi.org/10.1002/qj.3803.

Hirschfeld, Daniella, and Kristina E. Hill. 2017. "Choosing a Future Shoreline for the San Francisco Bay: Strategic Coastal Adaptation Insights from Cost Estimation." *Journal of Marine Science and Engineering* 5 (3): 42. https://doi.org/10.3390/jmse5030042.

Homer, Collin, Jon Dewitz, Suming Jin, George Xian, Catherine Costello, Patrick Danielson, Leila Gass, et al. 2020. "Conterminous United States Land Cover Change Patterns 2001–2016 from the 2016 National Land Cover Database." *ISPRS Journal of Photogrammetry and Remote Sensing* 162 (March): 184–99. https://doi.org/10.1016/j.isprsjprs.2020.02.019.

Knowles, N., L. Lucas, D. Stoliker, and C. Enright. 2015. "CASCADE II: Computational Assessments of Scenarios of Change for the Delta Ecosystem."

Lacy, Jessica R., Madeline R. Foster-Martinez, Rachel M. Allen, Matthew C. Ferner, and John C. Callaway. 2020. "Seasonal Variation in Sediment Delivery Across the Bay-Marsh Interface of an Estuarine Salt Marsh." *Journal of Geophysical Research: Oceans* 125 (1): 1–21. https://doi.org/10.1029/2019JC015268.

Martínez-García, Víctor, José M. Martínez-Paz, and Francisco Alcon. 2022. "The Economic Value of Flood Risk Regulation by Agroecosystems at Semiarid Areas." *Agricultural Water Management* 266 (October 2021). https://doi.org/10.1016/j.agwat.2022.107565.

Menendez, Pelayo, Inigo J Losada, Saul Torres-Ortega, and Michael W Beck. 2019. "Assessing the Effects of Using High-Quality Data and High-Resolution Models in Valuing Flood Protection Services of Mangroves." *PLoS ONE*, 1–14. https://doi.org/10.17605/OSF.IO/S5V7K.

Merkens, Jan-ludolf, Lena Reimann, Jochen Hinkel, and Athanasios T Vafeidis. 2016. "Gridded Population Projections for the Coastal Zone under the Shared Socioeconomic Pathways." *Global and Planetary Change* 145: 57–66. https://doi.org/10.1016/j.gloplacha.2016.08.009.

Meyer, David L, Edward C Townsend, and Gordon W Thayer. 1997. "Erosion Control Value of

Oyster Cultch for Intertidal Marsh." *Restoration Ecology* 5 (1): 93–99.

Narayan, Siddharth, Michael W. Beck, Paul Wilson, Christopher J. Thomas, Alexandra Guerrero, Christine C. Shepard, Borja G. Reguero, Guillermo Franco, Jane Carter Ingram, and Dania Trespalacios. 2017. "The Value of Coastal Wetlands for Flood Damage Reduction in the Northeastern USA." *Scientific Reports* 7 (1): 1–12. https://doi.org/10.1038/s41598-017-09269-z.

"National Structure Inventory." 2019. US Army Corps of Engineers. https://www.hec.usace.army.mil/confluence/nsidocs.

Nederhoff, Kees, Rohin Saleh, Babak Tehranirad, Liv Herdman, Li Erikson, Patrick L. Barnard, and Mick van der Wegen. 2021. "Drivers of Extreme Water Levels in a Large, Urban, High-Energy Coastal Estuary – A Case Study of the San Francisco Bay." *Coastal Engineering* 170 (March). https://doi.org/10.1016/j.coastaleng.2021.103984.

Parodi, Matteo U, Alessio Giardino, Ap van Dongeren, Stuart G Pearson, Jeremy D Bricker, and Ad J H M Reniers. 2020. "Uncertainties in Coastal Flood Risk Assessments in Small Island Developing States." *Natural Hazards and Earth System Sciences* 20: 2397–2414.

Pinsky, Malin L., Greg Guannel, and Katie K. Arkema. 2013. "Quantifying Wave Attenuation to Inform Coastal Habitat Conservation." *Ecosphere* 4 (8). https://doi.org/10.1890/ES13-00080.1.

Project, Goals. 2015. "The Baylands and Climate Change: What We Can Do. Baylands Ecosystem Habitat Goals Science Update 214." *BMJ (Online)*. Vol. 349. Oakland CA. https://doi.org/10.1136/bmj.g5945.

Reguero, Borja G, Michael W Beck, David N Bresch, Juliano Calil, and Imen Meliane. 2018. "Comparing the Cost Effectiveness of Nature- Based and Coastal Adaptation : A Case Study from the Gulf Coast of the United States." *PLoS ONE* 13 (4): 1–24. https://doi.org/10.17605/OSF.IO/D6R5U.

Reguero, Borja G, Curt D Storlazzi, Ann E Gibbs, James B Shope, Aaron D Cole, Kristen A Cumming, and Michael W Beck. 2021. "The Value of US Coral Reefs for Flood Risk Reduction." *Nature Sustainability* 4 (8): 688–98. https://doi.org/10.1038/s41893-021-00706-6.

Ruig, Lars T. de, Patrick L. Barnard, W. J.Wouter Botzen, Phyllis Grifman, Juliette Finzi Hart, Hans de Moel, Nick Sadrpour, and Jeroen C.J.H. Aerts. 2019. "An Economic Evaluation of Adaptation Pathways in Coastal Mega Cities: An Illustration for Los Angeles." *Science of the Total Environment* 678: 647–59. https://doi.org/10.1016/j.scitotenv.2019.04.308.

Safran, Sam, April Robinson, Julie Beagle, Marcus Klatt, Kristen Cayce, and Robin Grossinger. 2013. "A Landscape Ecology Analysis of San Francisco Bay-Delta Marsh Then (1850) and Now." Richmond, CA.

San Francisco Estuary Institute (SFEI). 1999. "Historical Baylands GIS Dataset." Richmond, CA.

San Francisco Estuary Institute (SFEI). 2016. San Francisco Bay Shore Inventory: Mapping for

Sea Level Rise Planning GIS Data. 2016. http://www.sfei.org/projects/SFBayShoreInventory.

San Francisco Estuary Institute & Aquatic Science Center (SFEI ASC). 2015. "Bay Area Aquatic Resource Inventory (BAARI) Version 2 GIS Data." 2015. http://desktop.arcgis.com/en/arcmap/10.3/manage-data/tables/calculating-area-length-and-other-geometric-properties.htm.

SFEI, and Peter Baye. 2020. "New Life for Eroding Shorelines: Beach and Marsh Edge Change in the San Francisco Estuary." Richmond, CA: San Francisco Estuary Institude.

Storlazzi, C.D., Reguero, B.G., Cumming, K.A., Cole, A.D., Shope, J.B., Gaido L., C., Viehman, T.S., Nickel, B.A., and Beck, M.W. 2021. "Rigorously Valuing the Potential Coastal Hazard Risk Reduction Provided by Coral Reef Restoration in Florida and Puerto Rico." *U.S. Geological Survey*, 1–24.

Sweet, W.V., B.D. Hamlington, R.E. Kopp, C.P. Weaver, P.L. Barnard, D. Bekaert, W. Brooks, et al. 2022. "Global and Regional Sea Level Rise Scenarios for the United States: Updated Mean Projections and Extreme Water Level Probabilities along U.S. Coastlines."

Taherkhani, Mohsen, Sean Vitousek, Patrick L. Barnard, Neil Frazer, Tiffany R. Anderson, and Charles H. Fletcher. 2020. "Sea-Level Rise Exponentially Increases Coastal Flood Frequency." *Scientific Reports* 10 (1): 1–18. https://doi.org/10.1038/s41598-020-62188-4.

Takekawa, J Y, K M Thorne, K J Buffington, K A Spragens, K M Swanson, J Z Drexler, D H Schoellhamer, C T Overton, and M L Casazza. 2013. "Final Report for Sea-Level Rise Response Modeling for San Francisco Bay Estuary Tidal Marshes." *U.S. Geological Survey Open File Report 2012-1081*, 161.

Tehranirad, Babak, Liv Herdman, Kees Nederhoff, Li Erikson, Robert Cifelli, Greg Pratt, Michael Leon, and Patrick Barnard. 2020. "Effect of Fluvial Discharges and Remote Non-Tidal Residuals on Compound Flood Forecasting in San Francisco Bay." *Water* 12 (9): 1–15. https://doi.org/10.3390/w12092481.

Thorne, Karen, Kevin Buffington, Kathleen Swanson, and John Takekawa. 2013. "Storm Episodes and Climate Change Implications for Tidal Marshes in the San Francisco Bay Estuary, California, USA." *The International Journal of Climate Change: Impacts and Responses* 4 (4): 169–90. https://doi.org/10.18848/1835-7156/cgp/v04i04/37200.

"Tides and Currents." 2021. NOAA.

Veloz, Samuel D., Nadav Nur, Leonardo Salas, Dennis Jongsomjit, Julian Wood, Diana Stralberg, and Grant Ballard. 2013. "Modeling Climate Change Impacts on Tidal Marsh Birds: Restoration and Conservation Planning in the Face of Uncertainty." *Ecosphere* 4 (4): 1–25. https://doi.org/10.1890/ES12-00341.1.

Vitousek, Sean, Patrick L Barnard, Charles H Fletcher, Neil Frazer, Li H Erikson, and Curt D Storlazzi. 2017. "Doubling of Coastal Flooding Frequency within Decades Due to Sea-Level Rise." *Nature Scientific Reports* 7: 1–9. https://doi.org/10.1038/s41598-017-

01362-7.

Zelst, Vincent T.M. van, Jasper T. Dijkstra, Bregje K. van Wesenbeeck, Dirk Eilander, Edward P. Morris, Hessel C. Winsemius, Philip J. Ward, and Mindert B. de Vries. 2021. “Cutting the Costs of Coastal Protection by Integrating Vegetation in Flood Defences.” *Nature Communications* 12 (1): 1–11. https://doi.org/10.1038/s41467-021-26887-4.

3. Exploring limitations of marsh restoration for flood reduction

Abstract

With increasing coastal hazards and ecosystem deterioration, there is interest in the U.S. and internationally in restoring wetlands to reduce coastal flooding and adapt to sea level rise. Restoring diked and drained former wetlands, such as the salt ponds in San Francisco Bay, California, represents a promising strategy but requires specific analyses to evaluate performance and effectiveness. It is widely acknowledged that wetlands can reduce flood risk, but under some conditions, marsh restoration may also amplify flooding. These effects can be controlled by the restoration design and should be included early in restoration planning. Here, we explore management scenarios in one of the salt ponds of San Mateo County, California, with both a numerical and a simplified hydrodynamic model to understand how different restoration scenarios influence water levels with sea level rise. We provide guidance on key factors for restoring coastal wetlands now and into the future.

3.1 Introduction

Wetland restoration is receiving increasing attention in the U.S. and internationally (Moraes et al. 2022) for the capacity to reduce flood water levels by attenuating wave energy and storm surge (Wamsley et al. 2010; Shepard et al. 2011; Möller et al. 2014; Smolders et al. 2015; Narayan et al. 2016; Crosby et al. 2016). Restoration of wetlands as a sea level rise (SLR) adaptation strategy has the potential to provide resilience as well as environmental and climate mitigation benefits such as fish and wildlife support and carbon sequestration (Callaway et al. 2012; Pinsky et al. 2013; Narayan et al. 2017; Foster-Martinez et al. 2018). In California, the increasing need to adapt to rising sea levels is becoming central to climate policy and action, with nature-based adaptation receiving special attention.

Within California, San Mateo County has the most projected flood exposure due to climate change, with more than 140,000 people and $50 billion of property exposed to flooding through this century (Hazard Reporting and Analytics, (HERA), 2017). Communities in California, as in many other areas, are beginning to experience these impacts and are seeking effective solutions, increasingly through use of nature-based solutions. For example, in 2016, Bay Area voters passed Measure AA, which uses a $12 per year parcel tax to restore wetlands to prepare for climate change (San Francisco Bay Restoration Authority 2017). Coastal development has altered or removed up to 90% of the Bay's historical tidal wetlands (Safran et al. 2013) and marsh restoration has emerged as a unifying regional management objective in the past several decades, particularly the restoration of salt ponds (Brew and Williams 2010; Callaway et al. 2007; 2011; Foxgrover et al. 2019). Restoration efforts in San Francisco Bay constitute the most ambitious wetland restoration on the U.S. West Coast. Wetland restoration can be effective in reducing flood risk, but recent work has also shown that restoration of diked and drained former wetlands could amplify flood levels and overtop levee crests in some instances (Taylor-Burns et al., in review). Therefore, exploring how marsh restoration in diked and drained former wetlands like the San Francisco Bay salt ponds can be strategically executed to maintain community safety is a necessary next step.

Here, we explore how management scenarios in one of the salt ponds of San Mateo County could influence flooding in the future and provide guidance on the factors that should be considered when restoring diked and drained former wetlands. We combine numerical modeling with a simplified model which is applicable in other contexts to provide guidance on how restoration in hydraulically altered ponds influences water levels with sea level rise.

3.2 Methods

3.2.1 Study site

The Cargill salt ponds in Redwood City (Figure 3.1) comprise a 1,400-acre area, formerly connected to the bay and diked off to facilitate evaporation for salt production in 1902. These ponds are some of the remaining holdings of the Cargill Corporation, which sold 15,000 acres of salt ponds to the state and federal government in 2003, launching the South Bay Salt Pond Restoration Project. In 2009, the Cargill Corporation proposed a plan to develop the area with 12,000 housing units as well as commercial buildings. Environmental groups argued the Clean Water Act protects the ponds from development, and EPA rulings have gone back and forth on this issue over three presidential administrations. While development is unlikely, the future of the ponds remains uncertain (Ashley and Didion 2021; Handa 2021; Toledo 2021). External levees separate the ponds from the San Francisco Bay, and internal levees divide the area into numerous separate basins (Figure 3.1A). The ponds are mostly unvegetated, and even if they were re-connected to the bay, their elevation is too low relative to the tidal prism of the area to support a full range of marsh vegetation. Channelization that is typical of healthy marshes is no longer present in the ponds due to decades of industrial salt production.

3.2.2 Management interventions

To understand how pond management influences flood depth and extent, simulations with existing salt ponds and potential interventions were compared under various sea level and storm conditions, including: 0, 0.5, and 1.0 m of SLR, within the range of most updated

intermediate estimates for California by 2100 (Sweet et al. 2022), along with annual, 20-year and 100-year storm conditions. Several management interventions were simulated, each identified by Beagle et al. (2019). These include polder management, horizontal levees, and marsh restoration (Figure 3.1B). We used satellite and historical photography, as well as conversations with stakeholders, to determine locations for the levee breaches, which are made across historical channels (Figure 3.2). The sediment nourishment brought mean elevation of the ponds to +1 m NAVD88 which is characteristic of healthy marshes in the region (Takekawa et al. 2013).

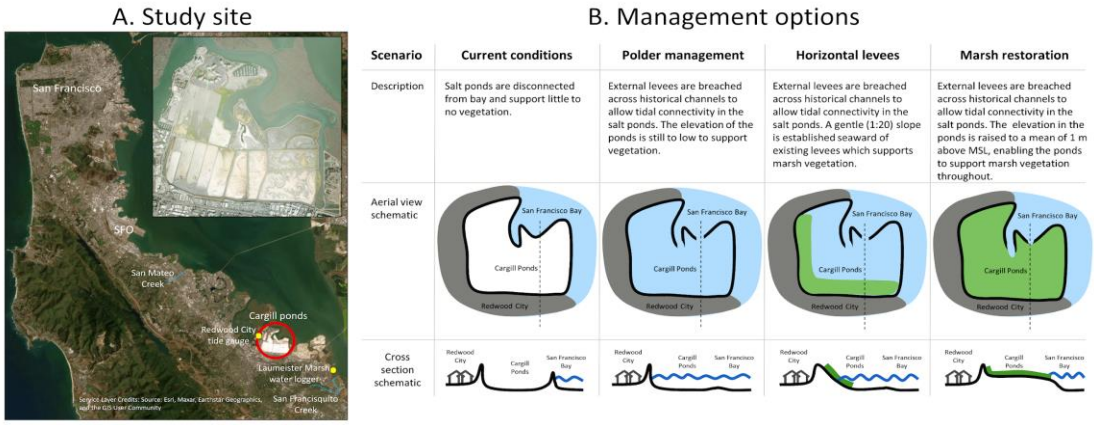

Figure 3.1 Depiction of the study site (A) and of the management options simulated (B).

3.2.3 Numerical modeling

To assess flood impacts of habitat restoration, we used Delft3D Flexible Mesh (Delft3D FM, Delft3D Flexible Mesh 2020.04, Deltares, 2022) and Simulating WAves Nearshore (SWAN, Booij et al., 1999) through a two-way coupling. Delft3D FM solves the shallow-water equations with a finite volume method on staggered unstructured grids in one-, two-, and three-dimensional schematizations. We ran the model in a depth averaged two-dimensional-horizontal schematization. SWAN is a third-generation, phase-averaged numerical model that

simulates wave propagation from deep to shallow waters using the energy balance and action balance equations. When coupling the flow and wave models, wave-current interactions are simulated, resulting in changes in wave setup, current refraction, bottom friction, forcing, turbulence, and bed shear stress. The wave energy spectrum model does not resolve individual waves. Thus, this model accounts for tides, storm surge, river discharge, wave setup, and SLR, but it lacks representation of swash processes, which are critical for assessing wave-structure interactions and require a phase-resolving wave model.

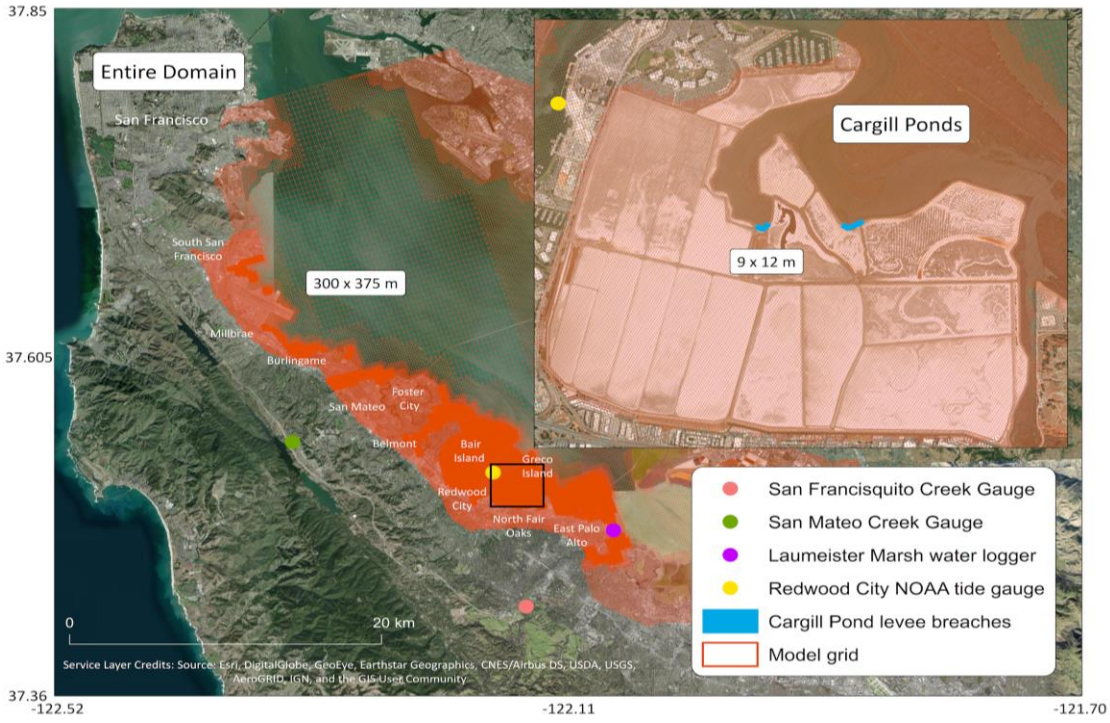

Figure 3.2 The numerical model mesh is shown in red. The yellow and purple circles show locations of model calibration and validation with sea level observations. The pink and green circles show locations of creek gauge data. The blue rectangles show locations of levee breaches in the Cargill Ponds. The text boxes in the mesh denote the grid resolution of the mesh in its lowest and highest resolution, which are the middle of the bay and in existing and potential San Mateo County marshes, respectively.

The numerical domain for the model in San Mateo County was adapted from Tehranirad et al. (2020), and the approach was based on the Coastal Storm Modeling System (Barnard et al.

2014; 2019). The grid resolution in the Cargill Ponds (Figure 3.2) and in other existing and potential marsh habitat was ~10 m, capturing sinuous channels and the complex bathymetry of the marshes. Bathymetry was derived from a LEAN-corrected 5-m horizontal resolution digital elevation model, used above -1 m NAVD88 (Buffington & Thorne, 2018) and from a 10-m horizontal resolution model, used below -1 m NAVD88 (Fregoso et al., 2017). Satellite-derived land cover data from the National Land Cover Database (Homer et al. 2020) was used to determine land cover type. Open water Manning's friction values were set to 0.02, following Tehranirad et al. (2020), and vegetation was represented implicitly with a Manning's friction coefficient of 0.03, 0.035, and 0.04 for low, transition, and high marsh zones, respectively, in the Delft3D model, following values suggested by Bunya et al. (2010) and DHI (2013). Marsh habitat locations were determined by tidal vegetation location in the Bay Area Aquatic Resources Inventory (San Francisco Estuary Institute & Aquatic Science Center, 2015). As marsh vegetation is sensitive to flooding periods (Takekawa et al. 2013), the three different marsh zones were determined based on elevation relative to mean sea level (MSL) and mean higher high water (MHHW), using z* as a metric, following Beagle et al. (2019): $z* = \frac{land\ surface\ elevation - MSL}{MHHW - MSL}$. High marsh was assumed to exist in locations with a z* value between 1.02 and 1.38; transition marsh was assumed to exist in locations with a z* value between 0.75 and 1.02; low marsh was assumed to exist in locations with a z* value between -0.14 and 0.75 (Beagle et al. 2019). MHHW and MSL were determined from Beagle et al. (2019) and were assumed to be constant across the study region, neglecting the < 20 cm variation in MHHW across the region.

MSL was assumed to be 1.00 m NAVD88 and MHHW was assumed to be 2.12 m NAVD88. Flood control infrastructure was included as a sub-grid feature. Location of flood control infrastructure was determined from the San Francisco Estuary Institute's Bay Shore Inventory (San Francisco Estuary Institute, 2016), with height of flood control infrastructure determined from the highest resolution DEM available (Danielson et al. 2016). Storm water levels and wind and pressure time series were derived from the Coastal Storm Modeling System (CoSMoS, Barnard et al., 2014; 2019) and were developed from 21st century total water level proxy time-series based on CMIP5 global climate model winds, sea level pressures and sea surface temperatures (Taylor et al. 2012). Water levels from this time series were ranked to extract mean, annual, 20-yr, and 100-year events. Downscaled 21st century wind and pressure for the associated future dates were used to force local models in which storms were run in combination with plausible 21st century increases in sea level to incorporate non-linear interactions between water levels and waves. Storms simulated in Barnard et al. (2019) are 50 hours in duration, which is not long enough to isolate the non-tidal residual from tides. Thus, data from the tide gauge closest to the open boundary, located in Alameda (NOAA, 2021), were appended before and after the storm water level time series at the open boundary, and a low-pass filter was used to derive the non-tidal residual. The low-pass filter caused the storm water levels to become non-progressive in the second day of the simulation. Thus, water levels from the first day of the simulation were used to determine maximum flood depth during the storms.

3.2.4 Simplified inlet-pond model

To characterize the effects of pond management on water levels, we also use a simplified model that is based on resolving the shallow water equations in one dimension, which can be applied to other areas without computational effort. For an inlet-pond problem, as represented in Figure 3.3, the sea level variations in the pond are defined by Bruun (1978): flow momentum and continuity, the ocean tide as a forcing function, and the relationship between the bed shear stress and the flow velocity in terms of a friction factor representing boundary resistance to flow.

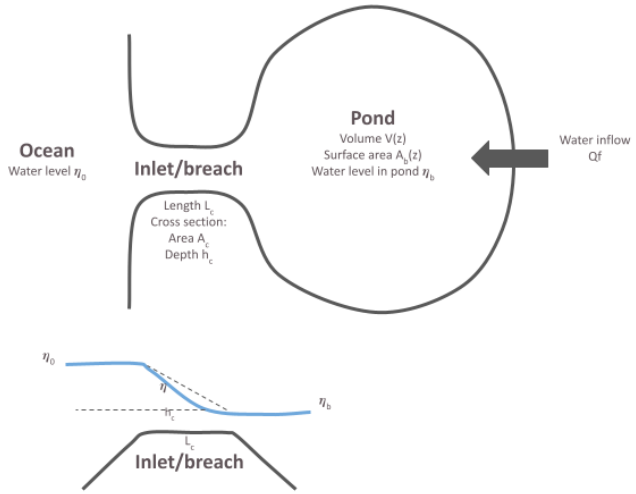

Figure 3.3 Idealized inlet-pond system representation (upper sketch) and head losses in an idealized inlet channel or breaching (lower sketch). Adapted from Bruun (1978).

The inlet (i.e., levee breach) is an open channel with a certain cross section, defined by area (A_c), which depends on the depth (h_c). The tide represents the boundary condition on one end of the channel, while the water level in the pond is the other. At the channel, the one-dimensional shallow water momentum equation determines that: $\frac{\partial \bar{u}}{\partial t} + u\frac{\partial \bar{u}}{\partial x} + g\frac{\partial \eta}{\partial x} + f\frac{\bar{u}|\bar{u}|}{8h_c} = 0$, where $\bar{u}$ is the depth-averaged flow velocity in the channel, η is the tidal

elevation, and f is the Darcy Weisbach friction factor for dissipation and is a function of the Chezy roughness coefficient, C, with $f = 8g/C^2$. Integrating over the length of the channel, L_c, and assuming no variations in u over the length of the channel, the equation can be written as:

$$g(\eta_b - \eta_0) + L_c \frac{\partial \bar{u}}{\partial t} + F \frac{\bar{u}|\bar{u}|}{2} = 0 \qquad \text{(Eq 3.1)}$$

where F represents losses at entrance, through the channel (entrance and exit loss, head loss due to friction and head loss due to inertia). F can be expressed as $F = K_{entrance} + K_{exit} + \frac{2gL}{C^2 h}$, where $K_{entrance}$ and K_{exit} are entrance and exit losses, respectively, and $\frac{2gL}{C^2 h}$ represents losses due to friction. The continuity equation imposes a relationship between the current speed and the water level in the pond which can be written as: $\frac{dV}{dt} = Q_c - Q_f = \bar{u}(t) \cdot A_c(\eta_0) - Q_f$, where Q_f is the rate of freshwater inflow, which we will assume is 0. Since the volume at the tidal inlet at any moment is $\mathrm{V} = \eta_b A_b$, the velocity at the channel is shown in equation 3.2, where A_b is the surface area of the pond and A_c is the area of the inlet or breach.

$$\bar{u} = \frac{A_b(\eta)}{A_c(\eta_0)} \frac{\partial \eta_b}{\partial t} \qquad \text{(Eq. 3.2)}$$

Equations 3.1 and 3.2 are second order differential equations that can be solved at each time step, considering that $A_b(\eta)$ is a function of sea level at the pond and may present different area laws.

3.2.5 Hypothetical case to assess the effects of sea level rise on wetland restoration management

To understand the effects of SLR and wetland management scenarios over storm tides, we simulate hypothetical pond cases: a pond with vertical walls (no change in A_b with η); a linear law; and two non-linear area laws. The full area of the pond for this example is assumed to 5 million m^2, approximately the area of the Cargill Ponds. The ocean forcing time series was extracted from results of the numerical model described above. The storm tide in pond is calculated to understand the effects of interventions, in support of the numerical simulations.

3.3 Results

3.3.1 Numerical results

In storm simulations where the storm overtops the external levees of the ponds (1 m SLR) and where the storm does not flood the ponds even with levee breaches (0 m SLR scenario), managed levee breaches have limited effect on peak water levels. However, with 0.5 m of SLR, all management interventions cause higher water levels in the ponds due to water entering the ponds through managed breaches of the levee system. While polder management only entails managed breaching of the salt ponds, implementing horizontal levees and marsh restoration require adding sediment to the ponds to raise elevation and support marsh vegetation. Sediment nourishment decreases volume of the ponds which can cause higher water levels (Figure 3.4). This is shown by the colored lines in the top row, which show the difference between water levels in the existing pond configuration and in the management alternative. The colored lines reach the highest values in the third column,

meaning this management alternative increases water levels most. The third column represents the marsh restoration management option and involves adding the most sediment to the ponds, decreasing pond volume by the greatest amount. Sediment nourishment can also cause an earlier peak water level during the storms (Figure 3.4). This earlier peak is shown by the colored dots in the bottom row, which show the timing of peak water level between the existing pond configuration and in the management alternative. The colored dots are furthest below the 1:1 diagonal black line in the third column, meaning this management causes peak water levels to happen earliest. Wider levee breaches can also cause higher water levels (Figure 3.4). This pattern is shown in the right-most panel, which shows the difference in water levels in the marsh restoration scenario and the existing pond configuration with three different levee breach sizes. Large levee breaches, shown by the large dashed lines, increase water levels in the ponds most.

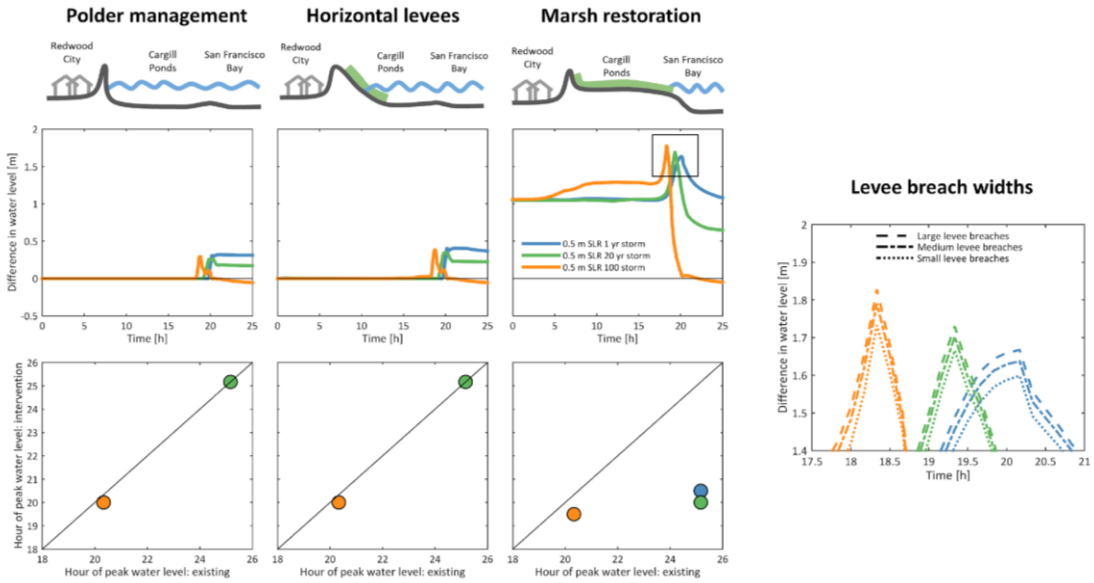

Figure 3.4 Differences between water levels between three different management interventions and the existing salt ponds (top panels), and with three different levee breach widths (right panel); and differences in timing of peak water levels with existing salt pond (bottom panels). The blue lines and

dots show results from 0.5 m SLR and an annual storm. The green lines and dots show results from 0.5 m SLR and a 20-year storm. The orange lines and dots show results from 0.5 m SLR and a 100-year storm. The right panel corresponds to the black square shown in the marsh restoration water level subplot. The top row shows that marsh restoration (right column) increases water levels most, shown by the highest peaks in the right-most subplot in the top row. The bottom row shows that marsh restoration (right column) causes peak water levels to happen earliest, shown by the colored dots being furthest below the diagonal black line. The right panel shows that larger levee breaches cause water levels in the ponds to be higher, shown by the large dashed lines reaching higher values than the medium dashed lines or the dotted lines.

Depending on levee height behind the ponds, higher water levels and earlier peak water levels in the ponds can increase flood risk. For example, for 0.5 m SLR and a 100-year storm, in comparison to the existing ponds, marsh restoration causes greater flooding over the levee at the back of the ponds, resulting in increased flood risk to communities behind the ponds. This increase in risk is shown by increased flood extent at 20:00:00 and 20:50:00 behind the red line which signifies the levee separating the ponds from industrial and residential development (Figure 3.5).

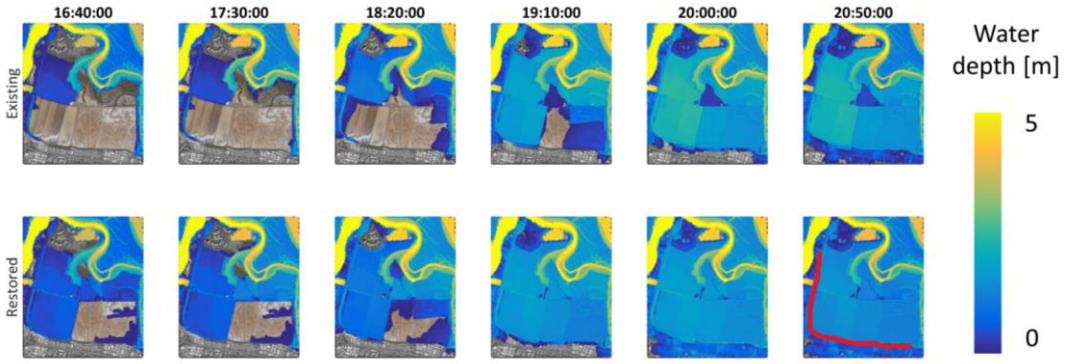

Figure 3.5 Flood extents and depths in the Cargill Ponds during the 0.5 m SLR and 100-year storm simulation, with the existing ponds on the top and the marsh restoration scenario on the bottom. Each column shows the modeled flood plain at a 50-minute time step, which is shown in the column title. In the marsh restoration scenario (bottom row), the ponds fill more quickly and the levee behind the ponds overtops earlier compared to the existing marsh scenario, resulting in increased flood risk. This can be seen by differences between the existing and restored flood plains at 20:00:00 and 20:50:00. At both of these model time steps, the restoration scenario results in increased flooding behind the red line which represents the levee separating the ponds from residential and industrial development.

3.3.2 Simplified model results

The balance of frictional drag force in the channel and gravitational force due to a difference in water levels between the pond and the channel drives water levels in the system (Figure S.3.1). Results from the simplified shallow water equation model illustrate that water levels in the tidal pond are dependent on the offshore water levels, the bathymetry within the tidal pond, and the width of inlet or levee breach (Figure 3.6).

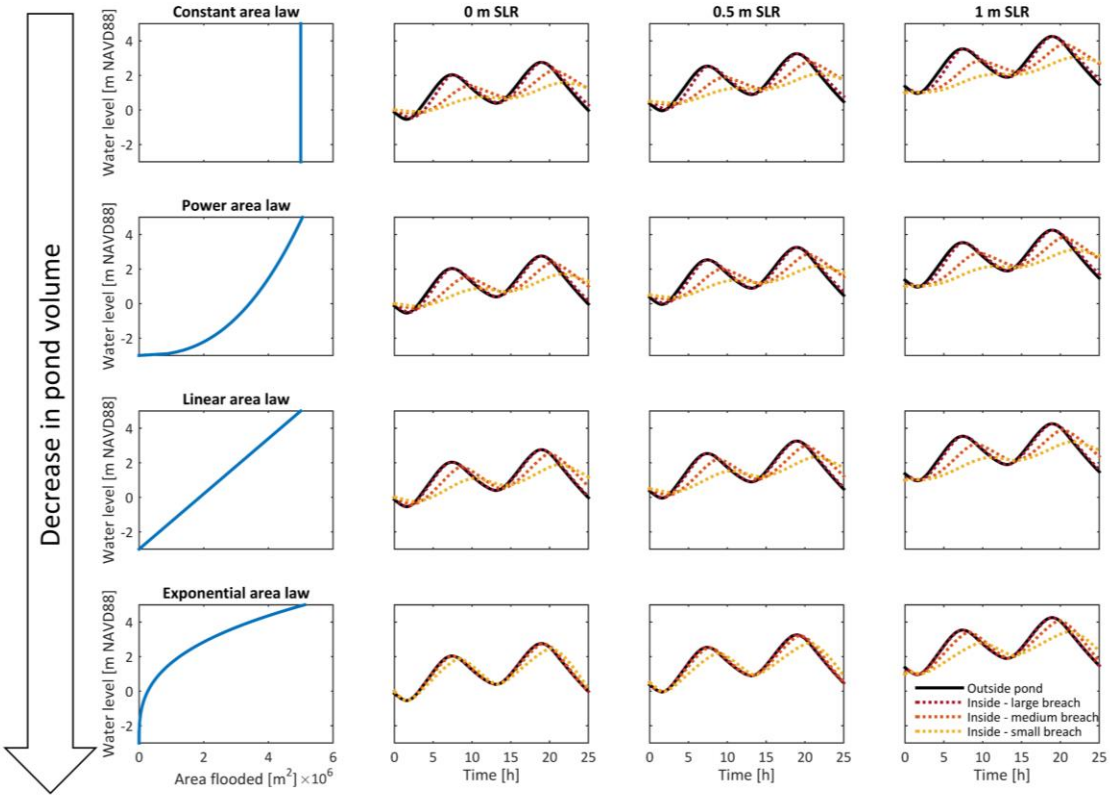

Figure 3.6 Water level and associated flooded surface area within the tidal pond in column 1. Modeled water levels inside and outside the tidal pond are shown in columns 2 through 4, with varying sea levels in each column and varying levee breach widths in each color.

Bathymetry within the pond influences the inundated surface area at each water level, determining how quickly the pond fills. The width of the levee breach also influences the flow into and out of the pond. A comparison between two different area laws is shown in Figure 3.7, illustrating the influence of bathymetry alteration and levee breaches width on water levels in the pond. Reducing the volume of the pond causes tidal amplification and a phase shift to earlier peak water levels. Wider levee breaches cause higher water levels as well. With SLR, the constant area and non-constant areas converge, causing water levels to become increasingly similar, while tidal amplification and phase lag decrease.

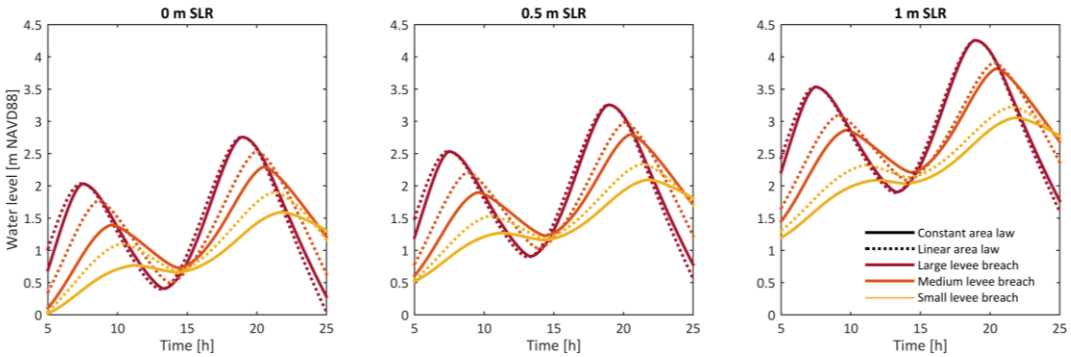

Figure 3.7 Water level inside the pond under three sea level rise scenarios (panels) with three breach widths (colors) and two area laws (line types).

3.4. Conclusions

These simulations demonstrate that flooding in diked and drained wetlands can be amplified depending on the restoration scenario and the wetland configuration. The width of the inlet, and the storage volume of the wetland are key drivers of water levels and adaptation benefits to SLR. Both factors can be controlled in the restoration design but are rarely considered when planning restorations. The simplified model can be a useful tool to inform strategies for wetland restoration. We provide several general conclusions:

- Narrow breach widths provide more flood mitigation, but also more restriction for hydraulic flow in the marsh, which will likely have ecological impacts (Figure 3.4, Figure 3.6, and Figure 3.7). Tradeoffs should be considered between flood mitigation, SLR adaptation, and habitat quality.

- Reducing the volume of the pond can cause amplification of the storm tide and a phase shift to earlier peak water levels (Figure 3.4, Figure 3.6, and Figure 3.7). The way a restoration is designed can affect the volume of water it can hold and may have flood risk implications.

- Shifting the tidal prism with SLR will also influence the volume of storm water a restoration can hold and can have flood risk implications. It will be necessary to consider tidal amplification with SLR to maintain community safety where restoration is adjacent to levees or berms that protect developed land.

References

Ashley, Dan, and Tim Didion. 2021. "Housing or Wetlands? Fight Continues over Future of Bay Area Salt Ponds." *ABC 7 News*, March 11, 2021. https://abc7news.com/salt-ponds-cargill-redwood-city-marsh/10404796/.

Barnard, Patrick L., Maarten van Ormondt, Li H. Erikson, Jodi Eshleman, Cheryl Hapke, Peter Ruggiero, Peter N. Adams, and Amy C. Foxgrover. 2014. "Development of the Coastal Storm Modeling System (CoSMoS) for Predicting the Impact of Storms on High-Energy, Active-Margin Coasts." *Natural Hazards* 74 (2): 1095–1125. https://doi.org/10.1007/s11069-014-1236-y.

Barnard, Patrick L., Li H. Erikson, Amy C. Foxgrover, Juliette A. Finzi Hart, Patrick Limber, Andrea C. O'Neill, Maarten Van Ormondt, et al. 2019. "Dynamic Flood Modeling Essential to Assess the Coastal Impacts of Climate Change." *Nature Scientific Reports* 9. https://doi.org/10.1038/s41598-019-40742-z.

Beagle, Julie, Jeremy Lowe, Katie McKnight, Sam Safran, Laura Tam, and Sarah Jo Szambelan. 2019. "San Francisco Bay Shoreline Adapation Atlas: Working with Nature to Plan for Sea Level Rise Using Operational Landscape Units."

Booij, N., R. C. Ris, and L. H. Holthuijsen. 1999. “A Third-Generation Wave Model for Coastal Regions 1. Model Description and Validation.” *Journal of Geophysical Research: Oceans* 104 (C4): 7649–66. https://doi.org/10.1029/98JC02622.

Brew, David S., and Philip B. Williams. 2010. “Predicting the Impact of Large-Scale Tidal Wetland Restoration on Morphodynamics and Habitat Evolution in South San Francisco Bay, California.” *Journal of Coastal Research* 265 (265): 912–24. https://doi.org/10.2112/08-1174.1.

Bruun, Per Moller. 1978. *Stability of Tidal Inlets*.

Bunya, S., J. C. Dietrich, J. J. Westerink, B. A. Ebersole, J. M. Smith, J. H. Atkinson, R. Jensen, et al. 2010. “A High-Resolution Coupled Riverine Flow, Tide, Wind, Wind Wave, and Storm Surge Model for Southern Louisiana and Mississippi. Part I: Model Development and Validation.” *Monthly Weather Review* 138 (2): 345–77. https://doi.org/10.1175/2009MWR2906.1.

Callaway, John C., Evyan L. Borgnis, R. Eugene Turner, and Charles S. Milan. 2012. “Carbon Sequestration and Sediment Accretion in San Francisco Bay Tidal Wetlands.” *Estuaries and Coasts* 35 (5): 1163–81. https://doi.org/10.1007/s12237-012-9508-9.

Callaway, John C., V. Thomas Parker, Michael C. Vasey, Lisa M. Schile, and Ellen R. Herbert. 2011. “Tidal Wetland Restoration in San Francisco Bay: History and Current Issues.” *San Francisco Estuary and Watershed Science* 9 (3). https://doi.org/10.15447/sfews.2011v9iss3art2.

Callaway, John C., V. Thomas Parker, Michael C. Vasey, and Lisa M. Schile. 2007. “Emerging Issues for the Restoration of Tidal Marsh Ecosystems in the Context of Predicted Climate Change.” *Madroño* 54 (3): 234–48. https://doi.org/10.3120/0024-9637(2007)54[234:eiftro]2.0.co;2.

Crosby, Sarah C., Dov F. Sax, Megan E. Palmer, Harriet S. Booth, Linda A. Deegan, Mark D. Bertness, and Heather M. Leslie. 2016. “Salt Marsh Persistence Is Threatened by Predicted Sea-Level Rise.” *Estuarine, Coastal and Shelf Science* 181: 93–99. https://doi.org/10.1016/j.ecss.2016.08.018.

Danielson, Jeffrey J., Sandra K. Poppenga, John C. Brock, Gayla A. Evans, Dean J. Tyler, Dean B. Gesch, Cindy A. Thatcher, and John A. Baras. 2016. “Topobathymetric Elevation Model Development Using a New Methodology : Coastal National Elevation Database.” *Journal of Coastal Research*, no. 76. https://doi.org/10.2112/SI76-008.

“Delft3D Flexible Mesh.” 2022. Deltares. https://www.deltares.nl/en/software/delft3d-flexible-mesh-suite/.

DHI. 2013. “Regional Coastal Hazard Modeling Study for South San Francisco Bay.”

Foster-Martinez, M. R., J. R. Lacy, M. C. Ferner, and E. A. Variano. 2018. “Wave Attenuation across a Tidal Marsh in San Francisco Bay.” *Coastal Engineering* 136 (February): 26–40. https://doi.org/10.1016/j.coastaleng.2018.02.001.

Foxgrover, Amy C., Mark Marvin-DiPasquale, Bruce E. Jaffe, and Theresa A. Fregoso. 2019. "Slough Evolution and Legacy Mercury Remobilization Induced by Wetland Restoration in South San Francisco Bay." *Estuarine, Coastal and Shelf Science* 220 (August 2018): 1–12. https://doi.org/10.1016/j.ecss.2019.02.033.

Handa, Robert. 2021. "Redwood City Salt Ponds Likely Safe From Development – at Least for Now." *NBC Bay Area*, April 23, 2021. https://www.nbcbayarea.com/news/local/climate-in-crisis/redwood-city-salt-ponds-likely-safe-from-development-at-least-for-now/2526894/.

"Hazard Reporting and Analytics (HERA)." 2017. https://www.usgs.gov/apps/hera/.

Homer, Collin, Jon Dewitz, Suming Jin, George Xian, Catherine Costello, Patrick Danielson, Leila Gass, et al. 2020. "Conterminous United States Land Cover Change Patterns 2001–2016 from the 2016 National Land Cover Database." *ISPRS Journal of Photogrammetry and Remote Sensing* 162 (March): 184–99. https://doi.org/10.1016/j.isprsjprs.2020.02.019.

Möller, Iris, Matthias Kudella, Franziska Rupprecht, Tom Spencer, Paul Maike, Bregje K. van Wesenbeeck, Guido Wolters, et al. 2014. "Wave Attenuation over Coastal Salt Marshes under Storm Surge Conditions." *Nature Geosciences* 7: 727–31.

Moraes, Roberta P.L., Borja G. Reguero, Inés Mazarrasa, Max Ricker, and José A. Juanes. 2022. "Nature-Based Solutions in Coastal and Estuarine Areas of Europe." *Frontiers in Environmental Science* 10 (June): 1–12. https://doi.org/10.3389/fenvs.2022.829526.

Narayan, Siddharth, Michael W. Beck, Borja G. Reguero, Iñigo J. Losada, Bregje Van Wesenbeeck, Nigel Pontee, James N. Sanchirico, Jane Carter Ingram, Glenn Marie Lange, and Kelly A. Burks-Copes. 2016. "The Effectiveness, Costs and Coastal Protection Benefits of Natural and Nature-Based Defences." *PLoS ONE* 11 (5): 1–17. https://doi.org/10.1371/journal.pone.0154735.

Narayan, Siddharth, Michael W. Beck, Paul Wilson, Christopher J. Thomas, Alexandra Guerrero, Christine C. Shepard, Borja G. Reguero, Guillermo Franco, Jane Carter Ingram, and Dania Trespalacios. 2017. "The Value of Coastal Wetlands for Flood Damage Reduction in the Northeastern USA." *Scientific Reports* 7 (1): 1–12. https://doi.org/10.1038/s41598-017-09269-z.

Pinsky, Malin L., Greg Guannel, and Katie K. Arkema. 2013. "Quantifying Wave Attenuation to Inform Coastal Habitat Conservation." *Ecosphere* 4 (8). https://doi.org/10.1890/ES13-00080.1.

Safran, Sam, April Robinson, Julie Beagle, Marcus Klatt, Kristen Cayce, and Robin Grossinger. 2013. "A Landscape Ecology Analysis of San Francisco Bay-Delta Marsh Then (1850) and Now." Richmond, CA.

San Francisco Bay Restoration Authority. 2017. "Grants Funded by Measure AA : The San Francisco Bay Clean Water , Pollution Prevention and Habitat Restoration Measure June 2017," no. June. https://sta.ca.gov/wp-content/uploads/STA/Groups/STA

Board/Meeting Agendas/2017/09-13-17/11.Ba_Att A Measure AA.pdf.

San Francisco Estuary Institute (SFEI). 2016. “No Title.” San Francisco Bay Shore Inventory: Mapping for Sea Level Rise Planning GIS Data. 2016. http://www.sfei.org/projects/SFBayShoreInventory.

San Francisco Estuary Institute & Aquatic Science Center (SFEI ASC). 2015. “Bay Area Aquatic Resource Inventory (BAARI) Version 2 GIS Data.” 2015. http://desktop.arcgis.com/en/arcmap/10.3/manage-data/tables/calculating-area-length-and-other-geometric-properties.htm.

Shepard, Christine C., Caitlin M. Crain, and Michael W. Beck. 2011. “The Protective Role of Coastal Marshes: A Systematic Review and Meta-Analysis.” *PLoS ONE* 6 (11). https://doi.org/10.1371/journal.pone.0027374.

Smolders, S., Y. Plancke, S. Ides, P. Meire, and S. Temmerman. 2015. “Role of Intertidal Wetlands for Tidal and Storm Tide Attenuation along a Confined Estuary: A Model Study.” *Natural Hazards and Earth System Sciences* 15: 1659–75. https://doi.org/10.5194/nhess-15-1659-2015.

Sweet, W. V., B. D. Hamlington, R. E. Kopp, C. P. Weaver, P. L. Barnard, D. Bekaert, W. Brooks, et al. 2022. “Global and Regional Sea Level Rise Scenarios for the United States: Updated Mean Projections and Extreme Water Level Probabilities along U.S. Coastlines.”

Takekawa, J. Y., K. M. Thorne, K. J. Buffington, K. A. Spragens, K. M. Swanson, J. Z. Drexler, D. H. Schoellhamer, C. T. Overton, and M. L. Casazza. 2013. “Final Report for Sea-Level Rise Response Modeling for San Francisco Bay Estuary Tidal Marshes.” *U.S. Geological Survey Open File Report 2012-1081*, 161.

Taylor-Burns, Rae, Christopher Lowrie, Babak Tehranirad, Jeremy Lowe, Li Erikson, Patrick L. Barnard, Borja Reguero, and Michael W. Beck. “Quantifying the Value of Marsh Restoration for Climate Adaptation in an Urban Estuary.” In review at *Scientific Reports*.

Taylor, Karl E., Ronald J. Stouffer, and Gerald A. Meehl. 2012. “An Overview of CMIP5 and the Experiment Design.” *Bulletin of the American Meteorological Society* 93 (4): 485–98. https://doi.org/10.1175/BAMS-D-11-00094.1.

Tehranirad, Babak, Liv Herdman, Kees Nederhoff, Li Erikson, Robert Cifelli, Greg Pratt, Michael Leon, and Patrick L. Barnard. 2020. “Effect of Fluvial Discharges and Remote Non-Tidal Residuals on Compound Flood Forecasting in San Francisco Bay.” *Water* 12 (9): 1–15. https://doi.org/10.3390/w12092481.

“Tides and Currents.” 2021. NOAA.

Toledo, Aldo. 2021. “Cargill Drops Fight to Build 12,000 Homes on Redwood City Salt Ponds.” *The Mercury News*, April 15, 2021. https://www.mercurynews.com/2021/04/15/cargill-drops-fight-to-build-12000-homes-on-redwood-city-salt-ponds/.

Wamsley, Ty V., Mary A. Cialone, Jane M. Smith, John H. Atkinson, and Julie D. Rosati. 2010.

"The Potential of Wetlands in Reducing Storm Surge." *Ocean Engineering* 37 (1): 59–68. https://doi.org/10.1016/j.oceaneng.2009.07.018.

4. Horizonal levees extend the lifespan of a regional levee system

Abstract

Nature-based solutions are receiving increasing attention as a cost-effective climate adaptation strategy. In estuarine areas, horizontal (green) levees can offer a hybrid solution to reinforce traditional levees in preparation for the projected impacts of sea level rise (SLR) while simultaneously providing new intertidal wetland habitat. Horizontal levees comprise of a gently sloping vegetated area fronting a buried levee. The plants on the horizontal levee can provide wave attenuation benefits as well as habitat benefits. We use a hydrodynamic model, XBeach non-hydrostatic (XB-NH), to assess the stability and sustainability of existing levees and determine how hybrid nature-based climate adaptation measures can reduce the risk of levee failure in San Francisco Bay. Here, we implement various horizontal levee configurations in the numerical model under a variety of sea level and wave conditions and compare overtopping rates of the existing levee and of the horizontal levee configuration to assess how horizontal levees perform in reducing flood risk, both with present day conditions and with SLR. Results show that the risk of levee failure can be reduced by up to 30% with horizontal levels. Further, the analysis provides insight to horizontal levee design considerations and a methodological approach to adapt levees to prepare for SLR in urban estuaries.

4.1 Introduction

Human caused climate change is raising sea levels and increasing the threat of coastal flooding globally, forcing coastal communities to develop adaptation strategies to mitigate future hazard risk. Traditional engineering solutions such as seawalls and levees have long been used to reduce flood risk. However, as mounting evidence demonstrates that coastal

habitats can play an important role in attenuating waves and reducing storm surge (e.g Maza et al. 2013; Narayan et al. 2017; Reguero et al. 2021), management interest is shifting towards nature-based climate adaptation (Reguero et al. 2018; Olander et al. 2022).

Management practices across San Francisco Bay ("the Bay"), a densely urbanized estuary in California, USA, exemplify this shift. The Bay relies heavily on gray infrastructure for flood protection today, with nearly 70% of the present-day Bay shoreline protected by levees and berms (Hirschfeld and Hill 2017). This regional levee system currently provides baseline flood protection for existing conditions, but without significant investment in existing infrastructure, this aging levee system will not provide sufficient protection for future SLR (BCDC et al. 2020). Projections for the 21st century estimate that two-thirds of the population and property at risk of exposure to SLR- and storm-driven flooding across California are focused along the Bay shoreline, assuming no levee failures or additional restoration activities (Barnard et al., 2019). To protect the 400,000 people and $150 billion in property at risk in the Bay, a gray infrastructure investment of ~$335 billion would be required (Hirschfeld and Hill, 2017). Highlighting the shift towards using nature for climate adaptation, in 2016 Bay Area voters passed Measure AA, which uses a $12 per year parcel tax to restore wetlands to prepare for climate change (San Francisco Bay Restoration Authority 2017), and over the past decade research and studies exploring how the region can incorporate nature-based coastal adaptation have proliferated (Foster-Martinez et al. 2018; Beagle et al. 2019; Foxgrover et al. 2019; Taylor Burns et al. 2023).

Previous research suggests that vegetation can play an important role in decreasing the required height and associated cost of levees and that vegetation could reduce levee investment cost by $320 billion on a global scale (van Zelst et al. 2021). However, in highly altered urban estuaries such as San Francisco Bay, where large areas of marsh habitat have already been reclaimed, developed, and degraded, large-scale habitat restoration options may be limited due to lack of accommodation space. An alternative approach to large-scale habitat restoration is the employment of vegetation in front of levees through the use of horizontal levees (Figure 4.1). Horizontal levees consist of implementing a levee set back from the coastline with a wide and gently sloping expanse of vegetated habitat between the water and the levee, allowing wave attenuation from plants to reduce the probability of wave-driven levee overtopping.

Horizontal levees have been identified as a potential approach in San Francisco Bay based on ecological and geomorphological factors (Beagle et al. 2019). Recent work shows that vegetation can reduce risk of wave-overtopping on levees in the Bay (van Zelst et al. 2021; Taylor-Burns et al. 2023), and regional studies identify suitable locations for horizontal levees in San Francisco Bay (Beagle et al. 2019). However, studies have lacked characterization of wave-resolved overtopping risk under present and future hydrodynamic forcing conditions. Further, how the design of horizontal levees may influence risk of levee failure remains unquantified.

Here, we use a joint-probability analysis paired with a process-based numerical model, XBeach non-hydrostatic (XB-NH, de Ridder et al. 2020), to assess how horizontal levees can reduce the risk of wave-induced levee overtopping in San Francisco Bay. We test several

horizontal levee designs across suitable regions of the Bay shore to quantify the capacity of this nature-based adaptation approach to reduce the risk of levee overtopping. Results illustrate that low-probability combinations of waves and water levels (e.g., the present-day 100-year storm) will quickly become more frequent as sea levels rise, pushing existing flood-control infrastructure to its limit and highlighting the urgent need for adaptation. The results demonstrate that 1:100 sloped horizontal levees can reduce risk of overtopping that exceeds the structural design of the levee by up to 7% with present sea level. With 0.5 m and 1 m of SLR, this value increases to 22% and 30% respectively. While the greater risk reduction values occur with more gradually sloping horizontal levees, even 1:20 sloped horizontal levees can reduce risk of structural exceedance by up to 3%, 8%, and 20%, with 0, 0.5 and 1 m of SLR, respectively. These results demonstrate that this hybrid nature-based climate adaptation approach can be a part of the solution in adapting to rising sea levels.

4.2 Methods

4.2.1 Study site

Within California, San Mateo County has the most projected flood exposure due to climate change, with more than 140,000 people and $50 billion of property at risk of flooding through this century (“Hazard Reporting and Analytics (HERA)” 2017). San Mateo County’s bay shoreline is highly altered and contains critical public infrastructure, including the San Francisco International Airport, touchdowns of two regional bridges, an interstate highway, the heart of the Silicon Valley technology industry, and over 750,000 residents. Levees are an essential component of flood control throughout the region. San Mateo County is one of only six counties in the country with over 100,000 residents at risk of high-tide flooding with 0.9 m

of SLR, and assumptions of population growth (Hauer et al. 2016). A wide variety of pathways for integrating nature-based shorelines has been identified regionally (Beagle et al., 2019; BCDC, 2020; *Bay Adapt: Regional Strategy for a Rising Bay*, 2021), including horizontal levees, which are also sometimes called ecotone levees. With the highest future flood risk in the state and stakeholder interest in incorporating nature into climate adaptation approaches, San Mateo County's shoreline is a key study site for investigating the potential of horizontal levees as a nature-based flood defense (Figure 4.1).

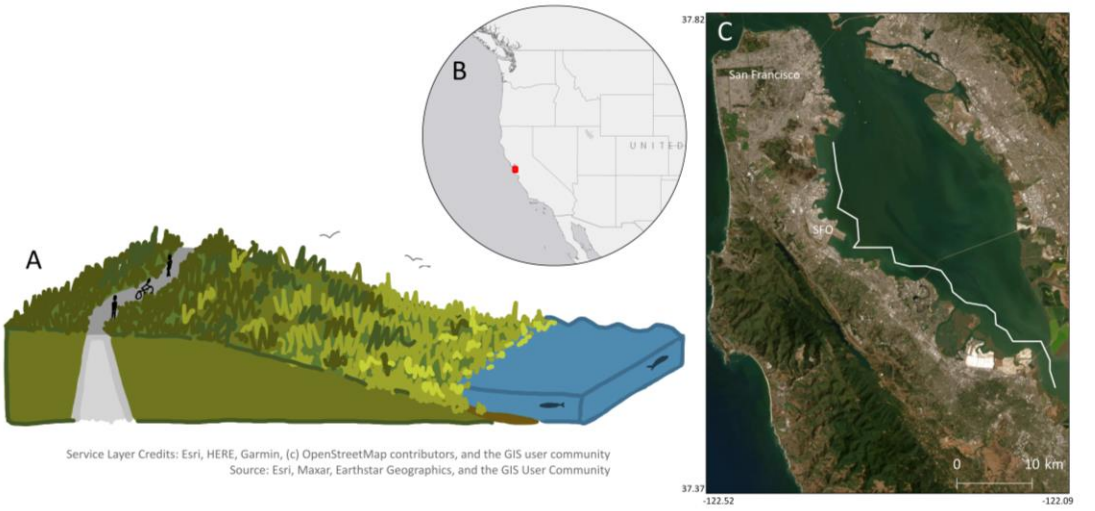

Figure 4.1 Depiction of a horizontal levee (A) and study location (B and C).

4.2.2 Numerical modeling

Effects of vegetation and levee overtopping are modeled with XBeach (Roelvink et al. 2009), a process-based model which simulates nearshore processes including wave transformation, wave-induced setup, over-wash, and inundation. Recently, a non-hydrostatic mode (XB-NH) was developed for XBeach (de Ridder et al. 2020), which is similar to a depth-averaged version of the SWASH model (Zijlema et al. 2011; Smit et al. 2013) and is able to fully resolve

incident-band (short period) waves. Resolution of incident-band waves, though computationally costly, is necessary to determine swash on relatively steep slopes and is thus necessary to investigate runup (as determined by the last wet grid cell), and potential overtopping on levees. Recent work has demonstrated the application of XB-NH for overtopping problems (Lashley et al. 2020).

Runup and overtopping in the non-hydrostatic mode have been validated using several separate datasets from sandy beaches. Results show that incident-band driven runup height is predicted with good accuracy and a maximum deviation from observations of 15% (Roelvink et al. 2018). A reduced two-layer non-hydrostatic formulation is included and allows for a more accurate description of the frequency dispersion in relatively deeper water. Relative depth (KD) determines whether waves are in deep water (waves do not interact with the bottom, $KD > \pi$) or shallow water (waves interact with the bottom, $KD < \pi/10$), and is based on water depth and wavelength. De Ridder et al. (2020) showed good performance up to a relative depth of 3.

XB-NH also allows for the inclusion of the effect of vegetation within the model via vegetation parameters including stem density, frictional drag coefficient, stem height, and stem diameter (van Rooijen et al. 2015; 2016). The combination of XB-NH and the vegetation module was calibrated to wave attenuation data from San Francisco Bay in Taylor-Burns et al. (2023). XB-NH can be computationally costly, particularly in shortwave environments where wavelengths and grid cell sizes are small. As a result, XB-NH was applied in this study in one-dimensional mode along transects as opposed to in two-dimensional mode on a lateral grid, since the flow at the levee section is considered predominantly shore normal. This approach

assumes that wave forcing is shore-normal and neglects lateral flow but allows us to apply the tool to a larger area and in multiple scenarios.

The XB-NH set up included a grid spacing of 30 grid points per wavelength (total number of grid points ranged from 2,000 to 12,000). Sensitivity analyses showed that the model results converge at this resolution. A Manning's friction formulation of 0.018 m^3/s was used for the mudflat on the unvegetated portion of each transect. Simulations all included 10 minutes of spin-up which were not used in the analysis and were 1000 waves in duration.

4.2.3 Transect development

In prioritizing where to apply one dimensional XB-NH within the study domain, both wave exposure and horizontal levee viability were considered. Beagle et al. (2019) identified which areas of the San Francisco Bay shoreline are suitable for horizontal levees, considering the appropriate elevation to support marsh habitat, proximity to urban development, and the capacity to accommodate a levee with at least a 1:30 slope. To find sections of the San Mateo County shoreline that are more exposed to waves, wave heights and water levels were extracted from storm simulations (Taylor-Burns et al. in review) approximately 120 m offshore from the first line of coastal defense. Wave formation in San Francisco Bay is limited by the Bay's shallow depths and constrained area, but in the main channels of the bay wave heights can exceed 1 m (O'Neill et al. 2017). These waves can propagate towards exposed shorelines of the bay. Coastal sections dominated by wind wave-levee interaction processes, as opposed to long-wave storm tide dominated areas, were identified through a ratio of wave and storm contribution to water level (shown in Equation 4.1, where Hs is significant wave height and TWL is total water level). Areas with a mean relative wave height to surge ratio of

greater than one which coincided with areas identified by Beagle et al. (2019) were selected for casting XB-NH transects (Figure 4.2).

$$Relative\ wave\ height\ to\ surge\ ratio\ = (Hs/(median\ Hs))/(\mathrm{T}WL/(median\ TWL)) \quad \text{(Eq. 4.1)}$$

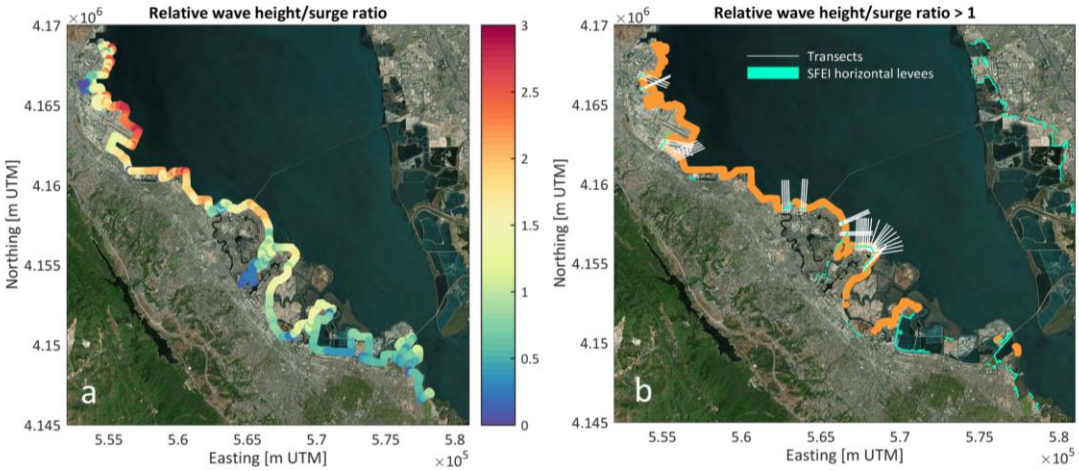

Figure 4.2 The relative wave height to surge ratio along throughout the study region (A) and areas with a relative wave height to surge ratio shown in orange, areas identified by Beagle et al. (2019) as suitable for horizontal levees shown in teal, and transects used in this study shown in white (B).

The Digital Shoreline Assessment System (DSAS, Himmelstoss et al. 2021) was used to cast transects and the results were modified manually to ensure transects are perpendicular to the existing levee. Bathymetry was interpolated using two different digital elevation models (DEMs): A 5 m resolution vegetation-corrected DEM, only available above -1 m NAVD88 (Buffington and Thorne 2018) was used above +1 m NAVD88 and a 10 m resolution DEM (Fregoso et al. 2017) was used below +1 m NAVD88. Switching between the two DEMs at +1 m NAVD88 provided the smoothest transition.

Throughout our study region, mean sea level is about +1 m NAVD88. 0.86 - 2.38 m NAVD88 was classified as marsh (Takekawa et al. 2013). Vegetation stem density, diameter, and height for the three marsh zones were taken from the meta-analysis done by Pinsky et al. (2013).

Several regional vegetation surveys have been done in San Francisco Bay, but they do not resolve the frictional coefficient of vegetation (C_d) as fully as Pinsky et al. (2013). Because C_d is a key parameter in assessing wave transformation across vegetation, the Pinsky et al. (2013) meta-analysis was utilized rather than local surveys. Stem density was 500 stems/m^2, stem height was 150 cm, and stem diameter was 7 mm. There are many areas in the study region that are at suitable elevation for marsh habitat but are developed and unvegetated. To ensure these places did not get assigned to be marsh habitat, vegetation was restricted to be offshore from first line of defense. The first line of defense was determined from a San Francisco Estuary Institute report (SFEI, 2016). Numerous studies show that C_d has an inverse relationship with Reynolds number (Re), which increases with increasing turbulence. This inverse relationship is caused by the bending and flexing of plant stems, which create less frictional drag in turbulent conditions. This relationship is important to account for when simulating wave decay by plants (e.g. Mendez and Losada 2004; Pinsky et al. 2013) to avoid overestimation of frictional drag by plant stems. Pinsky et al (2013) developed a generalized relationship between Re and C_d in marsh plants, which is based on uniformly post-processed data from 14 different studies ranging up to Re < 3000 (eq 4.2):

$$log_{10}(\boldsymbol{C_d}) = \quad (-1.72 \pm 0.93) + (-1.67 \pm 1.19) \times log_{10}(3 \times 10^{-4} \times \boldsymbol{Re}) \qquad \text{(Eq. 4.2)}$$

Equation 4.2 was used to determine appropriate drag coefficients for the marsh vegetation in the XB-NH model. An initial batch of simulations was completed across the full range of water level and wave combinations derived from the joint probability analysis. This was done to determine Re at the offshore edge of the vegetated zone within each transect. Re was then used to determine appropriate C_d for the vegetation within the marsh, as shown in Figure

S4.1. Experimental simulations were conducted with the C_d value calculated from the Pinsky et al. (2013) equation.

4.2.4 Wave and sea level data

Two previously modeled hindcasts were used to develop boundary conditions of water level and wave height for this model. A 30-year hindcast by O'Neill et al. (2017) simulated wave heights in San Francisco Bay using global climate model of near-surface daily winds paired with observations from four regional airports. This approach allowed the authors to keep the spatial resolution of modeled winds while increasing the temporal resolution by temporally downscaling and using observations to find a "best match" day. The maximum over-water windspeed was extracted each day of the hindcast and used to force a SWAN (Simulating WAves Nearshore) model, resulting in a time 30-year hindcast of daily maximum wave heights across San Francisco Bay. A 70-year hindcast by Nederhoff et al. (2021) used Delft3D Flexible Mesh to simulate water levels in San Francisco Bay from 1950 to 2019. Tidal constituents and a remote non-tidal residual (NTR, signal minus tide) forced the model at the open boundary. ERA5 wind and atmospheric pressure data (Hersbach et al. 2020) forced the model at the surface boundary. Creeks and delta flows were included in the model. Upstream boundaries for creeks were forced with data from 16 river discharge stations from the USGS. Upstream boundaries for the Delta were forced with estimates of Dayflow, which is an estimate of the daily average outflow from the Delta, accounting for water consumption across the region (California Department of Water Resources 2019). Modeled data was compared to observations from 15 NOAA tide gauges across the region, with an average skill score of 8 cm root mean square error. Point observations (model output time series at given

locations) are publicly available at about 500 m increments along the coast of San Francisco Bay. The resulting values from the Nederhoff et al. (2021) hindcast are representative of mean sea level, but because this study aims to assess levee overtopping, which is most likely to occur at high tides, a constant value of 0.85 m was added to the water level time series, which is representative of the difference between MHHW and MSL in this study region (Takekawa et al. 2013).

Boundary conditions were derived using a joint probability analysis toolbox (MvCAT, Sadegh et al. 2017), which requires time series observations of two variables at equal time steps. Thus, hindcasted wave and water levels from the overlapping 30-year time-period of 1974-2004 were used for the joint probability analysis. Daily wave height values were extracted from the 30-year wave hindcast at the end of each transect. Total water level data were extracted from the 70-year total water hindcast at the corresponding times (00:00 each day) from the nearest model output point to the offshore end of each transect and the tidal signal was removed using a low pass filter. The MvCAT toolbox includes 26 different copula and was used to determine joint probability curves for each transect. Across all 48 transects, the Ali-Mikhail-Haq (AMH) copula had the overall best score, so this copula was selected for determining return interval curves. Ranking for the various copula are shown in Table S4-1.

Wave heights and water levels at 25 cm increments and spanning the domain of the return interval curves values produced from the joint probability analysis were used as boundary conditions for the XB-NH simulations. Return period was interpolated across the two-dimensional space, thus assigning a return period for each combination of wave height and water level boundary conditions used as boundary conditions. An example of this approach is

shown in Figure 4.3, which shows hindcast wave and water level data in small gray circles. These points were used as input to the joint probability analysis, which produced the return period curves, shown in the thick black lines. The return period curves were then used to interpolate probability onto water level and wave combinations, shown in the large colored dots. The large colored dots were used as boundary conditions for XBeach simulations. Some of these boundary conditions are outside the range of modeled wave height and water level from O'Neill et al. (2017) and Nederhoff et al. (2021). The interpolated return period of these simulations is more uncertain than values that were within the range of the modeled time series. This uncertainty was quantified by bootstrapping with resampling. 1000 samples with a length of the full 300 year time series (10950 samples) were randomly taken from the original time series with replacement, and the MvCAT toolbox was used on each of the 1000 samples to create bootstrapped return period curves. These lines are shown by the gray lines in Figure 4.9 and they highlight that uncertainty in return period curves increases with higher return periods. The subsequent analyses use the original return period curves, which are shown in black. This analysis is focused on exploring overtopping under low-probability scenarios, and there are no available time series long enough to robustly capture low-probability events such as a 1 in 100 storm. Interpolation beyond the modeled data is not ideal, but it is necessary in this case. The joint probability analysis was used to assess how return period probabilities for combinations of wave heights and water levels will change with SLR.

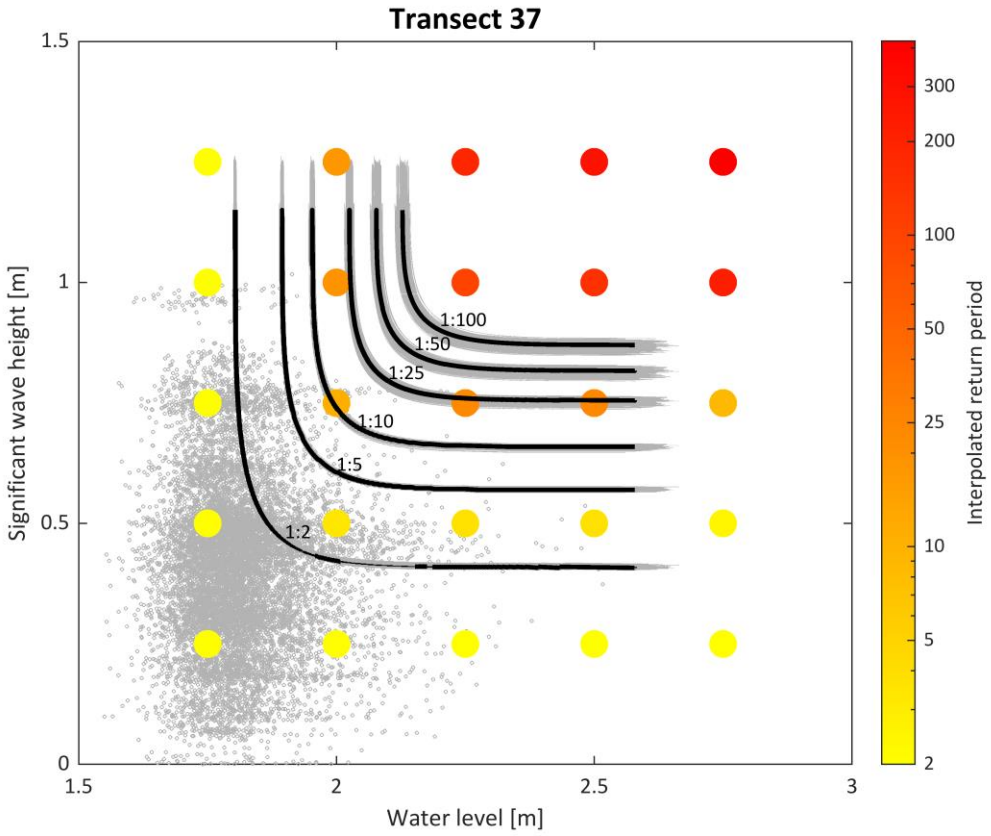

Figure 4.3 Gray dots show hindcast wave height (O'Neill et al., 2017) and water levels (Nederhoff et al., 2021) at or near the end of transect 37. These values were used as input for the joint probability analysis, which produced the return period curves which are shown in black. Text labels signify what the return period is for each of the six black lines. The gray lines underneath the thick black lines represent 1000 bootstrapped curves for each return period. The return period curves were used to determine the range and probability of boundary conditions in XB-NH. The boundary condition wave and water levels for XB-NH simulations are shown by the large colored dots. Color of the large dots represents interpolated return period for the water level and wave height combination. Yellow indicates short return period, or high probability, and red indicates long return period, or low probability. Thus, high water levels paired with large wave are less probable (red) than low water levels and with smaller waves (yellow).

4.2.5 Horizontal levee design alternatives

To assess how horizontal levee configuration influences wave decay and overtopping of the levee system, a range of slopes were applied to change bathymetry offshore from last vegetated grid cell, representing the shoreward edge of the marsh and the location of the

existing levee. Slopes ranged from 1/20, which is the steepest slope recommended by Beagle et al. (2019), to 1/100 (Figure 4.4). Vegetation zones were shifted accordingly, based on changes in elevation.

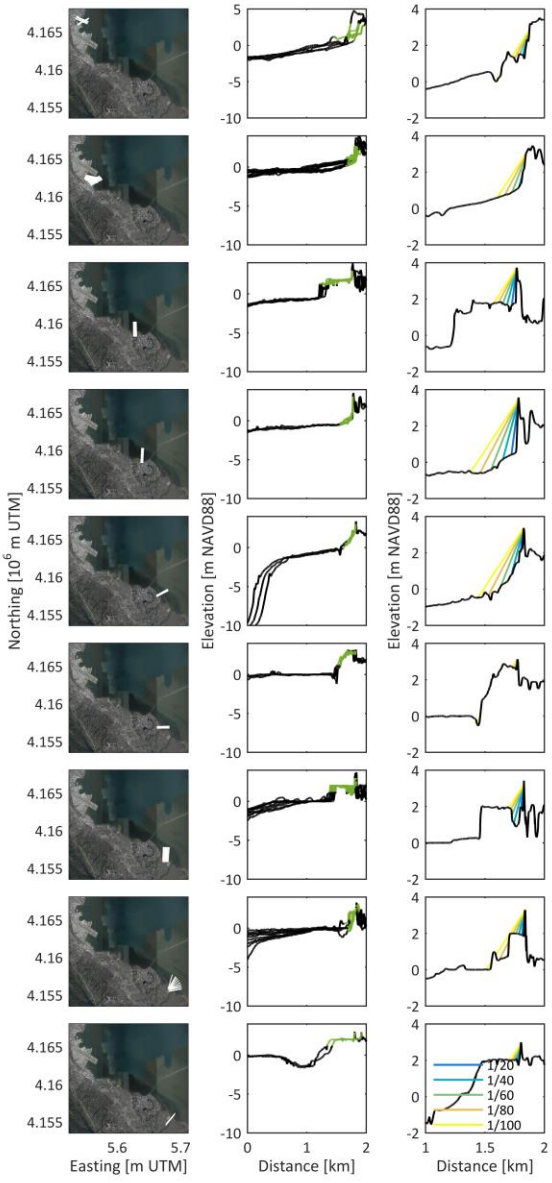

Figure 4.4 Location of transects (left column), bathymetry and elevation of the existing (middle column) and simulated horizontal levees with varying slopes (right column). Rows show groups of transects with similar bathymetry.

The sum of all shoreward flow over the levee crest was calculated for each simulation to determine cumulative flow over the levee crest, representing levee overtopping during the peak of a storm as it coincides with high tide. Cumulative flow over the levee crest and flow rate over the levee crest were compared to structural design thresholds identified by the EurOtop Manual in Table 4-1 (Van der Meer et al. 2018). The EurOtop Manual is a commonly used and widely cited document which has been applied and updated over decades, providing guidance on analysis and prediction of wave overtopping on various flood defenses.

Table 4-1 Limits for wave overtopping and structural design of breakwaters, seawalls, dikes, and dams from Van der Meer et al. (2018). Italicized text represents the design type and associated limits which are most relevant for this study, which is focused vegetated levee crests with relatively small significant wave heights.

Design type	Mean discharge q (L/s/m)	Maximum volume Q (L/m)
Rubble mound breakwaters; H_{m0} > 5 m; no damage	1	2000 – 3000
Rubble mound breakwaters; H_{m0} > 5 m; rear side designed for wave overtopping	5-10	10,000 – 20,000
Grass covered crest and landward slope; maintained and closed grass cover; H_{m0} = 1 – 3 m	5	2,000 – 3,000
Grass covered crest and landward slope; not maintained grass cover, open spots, moss and bare patches; H_{m0} = 0.5 – 3 m	.1	500
Grass covered crest and landward slope; H_{m0} < 1 m	*5 – 10*	*500*
Grass covered crest and landward slope; H_{m0} < 0.3 m	No limit	No limit

4.3 Results

4.3.1 Effects of sea level rise on overtopping risk

Levees are commonly designed to withstand a certain low-probability event, such as a 100-year storm. The joint probability analysis illustrates that as sea levels rise, the design limits of these structures will be tested on an increasingly frequent basis, highlighting the growing

need for adapting flood infrastructure. As sea level rises, present-day low-probability events will become increasingly frequent (Figure 4.5). For example, with 0.5 m SLR, the current 1 in 100-year wave and water levels will occur, 50 times more frequently, with less than a 1 in 2-year probability. This increase in frequency is shown by the gray star in figure 4.5, which marks where with 0 m SLR 1:100 year event will cause the same wave and water level conditions as a 0.5 m SLR 1:2 year event. This analysis is conservative as it does not account for increases in wave height due to increased depth and fetch. However, this significant shift in flood frequency with SLR is consistent with prior research (Vitousek et al. 2017; Taherkhani et al. 2020; Sweet et al. 2022).

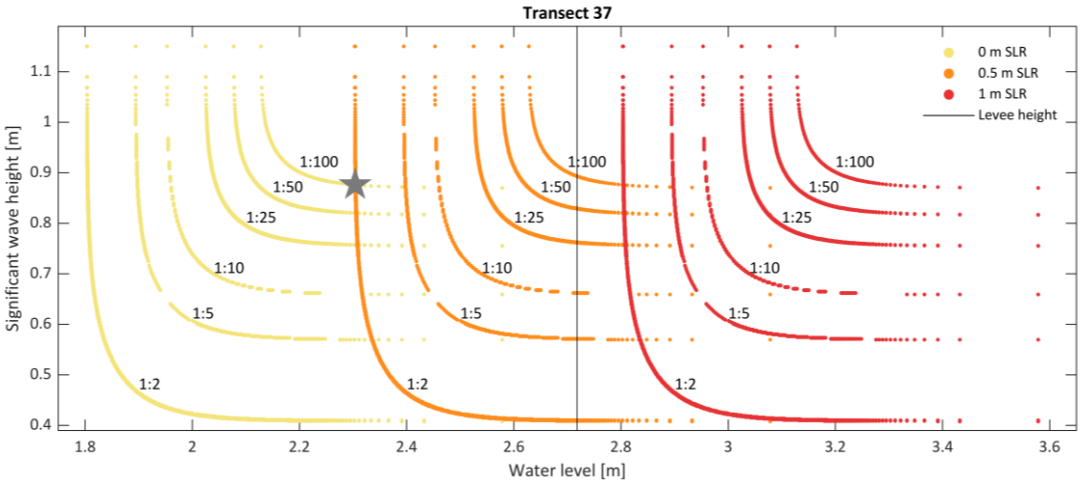

Figure 4.5 Joint probability return-period curves of co-occurring wave height and water levels on transect 37, with current sea level (yellow), 0.5 (orange) and 1 m of SLR (red). The black vertical line shows the levee crest height on transect 37. As sea levels rise, low probability events will become increasingly probable. An example of this increase in probability is shown by the gray star, which marks where with 0 m SLR 1:100 year event will cause the same wave and water level conditions as a 0.5 m SLR 1:2 year event. Thus, 0.5 m SLR makes 1:100 year storm conditions 50 times more probable.

Van der Meer et al. (2018) presents overtopping thresholds for different types of coastal protection structures and identifies a peak flow of more than 10 L/m/s or a cumulative

overtopping of more than 500 L/m/s as exceeding the structural design of levees like those in our study region. Thus, these thresholds are used to identify the probability of levee failure with sea level rise, which will cause exceedance of overtopping thresholds to become increasingly probable and severe, as shown by the expanding colored area going left to right in all rows of Figure 4.6, as well as by the increasing area of warm colors going left to right in all rows of Figure 4.6.

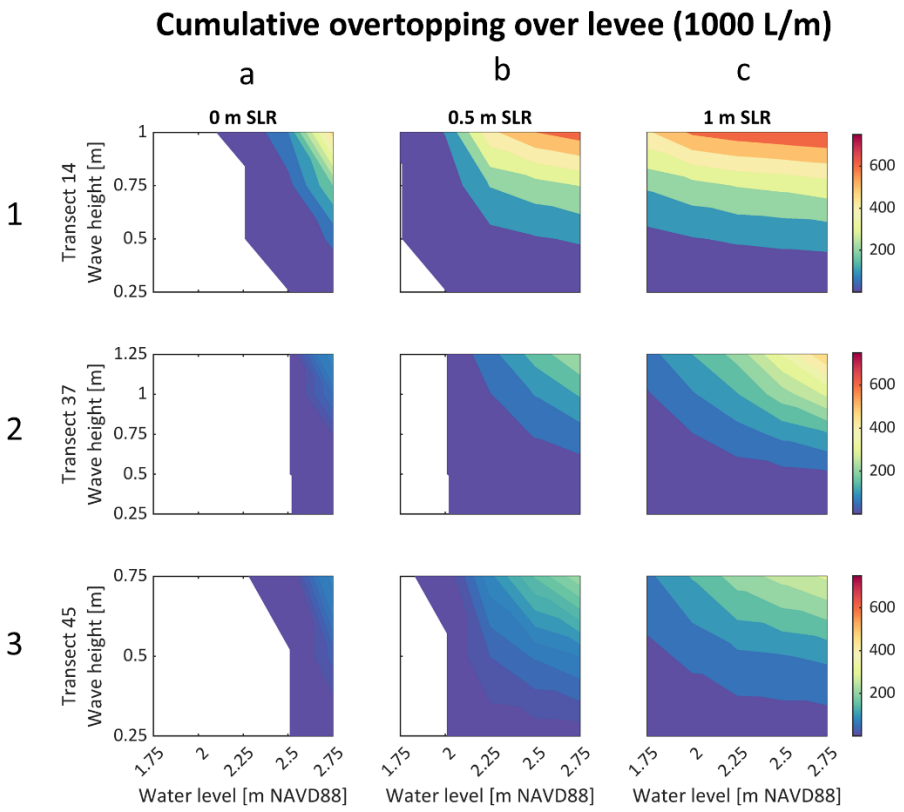

Figure 4.6 Cumulative levee overtopping on three different transects (rows) and with three different sea level rise (SLR) scenarios (columns). Water level is on the x-axis of all subplots and wave height is on the y-axis of all subplots. Color represents the magnitude of cumulative overtopping greater than 500 L/m at the given water level and wave combination. This threshold is identified as the structural design overtopping limit of levees of a design typical in San Francisco Bay. In all three transects, overtopping that surpasses the structural design of the levee system becomes increasingly probable with sea level rise, shown by the expanding colored area going from left to right.

4.3.2 Adaptation to sea level rise through horizontal levees

The hydrodynamic analysis indicates that horizontal levees can reduce the risk of levee overtopping beyond the structural design of the levee (Figure 4.7). As the slope of the horizontal levees become increasingly gradual, the magnitude of overtopping decreases, as shown by the shrinking area of warm colors going from left to right in columns (a) – (f). For example, with no adaptation, maximum cumulative overtopping on transect 14 is 475000 L/m, 654000 L/m, and 702000 L/m, with 0, 0.5, and 1 m of SLR, respectively. These values decrease to 377000 L/m, 550000 L/m, and 669000 L/m, with the implementation of a 1:20 horizontal levee and to 87000 L/m, 288000 L/m, 472000 L/m with the implementation of a 1:100 horizontal levee. These values are represented with the maximum overtopping values in Figure 4.7, represented by the warm colors in the upper right of each subplot. Gradually sloping horizonal levees allow waves to decay over a longer distance and across more vegetation before they reach the levee and cause runup and overtopping. Additionally, as the slope of the horizontal levee becomes increasingly gradual, the threshold of the structural design of the levee is surpassed in fewer simulations, shown by the colored area becoming smaller from left to right in the top two rows. This effect is not present in the bottom row, suggesting that on transect 14, levee overtopping will occur with 1 m of SLR, whether or not a horizontal levee is implemented. The simulations with high water levels and waves result in highest cumulative overtopping but are also the least likely to occur (e.g. Figure 4.2).

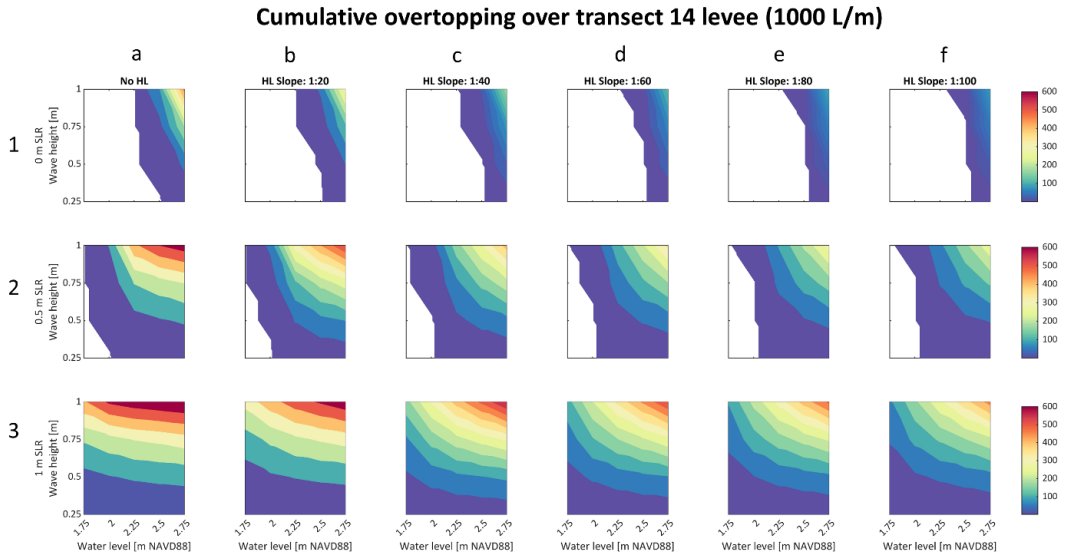

Figure 4.7 Cumulative overtopping on transect 14, with six different adaptation options shown in columns (a - f) and three different sea level scenarios shown in rows (1-3). The colored areas in columns (a – f) show overtopping greater than 500 L/m.

The probability of exceeding levee structural design thresholds can be calculated by weighting risk of failure by the probability of occurrence of each event (i.e., storm return periods). Across all the transects, various horizontal levee designs influence the probability of exceeding two different structural design thresholds of the levee system (Figure 4.8). Several general trends emerge. Horizontal levees are generally effective in reducing risk (shown by the vertical distance between scattered data points and the diagonal black line), and gradually sloping horizontal levees reduce probability of exceeding structural design thresholds better than steeper sloped designs (shown by the blue data points generally being closer to the diagonal black line than the yellow data points). Additionally, though there are some locations where horizontal levees have very limited influence on risk, most locations that have levee overtopping experience some degree of risk reduction by implementing horizontal levees. Because levees are increasingly overtopped throughout the study region

with SLR, the risk reduction benefits of horizontal levees increase with SLR and, reach up to 7%, 22%, and 30% with 0, 05, and 1 m SLR respectively.

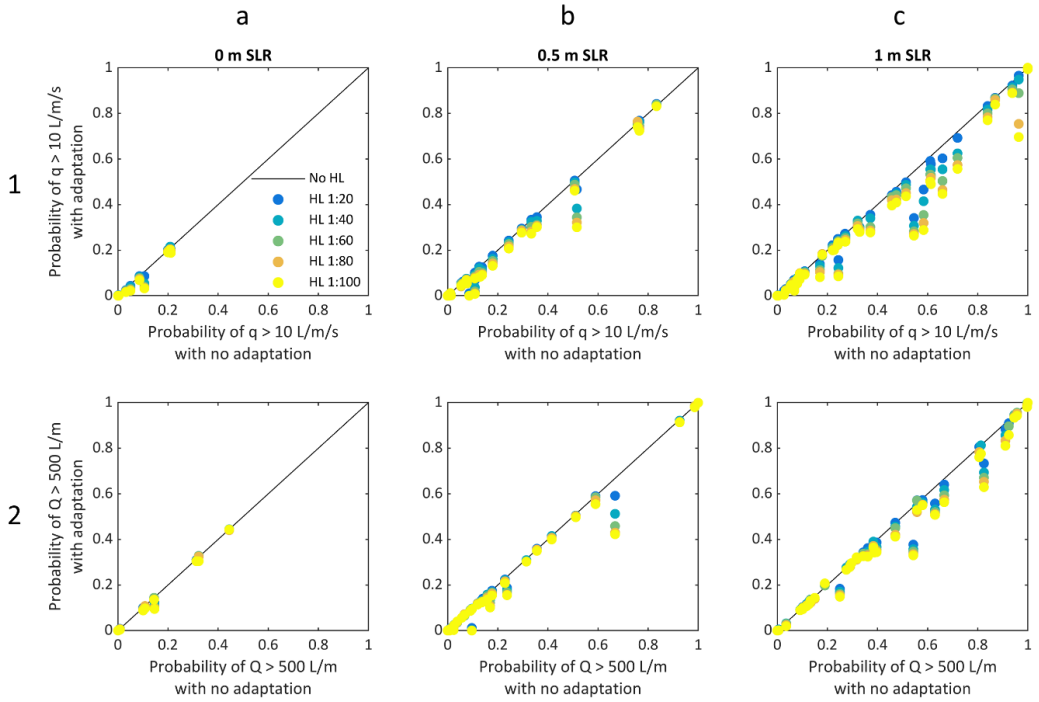

Figure 4.8 The probability of exceeding structural design thresholds of the levee on all 48 transects with five different adaptation options. The top row shows probability of exceeding q > 10 L/m/s; and the bottom row shows probability of exceeding Q > 500 L/m. Each column shows a different sea level rise scenario. The color of the dots signifies the adaptation option. Across the study region, the general trend shows that increasingly gradually sloped horizontal levees reduce the probability of exceeding the structural design thresholds. HL stands for horizontal levee in the legend.

The spatial distribution of risk reduction is shown in Figure 4.9. Risk reduction increases as sea levels rise, shown by the greater prevalence of colored lines going from left to right. Mean values in reducing the risk of q > 10 L/m/s across all 48 transects are a reduction by 0.4%, 2.0% and 5.3% with 0, 0.5, and 1 m of SLR, respectively. Mean values in reducing the risk of Q > 500 L/m across all 48 transects are a reduction by 0.2%, 1.5% and 2.9% with 0, 0.5, and 1 m of SLR, respectively. There are two main hotspots of risk reduction, shown by the

white stars in the top right subplot of Figure 4.9. These two areas both have relatively deep waters directly offshore from the levee, with no existing marsh platform to attenuate waves (Figure 4.10). Tests revealed that offshore water depth is a stronger control on risk reduction by horizontal levees than is wave height.

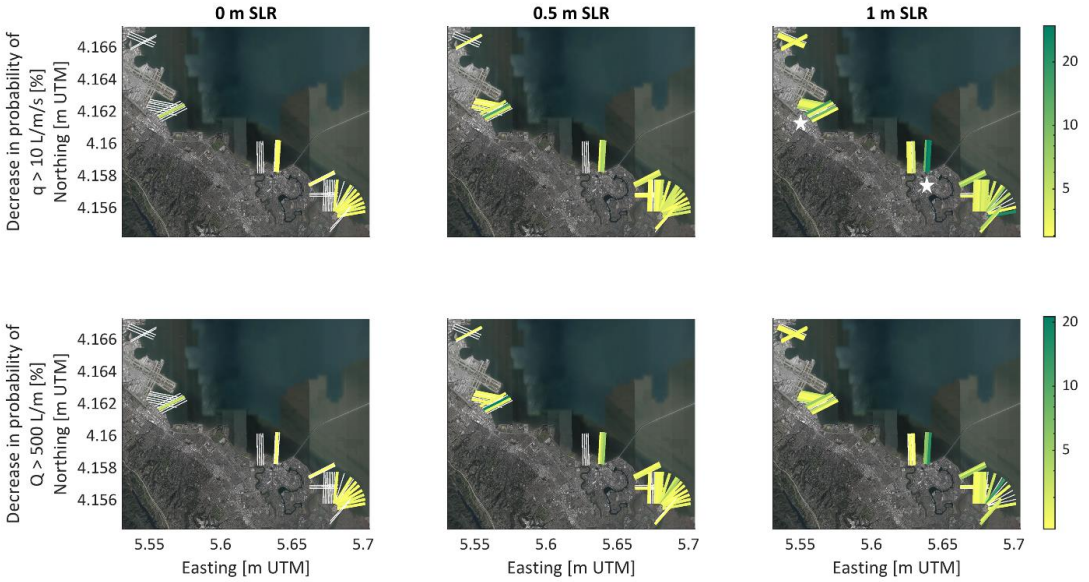

Figure 4.9 Decrease in probability of exceeding two different levee structural design thresholds due to horizontal levee implementation. The color of each transect signifies the decrease in failure risk delivered by implementing a 1:100 sloping horizontal levee. The top row shows the decrease in risk of exceeding 10 L/m/s and the bottom row shows the decrease in risk of exceeding 500 L/m. The three different columns show three different sea level scenarios. Green transects show places where horizontal levees are reducing the probability of levee failure by the greatest amount, reaching up to 30% in reduction of failure risk. The white star signifies two hotspots where horizontal levees are particularly effective. In both the top and the bottom row, horizontal levees decrease risk of overtopping. Horizontal levees play a stronger role as sea levels rise, shown by the increasing number of colored and dark colored transects, going from left to right. White stars in the top right plot denote hotspots of highest risk reduction from horizontal levees.

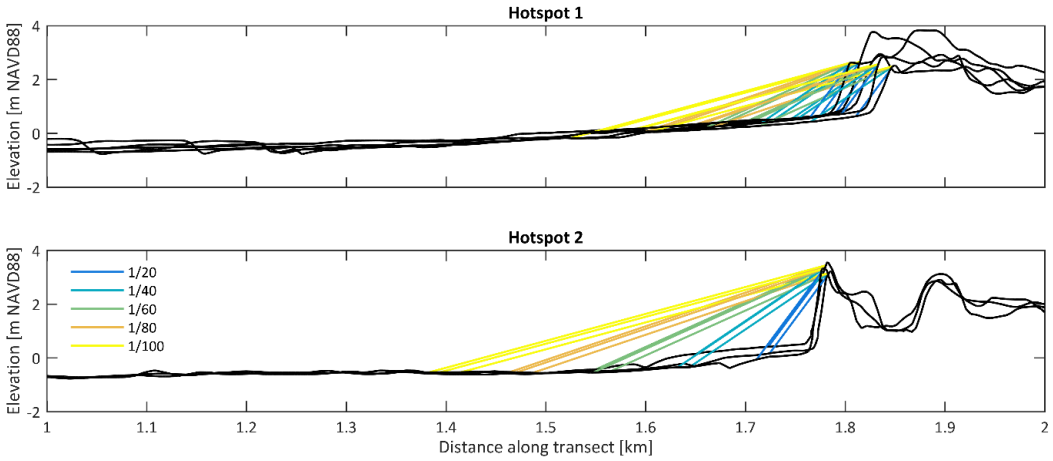

Figure 4.10 Bathymetry of transects in the two hotspots denoted in Figure 4.9, where horizontal levees provide the greatest risk reduction benefits. Hotspot 1 corresponds to the northwest star and hotspot 2 corresponds to the southeast star. In both hotspots the present levee drops off to relatively deep water, with little to no marsh habitat offshore from the existing levee.

4.4 Discussion and conclusions

This analysis investigates how SLR will affect levee overtopping risk from the joint action of waves and storm surges. SLR will challenge existing design thresholds and safety levels for future flood defenses. This study provides one of the first insights into nature-based adaptation options to increase the resilience and performance of levee systems. Engineering performance metrics were employed to test the effectiveness of horizontal levees as a hybrid green-gray coastal climate adaptation solution. Results suggest that horizontal levees can be an effective approach to adapt to and mitigate the impacts of increasing flood risk in urban estuaries like San Francisco Bay. Establishing horizontal levees in front of existing levee sections can reduce the risk of exceeding structural design limits of the levees.

More gradually sloping horizontal levees are better able to reduce this risk by providing a wider vegetation field that can reduce waves more than narrower and steeper horizontal

levees. For example, 1:100 sloped horizontal levees can reduce risk of overtopping that exceeds the structural design of the levee by up to 7%, 22% and 30% with 0, 0.5, and 1 m of SLR, while 1:20 sloped horizontal levees can reduce risk of structural exceedance by up to 3%, 8%, and 20%, with 0, 0.5 and 1 m of SLR, respectively. However, there is a tradeoff between using more gradually sloping horizontal levees, because even though they may provide more risk reduction benefits, they will cost more to implement as they have a larger footprint, thus requiring a larger spatial area of construction and larger land purchases. Hirschfeld and Hill (2017) show that land purchase cost could comprise more than half the total cost of adapting the San Francisco Bay levee system to prepare for climate change, suggesting that land purchase costs are non-trivial. Hotspots of risk reduction suggest that horizontal levees will deliver the greatest risk reduction in areas where the current levee is fronted by relatively deeper water with little to no existing marsh platform (Figure 4.9). This information can help managers prioritize where to invest in horizontal levees given limited adaptation funding.

Modeled wave decay in XB-NH has been calibrated in vegetated marshes (Taylor-Burns et al. 2023) and modeled overtopping in XB-NH has been compared to measurements and to output from other models, with results suggesting that XB-NH has higher skill in simulating overtopping than other models including OpenFOAM, SWASH, SWAN and XBeach Surfbeat (Lashley et al. 2020). However, overtopping in XB-NH through vegetation remains uncalibrated. This lack of data is a limitation of the present study and a promising area of further research. Calibration and validation of overtopping through vegetation should be explored before horizontal levees are widely implemented in climate adaptation plans. Furthermore, while this study relied on a review equation relating the vegetation drag

coefficient (C_d) and the Reynolds number (Re), this relationship is still an area of active research. Thus, it should be a research priority to obtain wave transformation and overtopping measurements across vegetation in high Reynolds number conditions. Even if these observations are obtained, it can be difficult to calculate C_d due to uncertainty and variation in methodology for vegetation surveys. This challenge has spurred recent research in quantifying wave attenuation in marshes by their standing biomass, (Maza et al. 2022), which requires only one field measurement rather than a minimum of three. Incorporating this approach into numerical models like XBeach would facilitate wave modeling through vegetation.

Sediment dynamics within marsh habitat are also important to consider. These dynamics control the degree to which marshes are or are not able to accrete sediment quickly enough to keep pace with sea level rise. San Francisco Bay marshes have been keeping up with sea level rise over the last 150 years by accreting 0.2 – 0.5 cm/year (Callaway et al. 2012), but these rates are less than 4% of what will be necessary to keep up with accelerating sea level rise by 2100 (Knowles 2010; Barnard et al. 2013). Further exacerbating insufficient accretion rates, riverine flood control structures channel sediment out to open water and dams impound sediment upstream, both disrupting the historic connection marshes have had with upland sediment sources. The relative elevations of marshes in San Francisco Bay are predicted to decrease by 0.4 to 1.3 m by 2100 (Swanson et al. 2014), causing marshes that do not have migration space to transition to mudflats (Elmilady et al. 2019). Sediment dynamics also influence whether marsh edge erosion or progradation will occur. Over recent decades, marshes in the wave-exposed northern part of San Francisco Bay have exhibited both spatial

and temporal variability in edge change on a local scale (SFEI and Baye 2020), though erosion is more likely to occur in a future with higher sea levels. Our model did not account for sediment interactions and future work could incorporate these processes.

This study assumed shore-normal flow by using one dimensional XB-NH, which was done due to computational limitations. This assumption is conservative because it ensures that, along most shorelines, waves take the shortest path across the marsh to the levee. However, it is possible that waves are focused on certain shoreline segments in embayments, and our approach neglects this possibility. Our approach also neglects the possibility of interactions between waves and alongshore currents.

We also assumed that regional levee failure will be caused by overtopping flow. This neglects the possibility of failure due to inertial forces introduced by high water levels and due to seismic activity. Moss and Eller (2007) outline six pathways for levee failure, including seepage and slumping/spreading, which can both be caused by high water levels without overtopping. Studies in the Sacramento-San Joaquin Delta have assessed risk to that region's levee system and show that failures can occur due to high water level events without overtopping and due to liquefaction caused by seismic activity (Mount and Twiss 2005; Deverel et al. 2016). These threats may also be applicable to the Bay Area's levee systems. Parts of the Bay that are built on fill (soft mud and sand), including several municipalities in San Mateo County. These areas are particularly vulnerable to liquefaction and many of them are within about 10 km from the San Andreas Fault. Further complicating these risks is the fact that most of the levees in San Francisco Bay are not certified by the Federal Emergency Management Agency and do not meet certain engineering criteria, meaning their limits are

not fully understood. Thus, levees may fail for other reasons before overtopping ever occurs. A comprehensive geotechnical risk assessment for the Bay's levee system would help illustrate how realistic this assumption is.

Finally, in this analysis the MvCAT toolbox was used with local optimization for copula parameters as opposed to optimization using the Monte Carlo Markov Chain algorithm, which produces a more robust estimate of copula parameters. Additionally, the MvCAT toolbox assumes that copula represent the probability of one or both parameters exceeding a value, known as an "OR" copula. However, in this context it would be more appropriate to use assume that both parameters are exceeded, known as an "AND" copula. Next steps to improve this work will be to utilize the Monte Carlo Markov Chain algorithm for copula parameter selection and to modify the MvCAT toolbox to allow for "AND copulas. Together, these steps would improve the estimations of probabilities associated with each XBeach simulation.

Despite these limitations, results from this study are promising. This work illustrates that levees can meaningfully reduce risk of levee failure in urban estuaries like San Francisco Bay, while simultaneously offering potential for other co-benefits such has habitat, carbon sequestration, and recreation opportunities. Further, the risk reduction benefits provided by horizontal levees increase with SLR, suggesting that with further study, this hybrid infrastructure approach can be a part of the solution as communities face the need to adapt to rising sea levels.

References

Barnard, Patrick L., David H. Schoellhamer, Bruce E. Jaffe, and Lester J. McKee. 2013. "Sediment Transport in the San Francisco Bay Coastal System: An Overview." *Marine*

Geology 345: 3–17. https://doi.org/10.1016/j.margeo.2013.04.005.

"Bay Adapt: Regional Strategy for a Rising Bay." 2021. https://www.bayadapt.org/wp-content/uploads/2022/01/BayAdapt_JointPlaform_Final_Oct2021.pdf.

BCDC, Caltrans, MTC, ABAG, and BARC. 2020. "Adapting to Rising Tides Bay Area, Regional Sea Level Rise Vulnerability and Adaptation Study," no. March: 205. http://www.adaptingtorisingtides.org/project/art-bay-area/.

Beagle, Julie, Jeremy Lowe, Katie McKnight, Sam Safran, Laura Tam, and Sarah Jo Szambelan. 2019. "San Francisco Bay Shoreline Adapation Atlas: Working with Nature to Plan for Sea Level Rise Using Operational Landscape Units."

Buffington, KJ, and KM Thorne. 2018. "LEAN-Corrected San Francisco Bay Digital Elevation Model." U.S. Geological Survey.

California Department of Water Resources. 2019. "Dayflow." 2019. https://data.ca.gov/datase t/dayflow.

Callaway, John C., Evyan L. Borgnis, R. Eugene Turner, and Charles S. Milan. 2012. "Carbon Sequestration and Sediment Accretion in San Francisco Bay Tidal Wetlands." *Estuaries and Coasts* 35 (5): 1163–81. https://doi.org/10.1007/s12237-012-9508-9.

Deverel, Steven J., Sandra Bachand, Scott J. Brandenberg, Cathleen E. Jones, Jonathan P. Stewart, and Paolo Zimmaro. 2016. "Factors and Processes Affecting Delta Levee System Vulnerability." *San Francisco Estuary and Watershed Science* 14 (4). https://doi.org/10.15447/sfews.2016v14iss4art3.

Elmilady, H., M. van der Wegen, D. Roelvink, and B. E. Jaffe. 2019. "Intertidal Area Disappears Under Sea Level Rise: 250 Years of Morphodynamic Modeling in San Pablo Bay, California." *Journal of Geophysical Research: Earth Surface* 124 (1): 38–59. https://doi.org/10.1029/2018JF004857.

Foster-Martinez, M. R., J. R. Lacy, M. C. Ferner, and E. A. Variano. 2018. "Wave Attenuation across a Tidal Marsh in San Francisco Bay." *Coastal Engineering* 136 (February): 26–40. https://doi.org/10.1016/j.coastaleng.2018.02.001.

Foxgrover, Amy C., Mark Marvin-DiPasquale, Bruce E. Jaffe, and Theresa A. Fregoso. 2019. "Slough Evolution and Legacy Mercury Remobilization Induced by Wetland Restoration in South San Francisco Bay." *Estuarine, Coastal and Shelf Science* 220 (August 2018): 1–12. https://doi.org/10.1016/j.ecss.2019.02.033.

Fregoso, T.A., R-F. T. Wang, E.S. Ateljevich, and B.E Jaffe. 2017. "A New Seamless, High-Resolution Digital Elevation Model of the San Francisco Bay-Delta Estuary." https://doi.org/Https://doi.org/10.3133/ofr20171067.

Hauer, Mathew E., Jason M. Evans, and Deepak R. Mishra. 2016. "Millions Projected to Be at Risk from Sea-Level Rise in the Continental United States." *Nature Climate Change* 6 (7): 691–95. https://doi.org/10.1038/nclimate2961.

"Hazard Reporting and Analytics (HERA)." 2017. https://www.usgs.gov/apps/hera/.

Hersbach, Hans, Bill Bell, Paul Berrisford, Shoji Hirahara, András Horányi, Joaquín Muñoz-Sabater, Julien Nicolas, et al. 2020. "The ERA5 Global Reanalysis." *Quarterly Journal of the Royal Meteorological Society* 146 (730): 1999–2049. https://doi.org/10.1002/qj.3803.

Himmelstoss, Emily A., Rachel E. Henderson, Meredith G. Kratzmann, and Amy S. Farris. 2021. "Digital Shoreline Analysis System (DSAS) Version 5.1 User Guide," 104.

Hirschfeld, Daniella, and Kristina E. Hill. 2017. "Choosing a Future Shoreline for the San Francisco Bay: Strategic Coastal Adaptation Insights from Cost Estimation." *Journal of Marine Science and Engineering* 5 (3): 42. https://doi.org/10.3390/jmse5030042.

Knowles, Noah. 2010. "Potential Inundation Due to Rising Sea Levels in the San Francisco Bay Region." *San Francisco Estuary and Watershed Science* 8 (1). https://doi.org/10.15447/sfews.2010v8iss1art1.

Lashley, Christopher H., Barbara Zanuttigh, Jeremy D. Bricker, Jentsje van der Meer, Corrado Altomare, Tomohiro Suzuki, Volker Roeber, and Patrick Oosterlo. 2020. "Benchmarking of Numerical Models for Wave Overtopping at Dikes with Shallow Mildly Sloping Foreshores: Accuracy versus Speed." *Environmental Modelling and Software* 130 (April): 104740. https://doi.org/10.1016/j.envsoft.2020.104740.

Maza, Maria, Javier L. Lara, and Inigo J. Losada. 2013. "A Coupled Model of Submerged Vegetation under Oscillatory Flow Using Navier-Stokes Equations." *Coastal Engineering* 80: 16–34. https://doi.org/10.1016/j.coastaleng.2013.04.009.

Maza, Maria, Javier L Lara, and Iñigo J Losada. 2022. "A Paradigm Shift in the Quantification of Wave Energy Attenuation Due to Saltmarshes Based on Their Standing Biomass." *Scientific Reports*, 1–13. https://doi.org/10.1038/s41598-022-18143-6.

Meer, J.W. Van der, N.W.H. Allsop, T. Bruce, J. De Rouck, A. Kortenhaus, T. Pullen, H. Schüttrumpf, et al. 2018. "Manual on Wave Overtopping of Sea Defences and Related Structures. An Overtopping Manual Largely Based on European Research, but for Worldwide Application." *Report*, 264. www.overtopping-manual.com.

Mendez, Fernando J., and Inigo J. Losada. 2004. "An Empirical Model to Estimate the Propagation of Random Breaking and Nonbreaking Waves over Vegetation Fields." *Coastal Engineering* 51 (2): 103–18. https://doi.org/10.1016/j.coastaleng.2003.11.003.

Moss, Robb Eric S., and J. Michael Eller. 2007. "Estimating the Probability of Failure and Associated Risk of the California Bay Delta Levee System." In *Geo-Denver: Probabilistic Applications in Geotechnical Engineering*, 1–10. Denver, CO. https://doi.org/10.1061/40914(233)21.

Mount, Jeffrey, and Robert Twiss. 2005. "Subsidence , Sea Level Rise , and Seismicity in the Sacramento-San Joaquin Delta." *San Francisco Estuary and Watershed Science*.

Narayan, Siddharth, Michael W. Beck, Paul Wilson, Christopher J. Thomas, Alexandra

Guerrero, Christine C. Shepard, Borja G. Reguero, Guillermo Franco, Jane Carter Ingram, and Dania Trespalacios. 2017. “The Value of Coastal Wetlands for Flood Damage Reduction in the Northeastern USA.” *Scientific Reports* 7 (1): 1–12. https://doi.org/10.1038/s41598-017-09269-z.

Nederhoff, Kees, Rohin Saleh, Babak Tehranirad, Liv Herdman, Li Erikson, Patrick L. Barnard, and Mick van der Wegen. 2021. “Drivers of Extreme Water Levels in a Large, Urban, High-Energy Coastal Estuary – A Case Study of the San Francisco Bay.” *Coastal Engineering* 170 (March). https://doi.org/10.1016/j.coastaleng.2021.103984.

O’Neill, A. C., L. H. Erikson, and P. L. Barnard. 2017. “Downscaling Wind and Wavefields for 21st Century Coastal Flood Hazard Projections in a Region of Complex Terrain.” *Earth and Space Science* 4 (5): 314–34. https://doi.org/10.1002/2016EA000193.

Olander, Lydia, Krystal Laymon, and Heather Tallis. 2022. “Opportunities to Accelerate Nature-Based Solutions : A Roadmap for Climate Progress , Thriving Nature , Equity, & Prosperity. A Report to the National Climate Taskforce.,” no. November: 1–44.

Pinsky, Malin L., Greg Guannel, and Katie K. Arkema. 2013. “Quantifying Wave Attenuation to Inform Coastal Habitat Conservation.” *Ecosphere* 4 (8). https://doi.org/10.1890/ES13-00080.1.

Reguero, Borja G, Michael W Beck, David N Bresch, Juliano Calil, and Imen Meliane. 2018. “Comparing the Cost Effectiveness of Nature- Based and Coastal Adaptation : A Case Study from the Gulf Coast of the United States.” *PLoS ONE* 13 (4): 1–24. https://doi.org/10.17605/OSF.IO/D6R5U.

Reguero, Borja G, Curt D Storlazzi, Ann E Gibbs, James B Shope, Aaron D Cole, Kristen A Cumming, and Michael W Beck. 2021. “The Value of US Coral Reefs for Flood Risk Reduction.” *Nature Sustainability* 4 (8): 688–98. https://doi.org/10.1038/s41893-021-00706-6.

Ridder, Menno P. de, Pieter B. Smit, Ap van Dongeren, Robert McCall, Kees Nederhoff, and Ad J.H.M. Reniers. 2020. “Efficient Two-Layer Non-Hydrostatic Wave Model with Accurate Dispersive Behaviour.” *Coastal Engineering* 164 (October 2020): 103808. https://doi.org/10.1016/j.coastaleng.2020.103808.

Roelvink, Dano, Robert McCall, Seyedabdolhossein Mehvar, Kees Nederhoff, and Ali Dastgheib. 2018. “Improving Predictions of Swash Dynamics in XBeach: The Role of Groupiness and Incident-Band Runup.” *Coastal Engineering* 134 (July 2017): 103–23. https://doi.org/10.1016/j.coastaleng.2017.07.004.

Roelvink, Dano, Ad Reniers, Ap van Dongeren, Jaap van Thiel de Vries, Robert McCall, and Jamie Lescinski. 2009. “Modelling Storm Impacts on Beaches, Dunes and Barrier Islands.” *Coastal Engineering* 56 (11–12): 1133–52. https://doi.org/10.1016/j.coastaleng.2009.08.006.

Rooijen, A. A. van, R. T. McCall, J. S. M. van Thiel de Vries, A. R. van Dongeren, A. J. H. M Reniers, and J. A. Roelvink. 2016. “Modeling the Effect of Wave Vegetation Interaction

on Wave Setup." *Journal of Geophysical Research: Oceans* 121. https://doi.org/10.1002/2015JC011486.Received.

Rooijen, A.A. van, J.S.M. van Thiel de Vries, R.T. McCall, A.R. van Dongeren, J.A. Roelvink, and A.J.H.M. Reniers. 2015. "Modeling of Wave Attenuation by Vegetation with XBeach." *E-Proceedings of the 36th IAHR World Congress*, 7.

Sadegh, Mojtaba, Elisa Ragno, and Amir Aghakouchak. 2017. "Multivariate Copula Analysis Toolbox (MvCAT): Describing Dependence and Underlying Uncertainty Using a Bayesian Framework." *Water Resources Research* 53. https://doi.org/10.1111/j.1752-1688.1969.tb04897.x.

San Francisco Bay Restoration Authority. 2017. "Grants Funded by Measure AA : The San Francisco Bay Clean Water , Pollution Prevention and Habitat Restoration Measure June 2017," no. June. https://sta.ca.gov/wp-content/uploads/STA/Groups/STA Board/Meeting Agendas/2017/09-13-17/11.Ba_Att A Measure AA.pdf.

San Francisco Estuary Institute (SFEI). 2016. "No Title." San Francisco Bay Shore Inventory: Mapping for Sea Level Rise Planning GIS Data. 2016. http://www.sfei.org/projects/SFBayShoreInventory.

SFEI, and Peter Baye. 2020. "New Life for Eroding Shorelines: Beach and Marsh Edge Change in the San Francisco Estuary." Richmond, CA: San Francisco Estuary Institude.

Smit, Pieter, Marcel Zijlema, and Guus Stelling. 2013. "Depth-Induced Wave Breaking in a Non-Hydrostatic, near-Shore Wave Model." *Coastal Engineering* 76: 1–16. https://doi.org/10.1016/j.coastaleng.2013.01.008.

Swanson, Kathleen M., Judith Z. Drexler, David H. Schoellhamer, Karen M. Thorne, Mike L. Casazza, Cory T. Overton, John C. Callaway, and John Y. Takekawa. 2014. "Wetland Accretion Rate Model of Ecosystem Resilience (WARMER) and Its Application to Habitat Sustainability for Endangered Species in the San Francisco Estuary." *Estuaries and Coasts* 37 (2): 476–92. https://doi.org/10.1007/s12237-013-9694-0.

Sweet, W.V., B.D. Hamlington, R.E. Kopp, C.P. Weaver, P.L. Barnard, D. Bekaert, W. Brooks, et al. 2022. "Global and Regional Sea Level Rise Scenarios for the United States: Updated Mean Projections and Extreme Water Level Probabilities along U.S. Coastlines."

Taherkhani, Mohsen, Sean Vitousek, Patrick L. Barnard, Neil Frazer, Tiffany R. Anderson, and Charles H. Fletcher. 2020. "Sea-Level Rise Exponentially Increases Coastal Flood Frequency." *Scientific Reports* 10 (1): 1–18. https://doi.org/10.1038/s41598-020-62188-4.

Takekawa, J Y, K M Thorne, K J Buffington, K A Spragens, K M Swanson, J Z Drexler, D H Schoellhamer, C T Overton, and M L Casazza. 2013. "Final Report for Sea-Level Rise Response Modeling for San Francisco Bay Estuary Tidal Marshes." *U.S. Geological Survey Open File Report 2012-1081*, 161.

Taylor-Burns, Rae, Chris Lowrie, Babak Tehranirad, Jeremy Lowe, Li H. Erikson, Patrick L. Barnard, Borja G. Reguero, and Michael W. Beck. n.d. "The Value of Marsh Restoration

for Flood Risk Reduction under Climate Change in an Urban Estuary." *Nature Climate Change*.

Taylor-Burns, Rae, Kees Nederhoff, Jessica R. Lacy, and Patrick L. Barnard. 2023. "The Influence of Vegetated Marshes on Wave Transformation in Sheltered Estuaries." *Coastal Engineering* 184 (March 2022): 104346. https://doi.org/10.1016/j.coastaleng.2023.104346.

Vitousek, Sean, Patrick L Barnard, Charles H Fletcher, Neil Frazer, Li H Erikson, and Curt D Storlazzi. 2017. "Doubling of Coastal Flooding Frequency within Decades Due to Sea-Level Rise." *Nature Scientific Reports* 7: 1–9. https://doi.org/10.1038/s41598-017-01362-7.

Zelst, Vincent T.M. van, Jasper T. Dijkstra, Bregje K. van Wesenbeeck, Dirk Eilander, Edward P. Morris, Hessel C. Winsemius, Philip J. Ward, and Mindert B. de Vries. 2021. "Cutting the Costs of Coastal Protection by Integrating Vegetation in Flood Defences." *Nature Communications* 12 (1): 1–11. https://doi.org/10.1038/s41467-021-26887-4.

Zijlema, Marcel, Guus Stelling, and Pieter Smit. 2011. "SWASH : An Operational Public Domain Code for Simulating Wave Fi Elds and Rapidly Varied Fl Ows in Coastal Waters." *Coastal Engineering* 58 (10): 992–1012. https://doi.org/10.1016/j.coastaleng.2011.05.015.

Conclusions

Rising sea levels will continue to increase flood risk in coastal communities, and coastal habitat restoration can play a strong role in reducing this risk by altering flow and reducing wave energy. Traditional engineering and planning tools such as hydrodynamic models have long been used to assess the efficacy of "gray infrastructure", such as sea walls, levees and berms, but these approaches have not been applied to assess how nature-based solutions can reduce flood risk until more recently. To fully integrate nature-based solutions to coastal flood risk reduction, it is necessary to assess their efficacy with the same rigor as is applied to gray alternatives. This dissertation uses quantitative coastal engineering tools and approaches to assess how marsh habitat can reduce current and future flood risk in a densely urbanized estuary, contributing new research to support the integration of nature into coastal climate adaptation frameworks.

In chapter one, a wave-resolved numerical model was applied to investigate how vegetated marshes influence wave transformation, particularly wave runup. The model was calibrated to observations and then used to examine how marsh and hydrodynamic characteristics change the potential for marshes to mitigate wave driven flooding. Results suggest that in comparison to wave propagation over an unvegetated mudflat, marsh vegetation reduces runup by a median of 40 cm and wave height by a median of 35 cm, even across only 50 m of marsh width. In urban estuaries like San Francisco Bay, which is already beginning to experience the flooding impacts associated with climate change, a 40 cm reduction in dynamic water levels is meaningful for planning purposes and could be a strong incentive to invest in marsh conservation and restoration. By reducing the required height of the Bay area's levee system by 0.5 m, salt marsh vegetation could save $3.5 million per kilometer of

levee, based on existing estimates of levee construction costs (van Zelst et al. 2021), resulting in net savings of $3.5 billion across the approximately 1000 kilometers of bay area shoreline.

In chapter two, a two-dimensional coupled wave-flow hydrodynamic model was used to value the flood protection benefits of stakeholder-identified marsh restoration under current and future climate change in San Mateo County, the California county most vulnerable to future flooding. Results show that marsh restoration provides a present value of $21 million which increases to over $100 million with 0.5 m of sea level rise (SLR), and to about $500 million with 1 m of SLR. We identify hotspots where marsh restoration delivers the highest benefits for adaptation, which reach $9 million/hectare. These findings show that today's investments in nature and community resilience can result in increasing payoffs as climate change progresses and risk increases.

Chapter three explores the limitations of marsh restoration for risk reduction in one of San Francisco Bay's salt ponds, which is built on a diked and drained historical marsh. Results demonstrate that marsh restoration in hydraulically altered ponds or inlets must be strategically done to maintain community safety. Narrow tidal inlets and volume modification of the inlet or pond can amplify water levels during storms and high tides, while creating wider tidal inlets and maximizing the volume of the inlet or pond both reduce the risk of tidal amplification. Hydraulically altered wetlands represent a large proportion of potential marsh restoration sites nationally, and these results can guide such restoration efforts.

Chapter four explores how establishing marsh habitat in front of levees with horizontal levees can reduce the risk of levee overtopping. Results illustrate that sea level rise will increase the likelihood of occurrence of low-probability storm events. For example, with 0.5 m of SLR, the

current 100-year event will occur semi-annually. This shift will increasingly test the limits of regional flood control infrastructure, highlighting the need for adaptation. Results also show that horizontal levees can provide adaptation benefits by reducing the probability that structural design thresholds of levees are exceeded during storms. The hydrodynamic analyses illustrate that horizontal levees can reduce probability of exceeding the structural design limit of the levee by up to 7% with present sea level. With 0.5 m and 1 m of SLR, this value increases to 22% and 30% respectively, demonstrating that this hybrid nature-based climate adaptation approach can be a part of the solution in adapting to rising sea levels.

The models used in this dissertation are state of the art and widely used, but they do have limitations and shortcomings. The XBeach simulations were all done in one dimension due to computational limitations, neglecting numerous alongshore processes that occur on complex shorelines like San Francisco Bay. The Delft3D and SWAN simulations do not account for swash processes due to the limits of the models themselves. None of our work incorporated sediment dynamics or pluvial flooding, which are both important factors to consider. All models used here have been tested and validated during present day conditions, but calibration data is limited during extreme events, and cannot be collected in the field in conditions that represent a future with sea level rise. To facilitate reliable model data, observations are needed during storms, high tides, and ideally also from flumes where sea level rise can be simulated. These measurements will facilitate model calibration and validation during conditions of interest and increase confidence in model results for high water level and large wave conditions. Advancing the study of sediment dynamics in mashes is equally important to further constrain if and how these tidal habitats will persist in a future

with sea level rise, increasing confidence in model results for sea level rise scenarios. Sediment dynamics vary geographically depending on relative sea level rise and sediment availability, which presents a challenge. However, marsh accretion rates and edge stability may also present management goals. Thin layer sediment placement of mud on marsh platforms can be an effective way to support vegetation and build elevation. Edging and sills can be effective in stabilizing marsh edges. Investing in these approaches could be worthwhile on urban coastlines.

Aside from model limitations, implementation of any of these results is limited by the ability and will of managers to take action to invest in conservation and restoration based on risk reduction metrics. Access to funding is a common limitation but results like those presented here can open access to new funding sources. For example, quantifying the risk reduction benefit of habitat restoration can facilitate benefit cost analyses, and where restoration projects have a sufficient ratio, it may be possible to apply for and receive FEMA grants for increasing community resilience. This type of work also facilitates insurance and other risk transfer mechanisms to support funding for habitat restoration. If a seawall can be insured, the argument can be made that a coral reef which provides the same service as a seawall should also be insurable. This type of policy was written to protect the meso-American reef in Quintana Roo, Mexico several years ago. Shortly after the policy was written, a hurricane passed over the reef causing damage, and subsequently an insurance payout was made to fund habitat restoration. Similarly, if a property owner could receive a premium reduction by building a bulkhead, the argument can be made that if marsh restoration would serve the same purpose, habitat restoration should also result in a decreased premium, resulting in

savings. However, habitat restoration funding, even when available, is not commonly allocated based on risk reduction metrics, but rather on ecological metrics. Pairing the type of work included in this dissertation with ecological analyses may facilitate aligning the two goals. Pilot restoration projects that show quantifiable risk reduction benefits may help gain confidence in restoration for risk reduction, potentially increasing the use of this approach.

A drawback of nature-based solutions for coastal flood risk reduction is that they will almost always require more time and space to grow than traditional engineering approaches. Concrete can be poured in a matter of days or weeks, but a successful habitat restoration can take years or decades to fully establish. However, concrete will never evolve or adapt to changing conditions, but marshes, coral reefs, and mangroves can shift, grow, accrete, and repair themselves. The capitalistic focus on short-term gains rather than long-term sustainability has been a major driver in creating the climate crisis. While threats of climate change are imminent in many places, we need to learn from our past mistakes and chose adaptation strategies that will meet goals for decades to come. In a similar vein, while benefit cost analyses can be a powerful tool in assessing and selecting adaptation measures, the commonly used and Federal Emergency Management Agency (FEMA) mandated 7% discount rate (the rate which is used to "discount" future benefits in comparison to present day benefits or costs) is arbitrary and arguably too high. Lowering this rate to 3% or 5% would enable communities to invest in long-term climate solutions such as habitat restoration rather than relying on quick fixes that may not last.

Collectively, this suite of work provides motivation and guidance for integrating marsh habitat conservation and restoration into coastal risk reduction plans and budgets. Results from

chapter one and three are idealized and can thus be used to inform planning in other urban estuaries. Results from chapter two and four are specific to San Mateo County, CA, but the approach used here can be applied to other areas to quantify climate adaptation benefits of marsh restoration. Using traditional engineering approaches, this dissertation shows that marsh habitat can play an important role in reducing coastal flood risk in an era of climate change, supporting both community safety and conservation goals.

Supplementary material

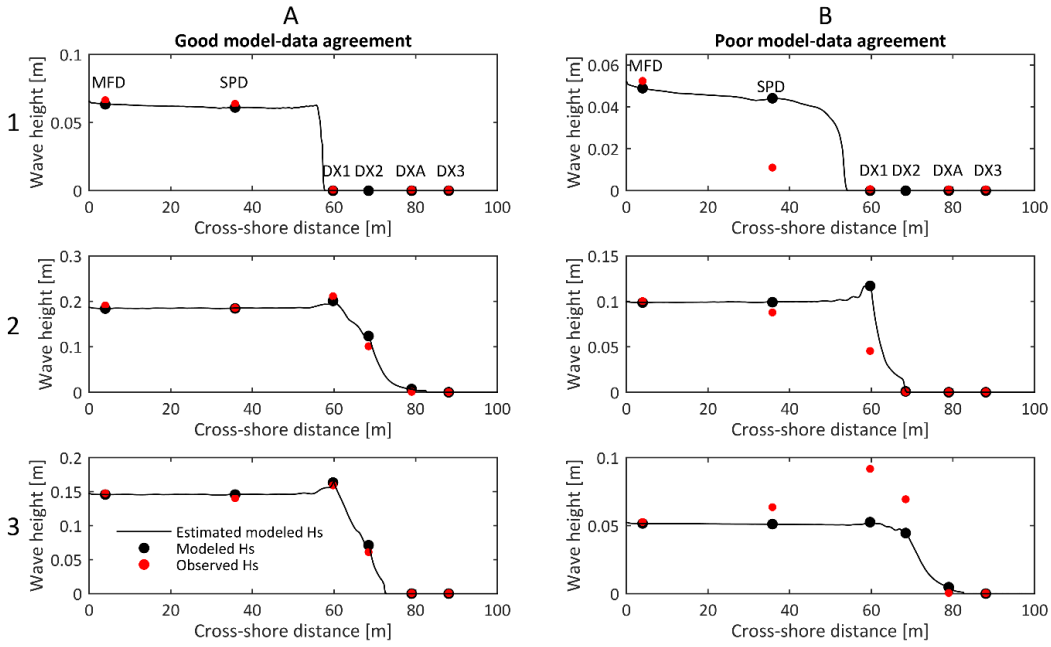

Figure S1.1 In column A, examples of bursts with good model-data agreement, and in column B, examples of bursts with poor model-data agreement. Wave height is on the y axis and cross-shore distance is on the x axis. Red dots show observed wave height, and black dots show modeled wave height, both calculated spectrally from variance density time series at observation points. The black line shows estimated wave height along the whole transect, which is estimated by the variance in water level. In subplot 1B, modeled wave height at station SPD, which is at the edge of the low marsh, is higher than the observed wave height. In subplot 2B, modeled wave height at station DX2, which is at the edge of the first transition zone, is higher than observed wave height. Discrepancies in subplots 1B and 2B could be due to non-shore-normal wave direction in the observations, which the XBeach simulations do not include. In subplot 3B, modeled wave height at stations SPD, DX1, and DX are lower than observed wave heights. This could be due to wind-driven wave growth along the transect, which is reported in Foster-Martinez et al. (2018) and which the XBeach simulations do not include.

Table S1-1 Summary of scatter index scores for modeled versus observed wave heights with different model settings. Scores are shown at each observation point for the calibration and validation time periods in the two columns on the left. Model settings are shown in the top row and include: Manning friction coefficient (varied from 0.016 to 0.020, per the range of values recommended in Chow 1959); maximum wave steepness before breaking (varied from 0.3 to 0.8, per the range of values recommended in the XBeach user manual); Cd values for the four vegetation zones (varied from mean values - 1 standard deviation to mean values + 1 standard deviation, or [0, 0.11, 0.31, 0.4] to [0.75, 0.77, 0.81, 1.46] from low marsh to high marsh); and bathymetry, including a 5 m LEAN corrected DEM which was developed to account for the height of vegetation above bed level (K. Buffington and Thorne 2018) but which under-estimates bed level in the marsh, a 2 m DEM (Danielson et al. 2016) which is the highest resolution DEM available and which over-estimates bed level in the marsh, and the 2 m DEM corrected for discrepancies with a linear interpolation. The bottom row, which is bolded, shows the overall skill score, weighted equally across the six observation stations. Skill scores show that model results are relatively insensitive to changes in Manning friction coefficient and maximum wave steepness. Skill scores show that model sensitivity to bathymetry is similar to sensitivity to changes in Cd coefficients of one standard deviation.

Observation station		***Manning friction coefficient***			***Maximum wave steepness before breaking***			***Cd coefficient***			***Bathymetry***		
		Low	*Mid*	*High*	*Low*	*Mid*	*High*	*Low*	*Mid*	*High*	*Low*	*Mid*	*High*
		0.016	*0.018*	*0.02*	*0.3*	*0.4*	*0.8*	*mean - 1 SD*	*mean*	*mean + 1 SD*	*5 m LEAN corrected DEM*	*2 m DEM corrected with interpolation*	*2 m DEM*
MFD	Calibration	0.03	0.03	0.03	0.03	0.03	0.03	0.03	0.03	0.03	0.03	0.03	0.03
	Validation	0.02	0.02	0.03	0.02	0.02	0.02	0.02	0.02	0.02	0.02	0.02	0.02
SPD	Calibration	0.17	0.17	0.17	0.17	0.17	0.17	0.17	0.17	0.17	0.17	0.17	0.17
	Validation	0.11	0.11	0.11	0.11	0.11	0.11	0.11	0.11	0.11	0.11	0.11	0.11
DX1	Calibration	0.34	0.34	0.34	0.34	0.34	0.34	0.34	0.34	0.33	0.34	0.34	0.3
	Validation	0.3	0.3	0.3	0.3	0.3	0.3	0.31	0.3	0.29	0.3	0.3	0.16
DX2	Calibration												
	Validation	0.26	0.26	0.26	0.26	0.26	0.26	0.6	0.26	0.23	0.25	0.26	0.33
DXA	Calibration	0.39	0.39	0.39	0.39	0.39	0.39	0.83	0.39	0.27	0.57	0.39	0.37
	Validation	0.26	0.25	0.26	0.25	0.25	0.26	0.23	0.25	0.44	0.14	0.25	0.72
DX3	Calibration	0.24	0.24	0.24	0.24	0.24	0.24	0.87	0.24	0.39	0.45	0.24	0.58
	Validation	0.34	0.35	0.34	0.34	0.35	0.35	1.42	0.35	0.34	0.92	0.35	0.61
Total		**0.22**	**0.22**	**0.22**	**0.22**	**0.22**	**0.22**	**0.45**	**0.22**	**0.24**	**0.30**	**0.22**	**0.31**

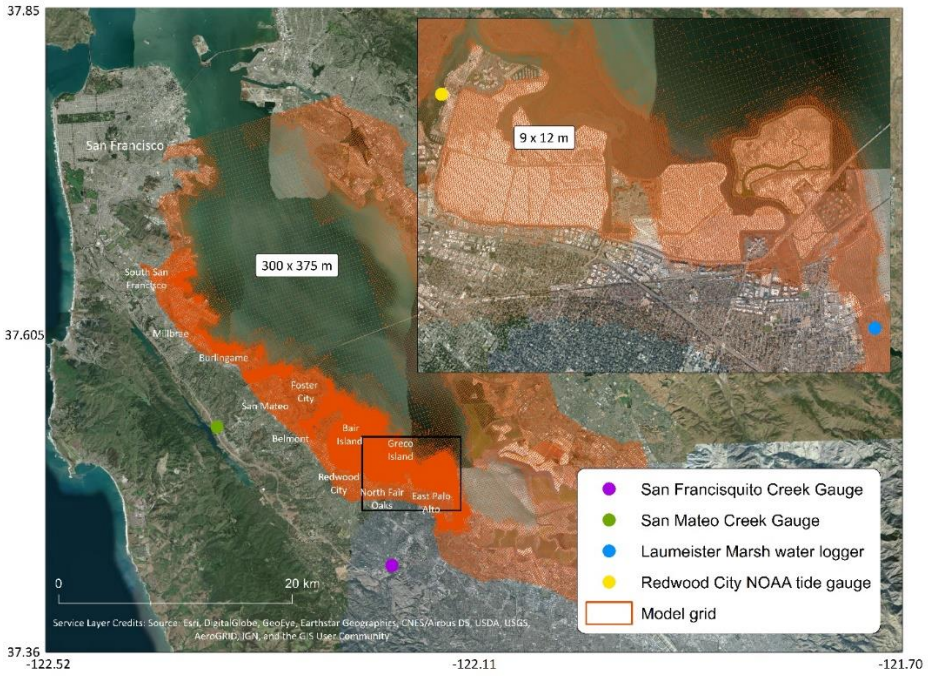

Figure S2.1 Depiction of the model mesh shown in red. The yellow and blue circles show locations of calibration and validation data. The text boxes in the mesh denote the grid resolution of the mesh in its lowest and highest resolution, which are the middle of the bay and in existing and potential San Mateo County marshes, respectively.

Figure S2.2 Observed (red) and modeled (blue) amplitude (cm, row 1) and phase (degrees, row 2) of the top five tidal constituents in the model; vector difference between observed and modeled tidal constituents (cm, row 3).

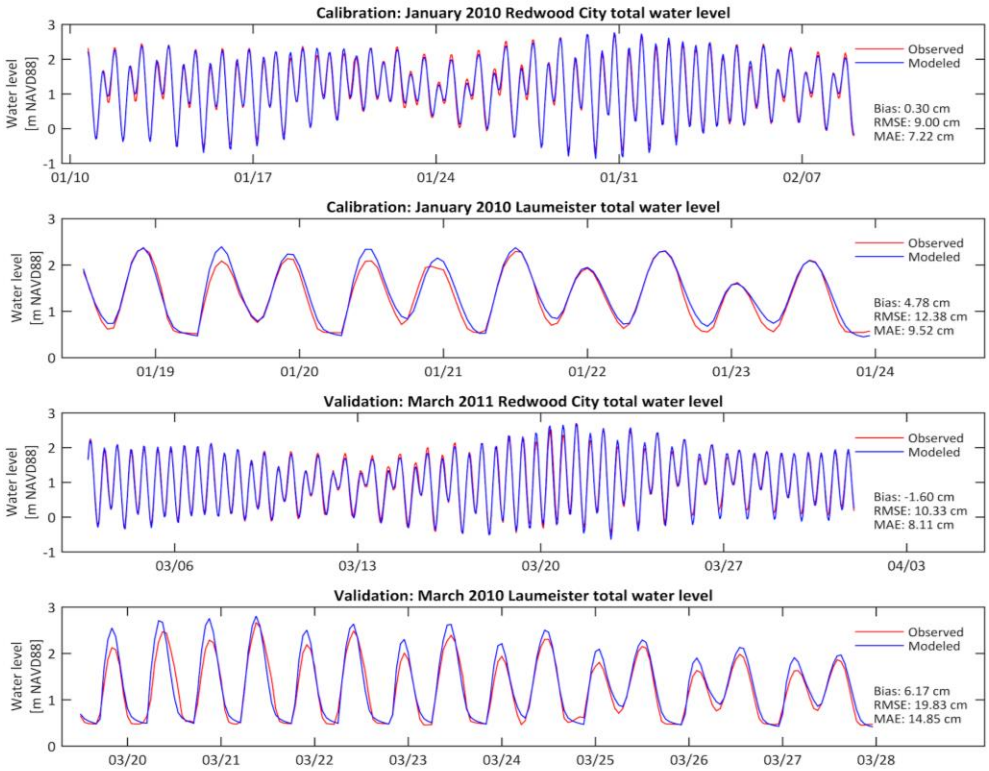

Figure S2.3 Calibration (rows 1 and 2) and validation (rows 3 and 4) time series, comparing model data (blue) and observations (red) at the Redwood City tide gauge (rows 1 and 3) and at a water logger deployed in Laumeister Marsh (rows 2 and 4). Skill scores include bias, root mean square error (RMSE) and mean absolute error (MAE).

Table S2-1 Results from sensitivity analysis of water levels on bathymetry in Laumeister Marsh. Results show that modeled water levels in the marsh channel are highly dependent on local channel depth and slightly dependent on local marsh platform height. Remote bathymetry has limited impact on model performance. Root mean squared error (RMSE), bias, and mean absolute error (MAE) of water levels were used to evaluate model performance.

Bathymetry		Laumeister water levels			Redwood City water levels		
Channel Depth	Platform Height	RMSE (cm)	Bias (cm)	MAE (cm)	RMSE (cm)	Bias (cm)	MAE (cm)
Deep*	High+	16.63	6.38	13.55	9.24	0.35	7.35
Deep	Mid++	15.65	6.23	12.65	9.24	0.35	7.35
Deep	Low+++	15.16	6.17	12.05	9.23	0.36	7.34
Mid**	High	43.76	20.50	34.82	9.24	0.35	7.35
Mid	Mid	41.87	20.02	33.18	9.24	0.35	7.35
Mid	Low	41.00	19.99	32.19	9.23	0.36	7.34
Shallow***	High	107.03	63.03	91.00	9.42	0.34	7.48
Shallow	Mid	101.79	59.55	85.59	9.42	0.34	7.48
Shallow	Low	n/a	n/a	n/a	n/a	n/a	n/a

* 0.25 m NAVD88; **1 m NAVD88; ***2 m NAVD88; +2.73 m NAVD88; ++2.23 m NAVD88; +++1.73 m NAVD88

Table S2-2 Indicators and rank of social vulnerability as determined by BCDC Adapting to Rising Tides "Vulnerable Communities" (BCDC et al., 2020).

Social Vulnerability Indicators	Social vulnerability rank determination: Number of indicators in a given percentile relative to the 9 county Bay area
Very low income Not a U.S. citizen Without a vehicle People with disability Single parent households Communities of color Limited English proficiency Without a high school degree Young children under 5 Severely housing cost burdened Older adults Renters	**Highest social vulnerability:** 8 or more indicators in the 70th percentile OR 6 or more indicators in the 90th percentile **High social vulnerability:** 6-7 indicators in the 70th percentile OR 4-5 indicators in the 90th percentile **Moderate social vulnerability:** 4-5 indicators in the 70th percentile OR 3 indicators in the 90th percentile

Table S2-3 On top, annual expected damages (property loss and people flooded) with existing and restored habitat under 3 different SLR scenarios. On the bottom, total and percentage of protected people and property with existing and restored habitat under 3 different SLR scenarios.

Annual expected damages

	Existing habitat		Restored habitat	
SLR	Property loss ($ millions)	Population flooded	Property loss ($ millions)	Population flooded
0	366	13588	364.80	13581
0.5	1,020	29576	1,012.22	29350
1.0	5,839	112668	5,802.92	112450

SLR	Total property protected ($ millions)	Total population protected	% Property protected	% Population protected
0	1.55	7	0.4	0.1
0.5	7.68	226	0.8	0.8
1.0	36.24	218	0.6	0.2

Table S2-4 Uncertainty ranges for risk with and without marsh restoration, assuming total vertical uncertainty of 25 cm.

Base case damage

SLR	Storm	Existing	Restored	Difference
0	1	$ 354,798,560.00	$ 353,573,250.00	$ 1,225,310.00
0	20	$ 378,091,940.00	$ 376,647,300.00	$ 1,444,640.00
0	100	$ 533,088,700.00	$ 520,691,170.00	$ 12,397,530.00
0.5	1	$ 984,671,500.00	$ 972,521,400.00	$ 12,150,100.00
0.5	20	$ 1,038,250,050.00	$ 1,029,675,000.00	$ 8,575,050.00
0.5	100	$ 1,912,055,300.00	$ 2,028,920,600.00	$ (116,865,300.00)
1	1	$ 5,513,224,700.00	$ 5,475,691,500.00	$ 37,533,200.00
1	20	$ 6,060,539,000.00	$ 6,024,786,000.00	$ 35,753,000.00
1	100	$ 11,020,855,000.00	$ 10,985,019,000.00	$ 35,836,000.00
				AEB
0				*$ 1,545,069.65*
0.5				*$ 7,678,641.25*
1				*$ 36,242,725.00*

Maximum damage (+25 cm)

SLR	Storm	Existing	Restored	Difference
0	1	$453,108,001.32	$432,243,541.52	$ 20,864,459.80
0	20	$483,406,720.98	$461,873,759.39	$ 21,532,961.59
0	100	$700,828,434.49	$649,782,201.80	$ 51,046,232.69
5	1	$1,270,378,392.96	$1,232,305,399.73	$ 38,072,993.23
5	20	$1,354,566,448.41	$1,319,451,763.10	$ 35,114,685.31
5	100	$2,496,076,956.32	$2,631,226,753.15	$ (135,149,796.83)
1	1	$6,939,577,266.06	$6,870,943,917.24	$ 68,633,348.82
1	20	$7,529,324,520.43	$7,466,996,300.30	$ 62,328,220.13
1	100	$12,558,269,457.50	$12,506,557,525.48	$ 51,711,932.02
				AEB
0				*$ 21,590,359.05*
0.5				*$ 32,763,445.08*
1				*$ 64,487,548.29*

Minimum damage (- 25 cm)

SLR	Storm	Existing	Restored	Difference
0	1	$291,688,398.61	$281,216,710.94	$ 10,471,687.67
0	20	$315,485,691.24	$303,653,983.37	$ 11,831,707.87
0	100	$443,655,745.94	$420,955,719.39	$ 22,700,026.55
5	1	$803,219,149.32	$773,284,912.53	$ 29,934,236.79
5	20	$848,240,550.64	$818,697,656.33	$ 29,542,894.31
5	100	$1,546,437,646.25	$1,588,834,372.68	$ (42,396,726.43)
1	1	$4,364,167,225.56	$4,301,308,169.35	$ 62,859,056.21
1	20	$4,842,956,016.69	$4,779,227,027.20	$ 63,728,989.49
1	100	$9,614,711,708.93	$9,544,919,742.15	$ 69,791,966.78
				AEB
0				*$ 11,284,747.57*
0.5				*$ 27,994,560.63*
1				*$ 62,799,740.83*

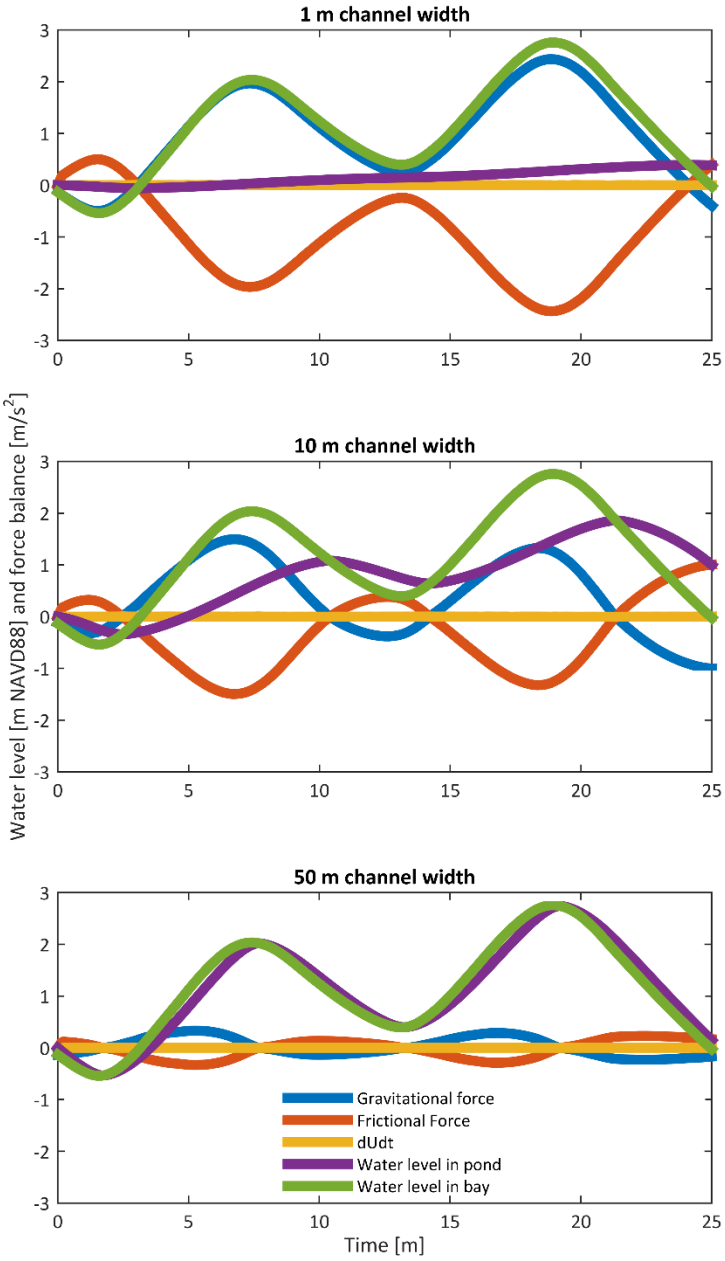

Figure S3.1 A time series of the balance between the gravitational force and frictional force in the bay-pond system, and the resulting water level time series. The three panels show, from top to bottom, the forces and water levels in a system with a 1 m, 10 m, and 50 m channel width.

Table S4-1 Ranking of the top 5 copula for each transect from the joint probability analysis.

	Top 5 Copula Ranking				
Transect	**1**	**2**	**3**	**4**	**5**
1	AMH	t	Gaussian	FGM	Fischer-Kock
2	AMH	t	Gaussian	FGM	Fischer-Kock
3	AMH	t	Gaussian	FGM	Fischer-Kock
4	AMH	FGM	Fischer-Kock	Nelsen	Frank
5	AMH	FGM	Fischer-Kock	t	Gaussian
6	AMH	Shih-Louis	t	Gaussian	FGM
7	AMH	t	Gaussian	FGM	Fischer-Kock
8	AMH	t	Gaussian	FGM	Fischer-Kock
9	AMH	t	Gaussian	FGM	Fischer-Kock
10	AMH	t	Gaussian	FGM	Fischer-Kock
11	AMH	t	Gaussian	FGM	Fischer-Kock
12	AMH	t	Gaussian	FGM	Fischer-Kock
13	AMH	t	Gaussian	FGM	Fischer-Kock
14	AMH	t	Gaussian	FGM	Fischer-Kock
15	AMH	t	Gaussian	FGM	Fischer-Kock
16	AMG	t	Gaussian	FGM	Fischer-Kock
17	Shih-Louis	AMH	FGM	Fischer-Kock	Nelsen
18	Shih-Louis	AMH	FGM	Fischer-Kock	Nelsen
19	Shih-Louis	AMH	FGM	Fischer-Kock	Nelsen
20	Shih-Louis	AMH	FGM	Fischer-Kock	Nelsen
21	Shih-Louis	AMH	FGM	Nelsen	Plackett
22	Shih-Louis	AMH	FGM	Fischer-Kock	Nelsen
23	Shih-Louis	AMH	FGM	Fischer-Kock	Nelsen
24	Shih-Louis	AMH	FGM	Fischer-Kock	Nelsen
25	Shih-Louis	AMH	FGM	Fischer-Kock	Nelsen
26	Shih-Louis	AMH	FGM	Fischer-Kock	Nelsen
27	Shih-Louis	AMH	FGM	Fischer-Kock	Nelsen
28	Shih-Louis	AMH	FGM	Fischer-Kock	Gaussian
29	Shih-Louis	AMH	Gaussian	t	FGM
30	Shih-Louis	AMH	FGM	Fischer-Kock	Nelsen
31	Shih-Louis	AMH	FGM	Fischer-Kock	Nelsen
32	Shih-Louis	AMH	FGM	Fischer-Kock	Nelsen
33	Shih-Louis	AMH	FGM	Fischer-Kock	Nelsen
34	Shih-Louis	AMH	FGM	Fischer-Kock	Nelsen
35	Shih-Louis	AMH	FGM	Fischer-Kock	Nelsen
36	Shih-Louis	AMH	FGM	Fischer-Kock	Nelsen
37	Shih-Louis	AMH	FGM	Fischer-Kock	Nelsen
38	Shih-Louis	AMH	FGM	Fischer-Kock	Nelsen
39	Shih-Louis	AMH	FGM	Nelsen	Plackett
40	Shih-Louis	AMH	FGM	Nelsen	Plackett
41	Shih-Louis	Raftery	AMH	FGM	Nelsen
42	Shih-Louis	AMH	FGM	Nelsen	Plackett
43	Shih-Louis	AMH	FGM	Fischer-Kock	Nelsen
44	Shih-Louis	AMH	FGM	Fischer-Kock	Nelsen
45	Shih-Louis	AMH	FGM	Fischer-Kock	Nelsen
46	Shih-Louis	AMH	FGM	Fischer-Kock	Nelsen
47	Shih-Louis	AMH	Gaussian	t	FGM
48	Shih-Louis	AMH	Gaussian	FGM	Fischer-Kock

Figure S4.1 A plot of the Pinsky (2013) equation relating vegetation drag coefficient (Cd) and Reynolds number (Re) in marshes. The equation is shown on the black line, with one and two standard deviations shown in dark and light pink, respectively. The black dots represent conditions in our experimental runs.

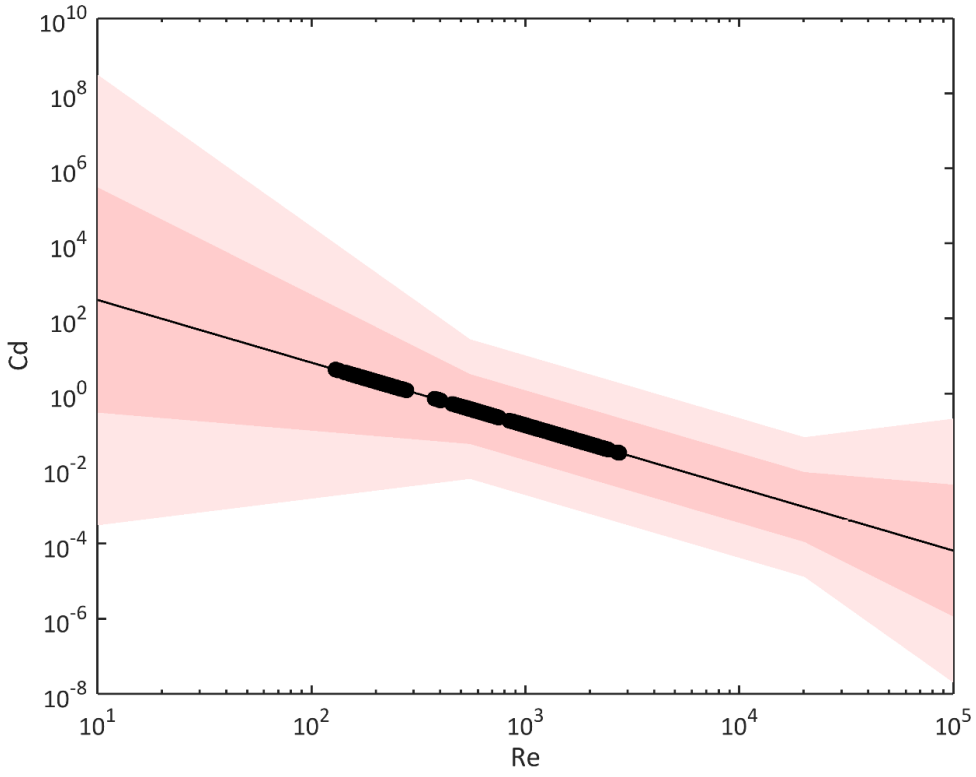

Appendix

XBeach Non-hydrostatic

XBeach was originally developed as a phase-averaged wave model that resolves amplitude variation on the wave group scale but does not resolve individual waves as in a Boussinesq model. Recently, a non-hydrostatic mode (XB-NH) was developed for XBeach which is able to fully resolve incident-band (short period) waves. XBeach simulates nearshore processes including wave transformation, wave-induced setup, over-wash, and inundation. In addition to information on water levels and wave heights, model outputs can include parameters such as flow and orbital velocity, bed shear stress, and Stokes drift. The non-hydrostatic mode is able to fully resolve incident-band waves. Resolution of incident-band waves, though computationally costly, is necessary to determine swash on relatively steep slopes and is thus necessary to investigate runup and potential overtopping.

Non-hydrostatic XBeach calculations are based on the non-linear shallow water equations, including a non-hydrostatic pressure term. The depth averaged dynamic pressure is computed from the mean of the dynamic pressure at the surface and at the bed by assuming the dynamic pressure at the surface to be zero and a linear change over depth, where w is the vertical velocity and z is the vertical coordinate:

$$\frac{\delta w}{\delta t} + \frac{\delta q}{\delta z} = 0$$

The vertical velocity at the bed is set by the kinematic boundary condition:

$$w_b = u \frac{\delta(\eta - h)}{\delta x}$$

Combining the Keller-box method for the description of the pressure gradient in the vertical, and with substitution, the dynamic pressure at the bed can be described by:

$$\frac{\delta w_s}{\delta t} = 2\frac{q_b}{h} - \frac{\delta w_b}{\delta t}$$

The dynamic pressure at the bed is subsequently solved by solving the continuity equation:

$$\frac{\delta u}{\delta x} + \frac{w_s - w_b}{h} = 0$$

This method simplifies the hydrodynamics of plunging waves. For example, it does not include highly resolved vertical discretization and it does not simulate the overturning of waves. However, it has been shown to provide sufficient skill to describe dominant characteristics of the flow.

XB-NH allows for the inclusion of the effect of vegetation within the model via vegetation parameters including stem density, frictional drag coefficient, stem height, and stem diameter (van Rooijen et al. 2015; 2016). Wave-vegetation interactions are included in the model following the approach of Mendez and Losada (2004). It is possible to include multiple heterogenous vegetation layers, but in this dissertation only one layer was used. Dissipation by vegetation is described by:

$$D = A_v \times \frac{\rho C_D b N}{2\sqrt{\pi}} (\frac{kg}{2\sigma})^3 H^3$$

$$A_v = \frac{(sinh^3 k\alpha h) + 3(sinhk\alpha h)}{3kcosh^3 kh}$$

$C_D$is the bulk drag coefficient, b is the vegetation stem diameter, N is the stem density, and α is the relative vegetation height.

XBeach non-hydrostatic is computationally costly, particularly in short wave environments. A minimum of 30 grid cells per wavelength are recommended to capture wave transformation

across the grid, and thus short wave environments result in small grid cells and small time steps, quickly increasing the run time of a simulation. Additionally, simulations with too many grid cells will fail, which makes regional 2D models challenging to create in short wave environments.

XBeach has been extensively tested and validated in sandy beach environments. The vegetation module within XBeach was developed more recently and while wave transformation and setup have been tested and validated, observations of runup and overtopping through vegetation have not yet been collected.

Delft 3D Flexible Mesh

Delft3D Flexible Mesh solves the shallow water equations with a finite volume method on staggered unstructured grids in 1D and 2D horizontal (2DH) schematizations. In this dissertation, only the 2DH application was used. The shallow-water equations express conservation of mass and momentum:

$$\frac{\partial h}{\partial t} + \nabla \cdot (hu) = 0$$

and

$$\frac{\partial u}{\partial t} + \frac{1}{h}(\nabla \cdot (huu) - u\nabla \cdot (hu)) = -g\nabla\zeta + \frac{1}{h}\nabla \cdot (vh(\nabla u + \nabla u^T)) + \frac{1}{h}\frac{\tau_b + \tau_w}{\rho}$$

where

$$\nabla = (\frac{\partial}{\partial x}, \frac{\partial}{\partial y})^T$$

ζ is the water level, h is the water depth, u is the velocity vector, g is gravitational acceleration, v is the viscosity of water, ρ is the density of water. τ_b represents the bottom friction and is represented by $\tau_b = \frac{\rho g}{C^2}||u||u$. τ_w represents the wind friction acting on the free surface, $\tau_w = C_d\rho_a||\tilde{u}_{10}||\tilde{u}_{10}$. $\tilde{u}_{10}$ represents the absolute wind velocity.

The two-dimensional shallow water equations are solved in a staggered scheme, meaning that velocity is solved at the edges or faces of the grid cells while water levels are solved at cell centers. This arrangement is called an Arakawa C-grid and the approach requires that the grid is orthogonal. The model can also be used on an unstructured grid, meaning that grid cells can have any number of faces. However, in this application, Delft3D Flexible Mesh was

coupled to SWAN, which requires that grid cells have no more than 4 nodes (i.e. are rectangular or triangular).

The model can include such processes as tide and wind driven flows (such as storm surges), stratified and density driven flows, river flows, channel flows, rainfall runoff, salt intrusion, and transportation of material and pollutants.

It is assumed that depth is much smaller than the length scale, allowing the vertical momentum to be reduced to the hydrostatic pressure relation and neglecting vertical accellerations. The Boussinesq approximation is also made in the model, which means fluid density differences are neglected except when they are multiplied by gravitational acceleration.

SWAN

SWAN (Simulating Waves Nearshore) is a third-generation numerical wave model. SWAN computes random waves and currents in coastal areas with shallow water. The model is based on Eulerian formulation of discrete spectral balance of action energy, and solves the spectral action balance equation:

$$\frac{\partial}{\partial t}N + \frac{\partial}{\partial x}c_x N + \frac{\partial}{\partial y}c_y N + \frac{\partial}{\partial \sigma}c_\sigma N + \frac{\partial}{\partial \theta}c_\theta N = \frac{S}{\sigma}$$

The first term on the left side of the equals sign represents the temporal rate of change of action density, N. The second and third terms represent the propagation of action in the x and y directions, with velocities c_x and c_y, respectively. The fourth term represents shifting in relative frequency due to changes in depths and currents, with velocity c_σ in σ space. The fifth term represents refraction due to changes in depths and currents with velocity c_θ in θ space. S represents the source term in terms of energy density, and represents the effects of wave generation and dissipation, and wave-wave interactions, depending on wave frequency and direction.

Transfer of wind energy into waves is described in SWAN with the following formula, where A and B depend on wave frequency and direction and wind speed and direction:

$$S_{in}(\sigma, \theta) = A + BE(\sigma, \theta)$$

Dissipation of wave energy is described in SWAN as the sum of contributions from whitecapping, bottom friction, and depth induced breaking. Dissipation due to whitecapping is described by:

$$S_{ds,w}(\sigma,\theta) = \Gamma\tilde{\sigma}\frac{k}{\tilde{k}}E(\sigma,\theta)$$

Γ is a steepness dependent coefficient. k is a wave number. $\tilde{\sigma}$ and $\tilde{k}$ denote a mean frequency and a mean wave number, respectively.

Bottom-induced dissipation is described by:

$$S_{ds,b}(\sigma,\theta) = -C_{bottom}\frac{\sigma^2}{g^2 sinh^2(kd)}E(\sigma,\theta)$$

Where C_{bottom} is a friction coefficient. Dissipation due to depth-induced wave breaking is described by:

$$S_{ds,br}(\sigma,\theta) = \frac{S_{ds,br,tot}}{E_{tot}}E(\sigma,\theta)$$

where E_{tot} is the total wave energy and $S_{ds,br,tot}$ is the rate of dissipation of total energy. This rate depends on a breaking parameter $\frac{H_{max}}{depth}$. In SWAN, this value is set to a constant of 0.73.

SWAN can simulate wind-driven wave generation, white-capping, bottom dissipation, and depth-induced wave breaking following the above equations. Quadruplet wave-wave interactions and triad wave-wave interactions are also included in SWAN. These interactions are included implicitly rather than explicitly, meaning that the model is not subject to the Courant criterion and thus can utilize larger time steps, increasing computational efficiency by two orders of magnitude.

Quadruplet wave-wave interactions and triad wave-wave interactions are included in SWAN, through a discrete interaction approximation (DIA) and a lumped triad approximation (LTA), respectively. The DIA approximation for quadruplet wave-wave interactions has been found to work fairly well in many cases but has been found to be less satisfactory for long-crested waves with a narrow directional distribution and for waves with frequency resolutions with ratios very different from 10%. The LTA approximation for triad wave-wave interactions has been found to perform reasonably well but it was developed from observations in a flume rather than the field. SWAN computes wave-induced setup, and in 2D this computation is done on approximations which do not apply in lakes.